COMPUTATIONAL STUDY OF LAMINAR FLOW IN MICROCHANNELS WITH ABRUPT EXPANSION OR CONTRACTION AT A 90° MITER BEND

by

Sadhashiva R. Chilukoori

A thesis submitted to the faculty of
The University of Utah
in partial fulfillment of the requirements for the degree of

Master of Science

Department of Mechanical Engineering

The University of Utah

May 2013

THE UNIVERSITY OF UTAH GRADUATE SCHOOL

STATEMENT OF THESIS APPROVAL

The thesis of Sadhashiva R. Chilukoori has been approved by the following supervisory committee members:

Timothy A. Ameel, Chair, 11/26/2012
Date Approved

James R. Stoll, Member, 11/26/2012
Date Approved

Kuan Chen, Member, 11/26/2012
Date Approved

and by Timothy A. Ameel, Chair of the Department of Mechanical Engineering and by Donna M. White, Interim Dean of The Graduate School.

ABSTRACT

Rapid prototyping technologies have radically reduced the time required for the development and field disposal of microfluidic devices. Xurography is one such technology, in which the microstructures are fabricated in double-sided adhesive tape using a cutting process. This cutting process is highly imprecise, particularly when cutting features such as bends and junctions where the blade is required to change cutting direction. As a result of this imprecision, expanding or contracting microchannels can be produced while fabricating serpentine microchannels. In order to efficiently use xurography to fabricate microfluidic systems for applications such as heat exchangers, it is necessary to characterize the effects of these abrupt expansions and contractions at 90° miter bends.

A steady state incompressible flow simulation of water in microchannels containing a 90° miter bend is conducted. Microchannels with miter bends, including abrupt expansions and contractions after the miter bend in some cases, are used in these simulations. The aspect ratio of these channels ranges from 0.2 to 1.0 and the area ratio of contraction and expansion ranges from 0.33 to 0.91 and 1.1 to 3, respectively. Commercially available software packages, Fluent and Gambit, are used for this purpose. A pressure-based solver using a fully-coupled implicit algorithm with algebraic multigrid method is used for the simulation. Third-order MUSCL scheme is used for the momentum discretization and the PRESTO scheme for the pressure.

Excess loss coefficients, flow development lengths downstream of the miter bend, and the length and width of the recirculation zones, both upstream and downstream of the miter bend, are evaluated for the microchannels with different aspect ratios and area ratios for Reynolds numbers ranging from 5 to 600. It is observed that the critical Reynolds number Re_{cr} of the microchannel is a function of the aspect ratio. An axial flow vortex that develops in the outlet channel results in the independence of the primary recirculation zone on Reynolds number and decreasing secondary recirculation

zone's penetration into the outlet with Reynolds number. The development length downstream of the miter bend is better predicted by the conventional model than the more advanced models based on aspect ratio. Bend excess loss coefficients K_b are in reasonable agreement with the microscale experimental loss coefficients reported in the literature. The bend excess loss coefficients decrease with increasing area ratio A_r in both the expansion and contraction channels, when the losses are normalized with the inlet kinetic head. Bend excess loss coefficient K_{be} for the expansion channel remains nearly constant for high expansion ratios. Bend excess loss coefficients for expansions and contractions in the 90° miter bend microchannels are far less than the similar experimental data reported in the literature, due to the surface roughness, inconsistent channel dimensions, and the damage to the channel walls caused by the cutting process.

To my parents

Vijaya Laxmi and Bal Reddy Chilukoori

CONTENTS

LIST OF FIGURES

LIST OF TABLES

ACKNOWLEDGEMENTS

I take this opportunity to thank Dr. Timothy Ameel for his invaluable advice and guidance, which was pivotal in the success of this work. I also thank Dr. James Stoll and Dr. Kuan Chen for being a part of my thesis committee.

I must acknowledge the work conducted by Rahul Kolekar, Dan Torgerson, and Lam Nguyen on the flows in xurographic microchannels; it is the results of their experiments that laid the foundation to this work. I am grateful to Bhagirath Addepalli and Manjunath Basavarajappa for their creative ideas, which are an integral part of this work.

I am thankful to the CADE lab at the University of Utah for providing me with the computational resources and the simulation packages. A special thanks is reserved to the CADE lab operators for their help in resolving the technical issues of parallel simulations, especially Mr. Mark Ogden.

I am grateful to my friends and family for their continuous support and belief in me all through this work.

CHAPTER 1

INTRODUCTION

The roots of microfluidics can be traced back to the microscale gas chromatography and the ink jet printing technologies developed in the 1970s [1], along with the work of Tuckerman and Pease [2] in designing and analyzing a micro heat exchanger for microprocessor cooling. In addition to being highly portable, these technologies have successfully demonstrated the unique advantages that can be realized by working at the microscale, such as:

- a small quantity of sample or reagent is required in bio-analysis applications,
- results are quick and reliable,
- fluid handling is easily controlled, and
- high heat transfer rates are possible.

These advantages have played a key role in the evolution of microfluidics into a highly multidisciplinary research field. Some of the early adopters of microfluidics were from the fields of microelectronics (for ink jet printers [1]), biology, and genomics (as a molecular analysis tool [3]).

Notably, all of these devices were fabricated from silicon wafers using the traditional etching processes employed in the fabrication of microchips. The microstructures fabricated using this process had the highest accuracy, but the process of etching on silicon wafers remains a time-consuming operation requiring skilled labor and specialized clean room facilities. Another disadvantage of microfluidic devices is the significantly high pressure losses involved with the microchannel flows even for low Reynolds numbers (Re). The Reynolds number is defined as

$$Re = \frac{\rho v_{avg} L_{ch}}{\mu}, \tag{1.1}$$

where ρ is the density , μ is the viscosity of the fluid, v_{avg} is the average velocity of the flow, and L_{ch} is the characteristic length of the system. The long development time, high costs involved with the fabrication processes, and the high pressure losses limited most microfluidic devices to academic research and high-end applications. In order to fully utilize the advantages of microfluidics, it was necessary to explore cost-efficient materials and fabrication procedures. These developments have resulted in a new class of microfabrication techniques classified as rapid prototyping techniques. For example, soft lithography uses a cheaper soft polymer called Poly-Dimethylsiloxane (PDMS) [4, 5] as a substrate in which the channel geometries are fabricated.

These new rapid prototyping techniques helped cut the lead time for the design and fabrication of new microdevices from days to a matter of hours. The low material cost and reusability of polymers was an added benefit that paved the way to the development of complex microsystems called "Lab-on-Chip" (LoC) devices, that integrate the capability of sample conditioning, analysis, and results [6–8] into a single microdevice. LoCs form a subset of a larger group of devices called microelectromechanical systems (MEMS) with a wider scope of applications such as micro power plants, microengines, microsensors, etc., (a detailed review of these devices is presented by Hassan [9]). These devices often use features like microchannels, microvalves [10], micropumps [11], micromixers [12] etc., to move around and manipulate the working fluid. The accuracy with which these features are fabricated is an important aspect in characterizing the performance of the microdevice.

Xurography is one such low-cost rapid prototyping technique proposed by Bartholomeusz et al. [13,14] as an alternative method for fabricating microstructures. Xurography is a cutting process in which features such as microchannels, valves, etc., are cut in films of thickness ranging from 25 to 1000µm. These films are later bonded between glass slides to form the microdevices. The cutting process is carried out using a graphic vinyl cutter on a lab desktop or a laser. There is no need for a clean room

to carry out this process; moreover, even complicated geometries such as multilayered devices can be fabricated in a matter of minutes using materials like tape and glass slides that are readily available in any lab.

Xurography is used in applications such as Polymerase Chain Reaction (PCR) by Greer et al. [15], where it has been reported that the results produced by the xurographic devices were comparable to those obtained with a commercial device. The xurographic device used a smaller quantity of sample (10nl, about 1000 times less than the commercial device) and the final cost of fabrication was less than $200. This work clearly demonstrates the massive benefits that can be gained in the form of fabrication time and resources (i.e., materials and facilities needed for the job). The work of Greer et al. [15] also highlights a flaw with microstructures fabricated using xurography, namely, geometrical inaccuracies.

These geometrical inaccuracies creep into the xurographic devices for two reasons. First, to ensure a tight bond between the tape and the glass slab, additional adhesives are used and the entire device is held under pressure, causing the adhesive to expand into the channel system in the form of tiny globules (see Fig. (1.1a), and the subfigures (a), (d), (c), and (e) of Fig. (1.2)). These globules act as flow tripping elements that may cause an early transition into turbulence, significantly increasing the pressure losses. The onset of turbulence due to the presence of the flow tripping elements is reported to occur at a $Re = 1000$, which is much higher than that for the applications considered in this report. Moreover, it will be explained in the following chapters that the turbulence may occur in the microchannels for Reynolds number as low as $Re = 500$ due to the presence of bends in the microchannels.

The second reason, and the focus of this study, is the deformations that result from the maneuvering of the cutting blade (see the subfigures (a) and (f) of Fig. (1.2)). Simply explained, to produce a microstructure in the tape, the blade has to cut along a predefined path. If this path includes elements like a 90° bend (miter bend) or a curve, the blade has to perform a complex set of maneuvers to cut these elements. As a result, the tape is subjected to a significant amount of shearing, often deforming the delicate structure. Even with extreme caution, simple operations such as producing a serpentine channel result in a structure with varying channel width, as reported by

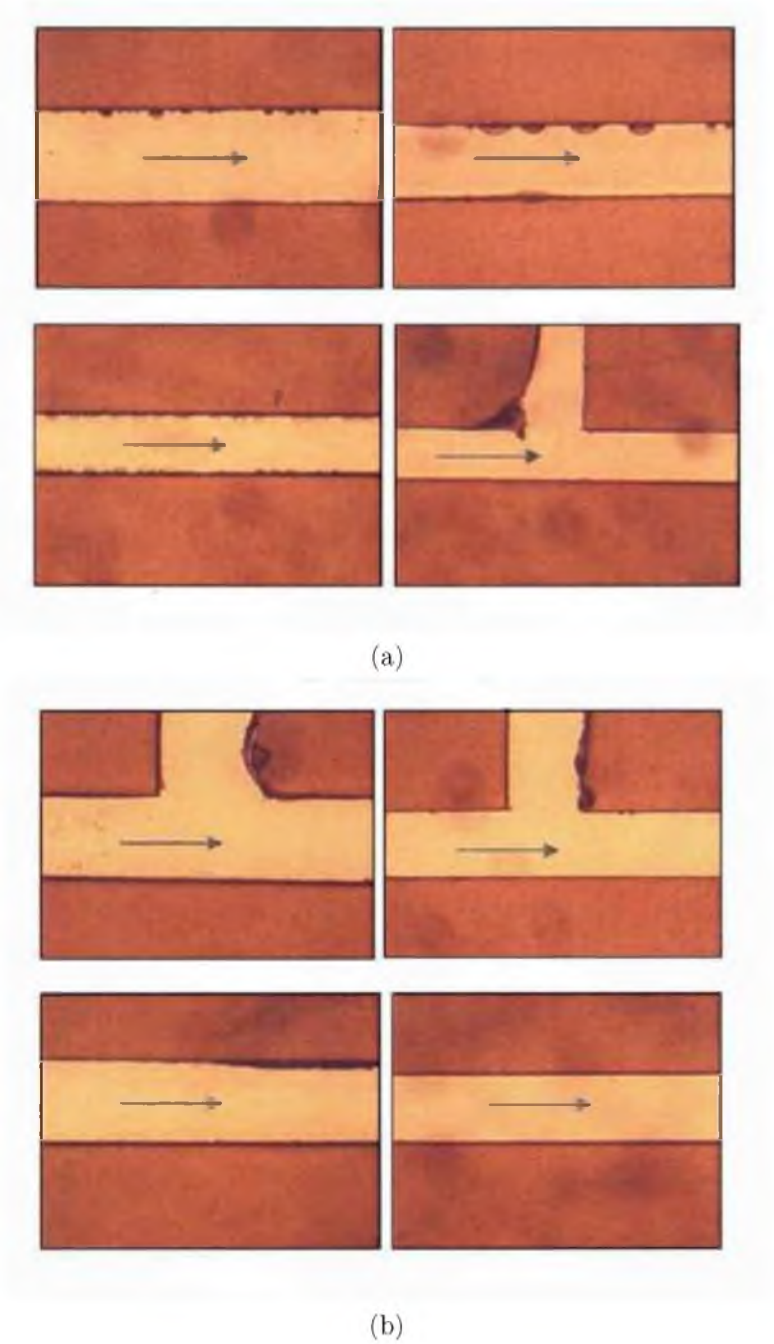

(a)

(b)

Figure 1.1: **Inaccuracies in xurographic microchannels I**: The images show some of the commonly occurring inaccuracies in microchannels fabricated using xurography. (a) Adhesive globules on the channel walls. (b) Improperly cut edges on the bends. **(Reprinted with permission from ref. [16])**

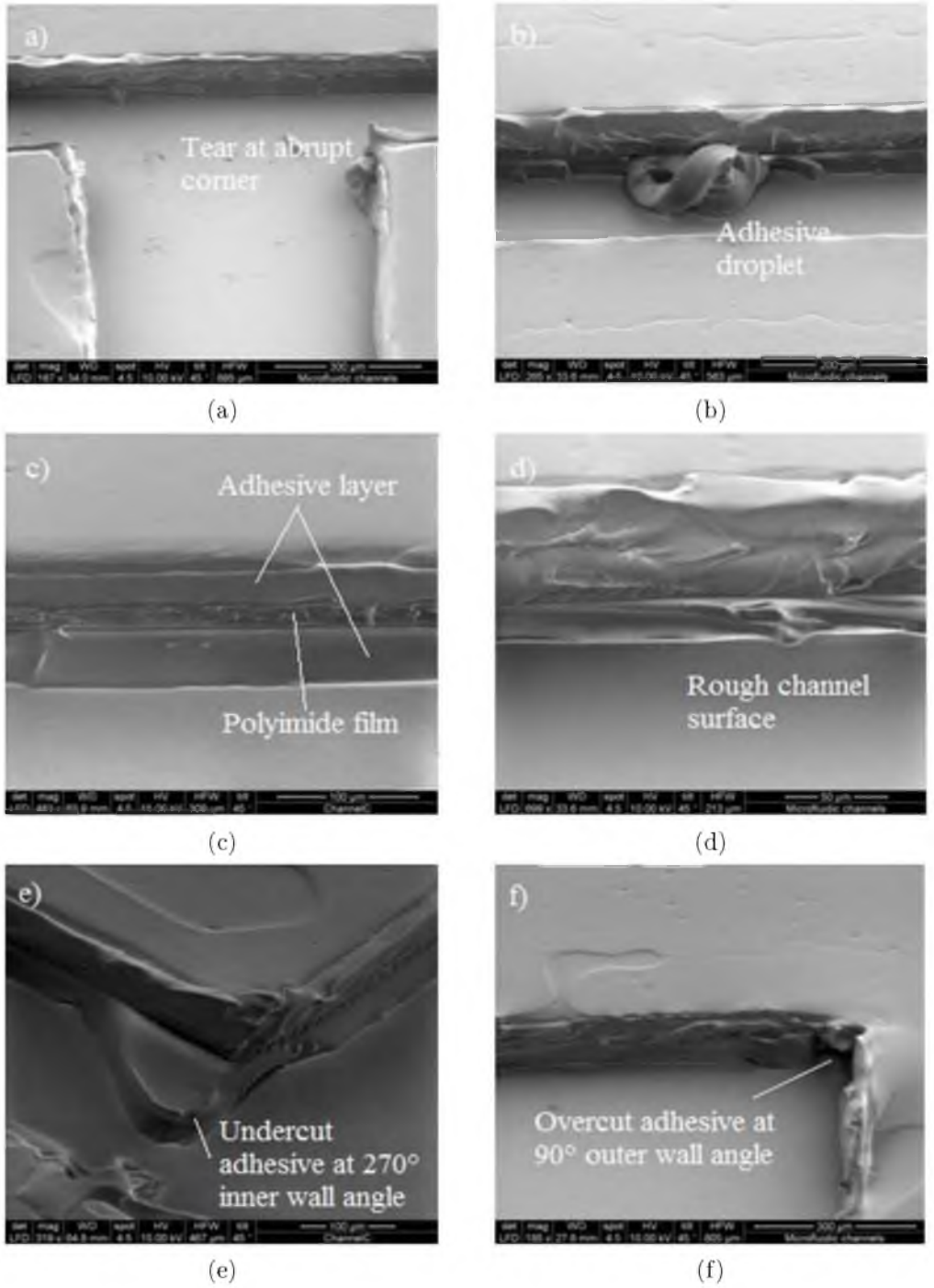

Figure 1.2: **Inaccuracies in xurographic microchannels II**: Images of inaccuracies in xurographic microchannels as seen under a Scanning Electron Microscope (SEM). (a) Tearing of tape at abrupt corners. (b) Adhesive globule in the channel. (c) Cross-section showing layers of film and adhesive. (d) Roughness of channel walls. (e). Adhesive globule at the corner. (f) Overcut tape in the corner.**(Reprinted with permission from ref. [17])**

Kolekar [16], when the blade changes cutting direction at the bend (see Fig. (1.1b)). This brings us to an interesting aspect of microchannel flow: *the effects of abrupt expansion or contraction of a microchannel at a miter bend on the flow field.* At this juncture, one may be skeptical about the need to characterize these effects, as most of the applications discussed to this point operate in a *creeping flow* regime, where the losses due to inaccuracies are insignificant. This is true, but the xurographic devices are not limited to the molecular analysis in a creeping flow regime. It has been experimentally demonstrated by Kolekar [16] that with a suitable clamping system, a xurographic microdevice can sustain the pressure of flows up to an $Re = 3000$ without any leakage from the adhesive tape.

This capability of xurographic microchannels to sustain high pressures was well utilized by Alshareef [18], in designing and successfully testing a microscale heat exchanger (see Fig. (1.3a)). It is reported that the efficiency of this heat exchanger was maximum, with minimum pressure losses when it was operated in the Reynolds number range of $500 \leq Re \leq 800$. Furthermore, as a means to enhance the heat transfer rate between the fluids, thereby increasing the efficiency of the device itself, serpentine channels with miter bends were used in the heat exchanger (see Fig. (1.3b)). A serpentine channel design helps to keep the device compact and portable by fully utilizing the available surface area on the device. Using xurography to fabricate these channels reduces the time and cost of fabrication. However, as explained earlier, the resulting channels may have a set of abruptly expanding or contracting bends. In order to completely characterize the performance of the micro heat exchanger, it is essential to understand the effect of abrupt expansions and contractions on fluid flow in miter bend microchannels. This characterization will ultimately assist in the design of efficient microfluidic systems by the selection of an appropriate driving force for the flow.

1.1 Simulation of microflows

The average computing power of a modern day PC has increased by ten orders of magnitude in the last decade. The introduction of new features like multicore processors has made it possible to run complex mathematical simulations on a per-

(a)

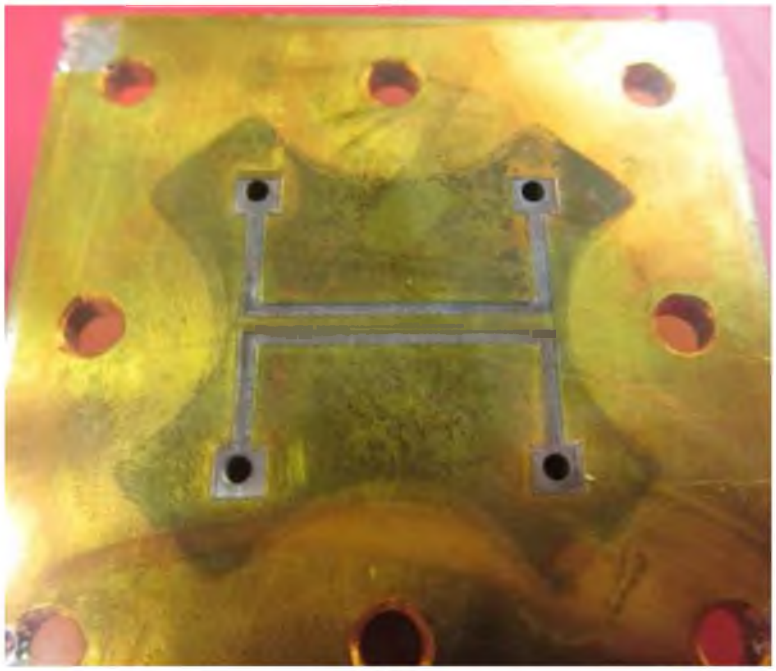

(b)

Figure 1.3: **Microscale heat exchanger**: A single-pass, single-phase, counterflow heat exchanger fabricated using xurographic microchannels sandwiched between copper plates. (a) An assembled view of heat exchanger. (b) A view of the microchannels in the tape. **(Reprinted with permission from ref. [18])**

sonal computer, in turn bringing down the costs of workstations [19]. As a result, Computational Fluid Dynamics (CFD) has evolved into an indispensable tool in the prefabrication development and analysis of a flow system. CFD provides a flexible means to analyze new designs by simply modifying the solid model accordingly. A CFD model also helps validate the experimental results and estimate the extent of error due to fabrication defects, measurement inaccuracies, etc., in the final device. In the case of microfluidics, although the cost and time of fabrication is low (with rapid prototyping), the cost of performing experiments is still high as the experiments need high-end equipment like a scanning electron microscope (for accurately measuring the channel dimensions) to accurately characterize the results. Therefore, CFD is useful in studying the preliminary design of a microfluidic device as a means to test performance relative to the requirements of the application, as well as to make suitable adjustments in the design to accommodate manufacturing defects.

Today, a plethora of numerical models are available, both as open source and commercial packages, that can simulate a wide variety of flow scenarios, ranging from a simple steady-state single-phase flow to a complex flow in a porous medium. OpenFOAM, ANSYS FLUENT, FLOW-3D, CFD-ACE+, and CFX are some of the popularly used commercial CFD packages. These packages use the Finite Volume Method (FVM) to solve the Navier-Stokes equations in general.

The present study uses Fluent (v6.3.26) to perform the flow simulations and Gambit (v2.4.6) to mesh the flow domain. In these simulations, the steady state and incompressible Navier-Stokes equations are solved for Reynolds numbers in the range of $5 \leq Re \leq 600$. Microchannels, with rectangular cross-sections, whose hydraulic diameters are in the range of $100\,\mu\text{m} \leq D_h \leq 188\,\mu\text{m}$, are used in the simulations. The hydraulic diameter (D_h) for a rectangular channels is defined as

$$D_h = \frac{2wh}{(w+h)}, \tag{1.2}$$

where h is the height and w is the width of the channel, respectively. The height of these microchannels (see Fig. (1.4))is kept constant (at $h = 100\,\mu\text{m}$), the approximate thickness of the double-sided adhesive tape. By varying the width of the microchan-

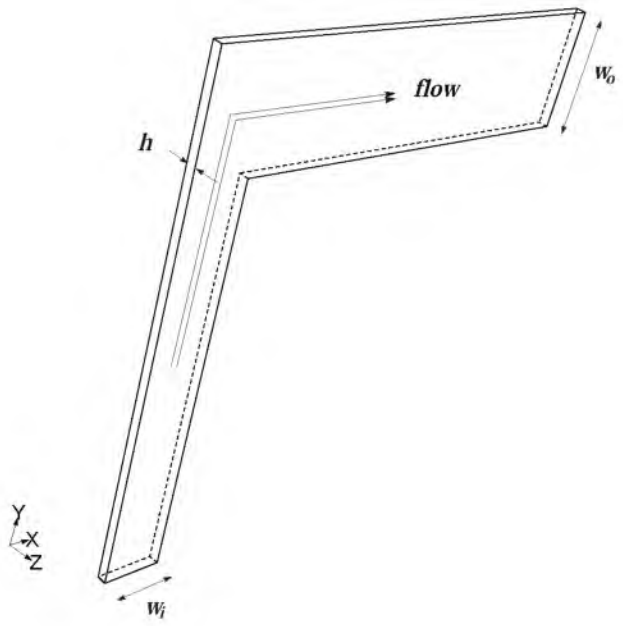

Figure 1.4: **A Sample microchannel with an expanding miter bend**: Image shows the flow direction and the generic dimensions of the domain used for the flow simulations. Here, w_i and w_o are the channel widths at the inlet and outlet, respectively.

nel, a set of nine channels whose *aspect ratio* (α), defined as

$$\alpha = \frac{h}{w} \quad (\leq 1), \tag{1.3}$$

falls in the range of $0.2 \leq \alpha \leq 1.0$. Data for the bend minor loss coefficients, flow development length after the miter bend, the flow separation Reynolds number, and the size of recirculation zones as a function of the Reynolds number are collected from these simulations. Using the channel with nominal aspect ratio $\alpha = 0.33$, a set of microchannels with abrupt contractions or expansions at 90° miter bends are examined. Area ratios (A_r) at a miter bend, defined as

$$A_r = \frac{\text{cross-section area of outlet}}{\text{cross-section area of inlet}}, \tag{1.4}$$

are in the range of $0.33 \leq A_r \leq 0.91$ and $1.1 \leq A_r \leq 3$, respectively. These channel designs are accomplished by keeping the width (w_i) of the inlet and the height of the

channel constant (at $h = 100\,\mu m$) and decreasing or increasing the width (w_o) of the outlet channel accordingly (see Fig. (1.4)). The data from these channels are used to study the effects of abrupt expansions and contractions on above-mentioned factors for liquid (water) flows in microchannels containing a 90° miter bend. The data also serve the purpose of numerically validating the experimental results obtained by Kolekar [16] and Nguyen [17].

1.2 Summary

Microfluidics is a rapidly growing field with a diversified area of applications. Advances in manufacturing technologies have opened the possibilities of fabricating complex LoCs in a time frame of hours. Further, these procedures are much more inexpensive than traditional procedures. On the downside, the microfeatures fabricated using these techniques are often geometrically inaccurate.

Xurography is one such rapid prototyping technology known to produce variations in the channel widths whenever there is a change in the cutting direction. This results in the formation of abrupt expansions and contractions when fabricating miter bends in the microchannels. To completely characterize the performance of xurographic microfluidic devices, it is of utmost importance to study the effects of abrupt expansions and contractions at miter bends in microchannel flows.

The present work investigates these effects for liquid flows in microchannels containing a 90° miter bend using computational fluid dynamics. The report presents the data on bend minor loss coefficients, flow development length after the miter bend, flow separation and the size of the recirculation zones with the Reynolds number, and the effect of the abrupt expansion and contraction on these parameters for water in the Reynolds number range of $5 \leq Re \leq 600$.

This report is split into chapters, with each chapter dealing with a specific aspect of the study under consideration, as described below:

Chapter 2: This chapter presents a detailed review of the literature relevant to the microchannel flows and their simulations.

Chapter 3: This chapter discusses the simulation procedure and the various verification tests performed in the study.

Chapter 4: In this chapter, the results of the simulations are discussed and are compared with the results available in the literature.

Chapter 5: This chapter presents the conclusions that can be inferred from the study along with recommendations for future work.

CHAPTER 2

LITERATURE REVIEW

The serpentine microchannels fabricated using xurography are often known to have a set of abruptly expanding or contracting miter bends. It is necessary to study the effects of these types of channel inaccuracies on the liquid flows in order to design an efficient microfluidic system. CFD simulations of water flows in such microchannels are presented in this report.

An important aspect that needs to be considered while simulating flow in a microchannel is the presence of microscale effects in such flows. In general, the characteristic length of a microfluidic system falls within the range of $10\,\mu\text{m} \leq L_{ch} \leq 200\,\mu\text{m}$ [20] (in the case of channels, $L_{ch} = D_h$). At such small dimensions, the applicability of the continuum assumption is in question, as the number of fluid molecules in a specific volume is relatively low. Should the fluid medium become rarefied, the *no-slip at the wall* assumption is no longer valid and the fluid begins to exhibit a non-zero velocity at the wall. This is one of the microscale effects and the flow regime is known as *slip flow*. To simulate the slip flow using the Navier-Stokes equations, it is necessary to modify the boundary conditions to accommodate the non-zero wall velocity. Further reduction in the characteristic length leads to the *free molecule flow* regime, where the fluid is considered as a collection of molecules rather than a continuous medium. Statistical models are needed to simulate these flows, as presented by Gad-el-Hak in his Freeman Scholar Lecture [21]. In this lecture, it is proposed that the Knudsen number (Kn), defined as

$$Kn = \frac{\lambda}{L_{ch}}, \tag{2.1}$$

where λ is the mean free path of the fluid, is an important parameter for the existence of microscale effects in any flow system. In traditional flows where $Kn \leq 10^{-3}$, the

microscale effects are absent and conventional theory can be used to analyze such systems. Most of the gas flows with the characteristic length in the above-mentioned range fall into the category of $0.1 \geq Kn \geq 0.001$, where the Navier-Stokes equations with modified boundary conditions have been used successfully to simulate such flows [21–23].

2.1 Application of macroscale theory to liquid microflows

Liquids, on the other hand, because of their higher density, have much smaller Kn. The mean free path for liquids is undefined, but in theory, it can be replaced by the lattice spacing (δ) of the liquids [24]. Upon substituting the lattice spacing of water ($\delta = 0.3\,\text{nm}$ [24]) in Eq. (2.1) and setting $Kn = 0.001$, the smallest characteristic length at which the continuum assumption is still valid is $L_{ch} = 0.3\,\mu\text{m}$. The hydraulic diameters of the microchannels used in the present work are well beyond this limit; therefore, microscale effects are not expected to be present in these flows.

In contrast, it has been reported by many researchers that liquid flows in microchannels can also exhibit microscale effects. These researchers used friction factor and pressure drop across the channel as a metric to determine the existence of microscale effects. For example, Papautsky et al. [25, 26] studied the microchannel liquid flows using an array of rectangular microchannels whose hydraulic diameters were in the same range as the channels considered in this report. They reported a 20% increase in the friction factor as compared to conventional theory and attributed this increase to the microscale effects. They have also proposed a numerical model that used micropolar theory and predicts these effects successfully. In the reviews published by Papautsky et al. [27], Morini [28], Koo and Kleinstreurer [29], and Hetsroni et al. [30], the available experiments conducted on liquid flows in microchannels have been discussed in detail. These reviews attributed the discrepancies in the experimental results to the following reasons:

- Ignoring the surface roughness of the fabricated microchannels.
- Ignoring the changes in the dimensions of the final device due to the fabrication procedures.

- Ignoring entrance and exit effects on pressure drop when the pressure taps are placed at the entrance/exit of the channel instead of within the channel.
- Ignoring the temperature change of the fluid in the channel, resulting in the variation of viscosity of the fluid.

Weilin et al. [31] conducted experiments to study the characteristics of water flow in trapezoidal silicon microchannels ($51\,\mu m \leq D_h \leq 169\,\mu m$). They reported that the higher pressure drops are due to the surface roughness of the microchannels. Qu and Mudawar [32] studied the characteristics of a heat sink using rectangular microchannels ($D_h \approx 348\,\mu m$) and deionized water; it was reported that the measured pressured drops were in good agreement with the numerical predictions. Circular and square microchannels ($15\,\mu m \leq D_h \leq 150\,\mu m$) were used by Judy et al. [33] to study the characteristics of pressure drops in microchannels with water, isopropanol, and methanol as the working fluids. Their results indicated that the microscale effects, if present, were within measurement uncertainties and therefore nonexistent. Kohl et al. [34] reported that the friction factor for microflows can be derived from the macroscale data after their study of both gas and liquid microflows in rectangular microchannels ($25\,\mu m \leq D_h \leq 100\,\mu m$). Costaschuk et al. [35] used a rectangular microchannel ($D_h = 169\,\mu m$) fabricated in an aluminum slab to study the pressure drop along the length of the channel. They reported that the discrepancies in the minor loss data were due to inaccuracies in the pressure measurement. Kolekar [16] reported that the pressure drops in the straight sections were in good agreement with the macroscale theory in his study on rectangular microchannels ($150\,\mu m < D_h < 200\,\mu m$) with 90° miter bends. These experiments clearly demonstrated the absence of microscale effects in liquid microflows for $15\,\mu m \leq D_h \leq 348\,\mu m$. Therefore, conventional macroscale theory can be successfully used in simulating water flows in microchannels, when the hydraulic diameter is in the previously mentioned range.

2.1.1 Minor loss coefficients

Pressure losses and the friction factors for microchannel flows are two of the oldest aspects of microfluidics to be under scientific review. These parameters have been used as the metrics for analysis in the experiments conducted by many researchers

[28]. It is now well established that macroscale theory can be used to determine the loss coefficients for microscale liquid flows. The data for straight channels with various cross-section geometries are readily available from the literature [36]. From the macroscale theory, the frictional pressure drop ($\Delta P_{friction}$) across a straight channel with hydraulic diameter D_h can be calculated as

$$\frac{\Delta P_{friction}}{L} = f_D \frac{\rho v_{avg}^2}{2D_h}, \tag{2.2}$$

where f_D is the Darcy-friction factor, ρ is the fluid density, and v_{avg} is the average velocity of the fluid in the channel. Further, the Darcy-friction factor in a rectangular microchannel of aspect ratio (α) for fully-developed laminar flow can be obtained using the Poiseuille number (Po) relation [37]

$$\begin{aligned} Po &= f_D Re \\ &= 96\left(1 - 1.3553\alpha + 1.9467\alpha^2 - 1.7012\alpha^3 + 0.9564\alpha^4 - 0.2537\alpha^5\right). \end{aligned} \tag{2.3}$$

Using Eq. (2.2) and Eq. (2.3), the friction loss coefficients (K_f) can be calculated as

$$K_f = \frac{\Delta P_{friction}}{\frac{1}{2}\rho v_{avg}^2} \tag{2.4}$$

On the other hand, only limited data are available for the excess loss coefficient (K_b) in miter bend microchannels in the literature. Few researchers have determined K_b for a microchannel with m miter bends, which may be calculated by using the equation

$$K_b = \frac{\Delta P_{total} - \Delta P_{friction}}{\frac{1}{2} m \rho v_{avg}^2} \tag{2.5}$$

where ΔP_{total} is the total pressure drop across the microchannel, and m is the number of similar bends in the channel (valid only if the bends are separated by sufficient distance to ignore the effects of an upstream bend).

Lee et al. [38] studied the flow of gases in microchannels with miter bends, curved bends, and double turn configurations. These channels, etched in silicon, were 20 µm wide, 1.1 µm deep, and 5810 µm long with the bend features located in the center.

They reported that the flow rate in the channel containing a 90° miter bend is the lowest in comparison to the other configurations and that the bend angle is a key to the extent of flow separation. Maharudrayya et al. [39] performed CFD simulations of air flow in rectangular serpentine microchannels with miter and curved bends. Their research was focused on studying the effects of Reynolds number, aspect ratio, curvature ratio (C), and the distance between the bends on bend excess loss coefficient (ξ), defined as

$$\xi = K_b - 4 f_D C \theta \tag{2.6}$$

where θ is the angle of bend in radians. As $C = 0$ for miter bends, from Eq. (2.6), $\xi = K_b$. It was reported that the flow development length is a function of Re, α, and the upstream effects, such as the presence of a bend. Further, with the increase in α and C of the channel, the flow distortion at the bend decreased. The flow separation at the bend decreased with the decrease in the separation distance from the upstream bend and K_b is the highest for the miter bends.

Kockmann et al. [40] performed numerical simulations of the flow in microchannels with bends and T-joints to analyze the transport phenomena (heat transfer and mixing characteristics) of these channels. They used two channels with $D_h = 100\,\mu m$ and $500\,\mu m$ to study the mixing characteristics of the microchannels as a function of channel size and diffusion distance. It was reported that the mixing characteristics of smaller channels is higher due to the small diffusion distance when compared to larger channels. Further, it was reported that the vortex pair induced at the bend enhances the mixing quality and heat transfer rate in the outlet channel.

Haller et al. [41] used a set of L-shaped, T-joint, and fork-shaped microchannels to study the effects of different shapes of bends on pressure losses and the heat transfer characteristics. They used water as the test fluid and employed experimental as well as computational methods to study the pressure distribution in various planes along the outlet channel. It was reported that stronger vortices developed at a miter bend, enhancing the heat transfer rate when compared to those with curved bends. It was also reported that hot spots are observed in miter bend channels as a result of

recirculation zones.

Xiong and Chung [42,43] performed experiments on a set of serpentine microchannels with miter bends separated by an *unmentioned* distance. The hydraulic diameters of these channels were 209 µm, 412 µm, and 622 µm with $\alpha \approx 1$. They used an additional set of straight microchannels of equal hydraulic diameters and approximately 4 mm and 120 mm long, to experimentally estimate the pressure drop in a straight channel without the entrance and exit effects. They reported that the experimental Poiseuille number for straight channels is in good agreement with the conventional laminar theory predictions up to an $Re = 1500$. The $K_b = 1.1$ from the macroscale is not valid for the microchannels, and is dependent only on Reynolds number for $Re < 100$, while for $Re > 100$, channel size also effects K_b, which remains constant for $Re > 1000$.

Kolekar [16] used rectangular xurographic microchannels with two miter bends to study the characteristics of bend excess loss coefficients as a function of aspect ratio and Reynolds number. In the range of $250 \leq Re \leq 1000$, it was reported that K_b increases linearly with Re and remains almost constant up to the critical Reynolds number (Re_{cr}), at which point K_b suddenly decreases. Further, K_b increased with increasing α of the channel and the Reynolds number, at which the maximum value of K_b occurs, increased with the decrease in α.

Herwig et al. [44] developed a second law analysis approach to the determination of losses, applicable to any configuration of conduit components and channels in general, and derived a relation for K_b as a function of Re. This relationship was tested for the cases of laminar flow in microchannels with 0°, 180°, and 90°/90° double bends in addition to the 90° single bend, all of which were smoothly curved, using CFD simulations for $4 \leq Re \leq 512$. In the case of a 90° single smooth bend, it was reported that K_b increases with Re and for low Re, the major losses are within the bend while for higher Re, downstream losses contribute most to K_b (up to 70% for $Re = 512$). In addition to K_b, they also provided the upstream and downstream lengths of the channel in which the flow distortion effects due to bends are observed.

The above studies have made a significant contribution towards understanding the flow characteristics of microchannels with miter bends. Sufficient data for K_b as

a function of Reynolds number, curvature ratio of the bend, and separation distances between bends were reported. These experiments also brought our attention to one other interesting parameter, area ratio A_r of the microchannels at the bends, caused by the fabrication defects. The pressure drop across such channels is derived by using the integral first law equation [45], given as

$$\phi = \Delta P_{io} + \frac{1}{2}\rho(\beta_i {v_i}^2 - \beta_o {v_o}^2) + \rho g(z_i - z_o), \tag{2.7}$$

and

$$\beta = \frac{\int_A v^3 dA}{v_{avg}^3 A} \tag{2.8}$$

where β is the nondimensional constant dependent on velocity distribution at a given plane and ϕ is the total pressure loss in the channel. Assuming that the inlet and outlet are held at the same altitude (i.e., $z_o = z_i$), rearranging the terms in Eq. (2.7) results in the following equation for head loss

$$\phi = \Delta P_{io} + \frac{1}{2}\rho(\beta_i {v_i}^2 - \beta_o {v_o}^2) \tag{2.9}$$

The ϕ term derived from the above equation includes pressure loss due to channel wall friction as well as other features likes bends. The pressure loss due to a bend is therefore derived as

$$\Delta P_{bend} = \phi - \Delta P_{friction} \tag{2.10}$$

and the bend excess loss coefficient for an expansion or contraction channel as

$$K_{be}(\text{or})K_{bc} = \frac{\Delta P_{bend}}{\frac{1}{2}\rho v_{avg,i}^2} \tag{2.11}$$

If the cross-sectional geometry of the channel at the inlet is the same as that of the outlet, then $\beta_i = \beta_o$. Then Eq. (2.9) is simply the total pressure drop across the microchannel, and Eq. (2.11) yields the same value as that of Eq. (2.5) (i.e., K_b).

A few researchers studied the effect of area changes on the loss coefficient in straight channels. Abdelall et al. [46] performed an experimental study on flow through straight circular channels with a sudden expansion or contraction. The hydraulic diameters of the two sections were 1.6 mm and 0.84 mm, respectively, and the test fluids were air and water at room temperature and atmospheric pressure. Minor loss coefficients for expansion and contraction channels were reported for water in the range $870 \leq Re \leq 12,960$(Re is based on the small channel diameter). It was reported that the contraction losses were slightly larger than the theoretical predictions. Chalfi [47] used a similar arrangement to study the minor loss coefficients, due to expansions and contractions in a straight channel, and compared his results to the conventional one-dimensional theory. He reported the loss coefficients for single-phase air and water as well as two phase flows using experiments and CFD simulations. For single-phase water flows in the laminar regime, $160 \leq Re \leq 539$, it was reported that the experimental K_c were in agreement with theory. However, K_e was not in agreement with theory, ruling out the applicability of the one-dimensional theory for the prediction of K_e and K_c in straight channels.

Further investigation into the characteristics of K_e and K_c in straight channels was conducted by Torgerson [48]. He used straight rectangular microchannels, fabricated by xurography, to study the minor losses as a function of Re and A_r. In his experiments, a straight rectangular microchannel with nominal width of 300 µm and height of 105 µm was incorporated with abrupt expansions and contractions in the range $2 \leq A_r \leq 5$ (in his study, $A_r > 1$). Data for loss coefficients were collected for water flows in the range of $250 \leq Re \leq 3500$. It was reported that K_{be} decreases rapidly with increasing Re up to the critical Reynolds number and the losses are higher for channels with lower A_r in the laminar regime. In the case of contraction channels, K_{bc} decreased much more gradually with the Re and developed a logarithmic correlation between K and Re.

The above investigations, when put together, provide a significant amount of data for K_e and K_c in straight channels and their dependence on the area ratio and the Reynolds number. Nguyen [17] extended the work of Torgerson [48] to microchannels with 90° miter bends. In his experiments on water flows in the range of $100 \leq Re \leq$

3200, he used xurographic rectangular microchannels with miter bends whose nominal dimensions are similar to those used by Torgerson [48]. K_b are reported to be in good agreement with those reported by Torgerson [48]. A relation for bend loss coefficients was developed as a function of A_r and Re.

From the above review, it is evident that a limited amount of data for K_e and K_c in microchannels is available in the literature. Furthermore, the data for K_{be} and K_{bc} are further limited to a few values of large A_r (1.5, 2, and 3) and high Re. The data for minor aberrations in the area (i.e., $A_r = 1.1$ or 0.9), which is prominently observed in the xurographic microchannels, are not available. Further, the experimental data do not quantify the effect of surface roughness on the loss coefficients. In order to develop an accurate model for K_{be} and K_{bc} as a function of A_r and Re, the data for minor aberrations in area and low Reynolds numbers are necessary. Therefore, in the present work, computational methods are used to study the characteristics of bend excess loss coefficients in the microchannels with abrupt expansions and contractions, whose area ratios are in the range of $0.33 \leq A_r \leq 3$, in the laminar regime with $5 \leq Re \leq 600$. Simulation of flows also helps to avoid the effect of channel roughness on the results. In all of these simulations, A_r is defined using Eq. (1.4) and Re and K are calculated based on the inlet channel dimensions regardless of the presence of an expansion or contraction in the channel.

2.1.2 Flow development length

Flow development length is another important aspect in designing microchannel systems. Knowledge of flow development length is important in the design of microchannels with multiple bends [39,42,43], when Eq. (2.5) is used to calculate the loss coefficient. If the distance separating two bends is not sufficient to accommodate the effects of both the upstream and downstream bends, the the flow at the downstream bend will be different than that in the rest of the microchannel [44]. In the review of macroscale theory for duct flow by Shah and London [37], the entrance length (L_e) in a channel with hydraulic diameter (D_h) and $\alpha = 1$ can be calculated as

$$L_e = 0.09 D_h Re. \tag{2.12}$$

According to this relationship, the development length for a flow with $Re = 600$ and $D_h = 200\,\mu m$ is estimated to be $10.8\,mm$, which is far greater than the L_e observed experimentally in microchannels. One reason for this discrepancy is that the experimental flows have been predeveloped when entering the channel and the other due to the high shear rate between the microchannel fluid layers, which is a function of Re as well as α.

Ahmad and Hassan [49] conducted micro-PIV experiments to study the effects of scaling on the entrance lengths in microchannels. They used square microchannels with $D_h = 500\,\mu m, 200\,\mu m$, and $100\,\mu m$ and water flowing at $0.5 \leq Re \leq 200$. They reported that L_e for $Re > 10$ is in good agreement with the conventional theory from the literature [37]. They also performed a curve-fit to the experimental data and proposed a modified entrance length equation as

$$\frac{L_e}{D_h} = \frac{0.6}{0.14Re + 1} + 0.0752Re \tag{2.13}$$

for microchannels with $\alpha = 1$. As the number of data points used in this curve fit is small (6) and channels with a single α are used, Eq. (2.13) closely resembles the conventional correlation (see Fig. (2.1)).

For microchannels with $\alpha \neq 1$, the entrance length as a function of α and Re was proposed by Martinelli and Viktorov [50], by curve-fitting the entrance length data from CFD simulations, as

$$L_e = Re\left[0.016 + 0.157\alpha - 0.129\alpha^2\right] h, \tag{2.14}$$

and

$$\alpha = \frac{h}{w} \tag{2.15}$$

where h is the height of the channel. L_e obtained using Eq. (2.14) and Eq. (2.15) is within 4% of the entrance lengths determined in the experiments conducted by Martinelli and Viktorov. Rectangular microchannels with $0.125 \leq \alpha \leq 1$ were used

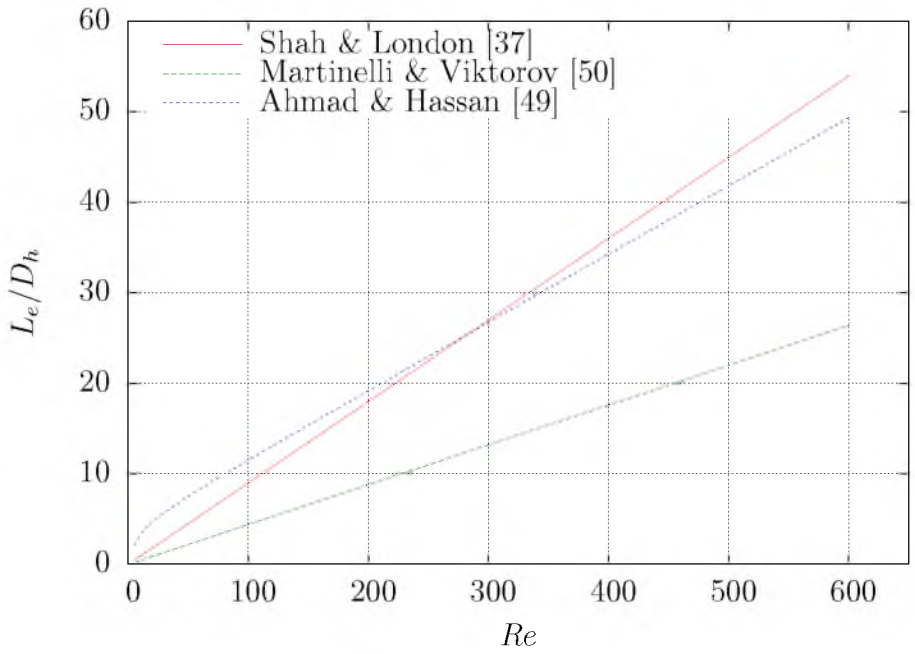

Figure 2.1: **Flow development length from literature:** The plot shows a comparison of the flow development lengths models available in the literature for a straight rectangular microchannel whose $D_h = 200\,\mu\text{m}$ and $\alpha = 1$.

in simulating the flows for $100 \leq Re \leq 2000$. Using Eq. (2.14), for the case with $Re = 600$, $D_h = 200\,\mu\text{m}$ and $\alpha = 1$, L_e was found to be 5.3 mm, which is about 50% of that obtained from Eq. (2.12). A comparison of development length predicted by the above three models is shown in Fig. (2.1) over the range of $5 \leq Re \leq 600$.

In the present simulations, the length of the outlet channel is set conservatively using Eq. (2.12) to ensure fully-developed flow at the outlet, even though a much smaller outlet length is proposed by Martinelli and Viktorov. The results for the development lengths in the outlet channels following the 90° miter bend for these simulations are presented in Chapter 4 alongside the L_e data obtained from Eq. (2.14).

2.2 Summary

In the past decade, many researchers have studied the flow characteristics of straight microchannels and provided sufficient data to support the argument that the loss coefficients, flow development lengths, and friction factors are in agreement with the conventional macroscale theory and correlations. A few researchers have extended these studies to microchannels with sharp bends and bends with different

curvature ratios and configurations. Advances in rapid prototyping technologies and the ease of fabricating complex channel systems are the motivating factors behind these studies. Some of these investigations reported data on parameters like the dimensions of recirculation zones at the bends, bend excess loss coefficients, and flow development lengths.

Xurography is a rapid prototyping technology, used to fabricate microchannels from thin films. A review of the literature has shown that the serpentine microchannels fabricated using xurography often result in undesired abrupt expansions or contractions at the bends. A few experimental studies have been conducted to explore this aspect of the xurographic serpentine microchannels. These experiments were limited to higher area ratios for the expansions or contractions. Unfortunately, data obtained from these experiments were highly inaccurate in characterizing the loss coefficients because of imprecise measurement of channel dimensions and pressure drops. Further, additional frictional losses due to surface roughness resulting from fabrications defects are unaccounted for in the data reduction.

In order to address the above-mentioned issues in previous experiments, a computational investigation is conducted on liquid flows in rectangular microchannels with and without abrupt expansion or contraction at the miter bend. A comprehensive set of microchannels whose parametric dimensions are in the range $100\,\mu\text{m} \leq D_h \leq 188\,\mu\text{m}$, $0.2 \leq \alpha \leq 1.0$, and $0.33 \leq A_r \leq 3$ are used in these simulations. The bend excess loss coefficients for miter bends with and without expansion or contraction are the focus of this investigation along with the flow development length in the outlet channel.

CHAPTER 3

SIMULATION

CFD packages, both commercial and open source, are widely used by researchers to perform numerical simulations of liquid and gas microflows. Clear knowledge of the applicability of macroscale theory to liquid microflows paved the way for this approach for the microflow analysis. CFX [39], CFD-ACE+ [40, 41, 51, 52], Open-FOAM [44], and Fluent [50, 53, 54] are among the most frequently used flow simulation packages. Details of the simulation procedure for water flow in rectangular microchannels with miter bends featuring abrupt expansions or contractions using Fluent and Gambit are presented in this chapter.

3.1 Methodology

3.1.1 Governing Equations

In general, the laminar flows can be accurately simulated by solving just the mass and momentum conservation equations of the Navier-Stokes equations, with the boundary conditions appropriate to such scenarios, assuming constant temperature. These equations can be simplified further, when simulating incompressible and isothermal flows (ρ and μ of the fluid remain constant in the flow domain), which is the case in the present study. Moreover, to estimate the excess pressure losses in the channels, the flows are assumed to be steady state, which eliminates time from the list of variables. The Navier-Stokes equations after applying these simplifications are reduced to the following equations.

$$\textbf{Momentum conservation:} \qquad \rho\vec{v}.\nabla\vec{v} = -\nabla P + \mu\nabla^2\vec{v} \tag{3.1}$$

$$\textbf{Mass conservation:} \qquad \nabla\vec{v} = 0 \tag{3.2}$$

Since the flow is laminar and isothermal for all cases in the study, the energy conservation equation need not be solved in the solution procedure. The above governing equations when discretized over a regular cartesian control volume using linear schemes transform into a set of coupled algebraic equations

$$\sum_{f}^{n} \vec{v_f} \left(\rho \vec{v_f} . \vec{A_f} \right) = \sum_{f}^{n} \nabla P_f . \vec{A_f} + \mu \sum_{f}^{n} \nabla \vec{v_f} . \vec{A_f} \tag{3.3}$$

$$\sum_{f}^{n} \vec{v_f} \vec{A_f} = 0 \tag{3.4}$$

where n is the number of faces of the control volume, $\vec{A_f}$ is the area vector normal to the face f, P_f is pressure on the face f, and $\vec{v_f}$ is the velocity normal to face f of the control volume. Higher order discretization schemes are frequently used in the simulations, and are discussed in the following section.

3.1.2 Discretization schemes

Linear discretization is one of the simplest schemes available in the literature. In this scheme, the cell center properties are linearly related to the properties on the walls of control volume in the finite volume method. The accuracy of the final solution is dependent on the cell size when linear schemes are employed. When applied to the Navier-Stokes equations, these schemes result in a checker board form of pressure distribution [55], which is practically impossible. Further, linear schemes, like upstream differencing, result in numerical diffusion when the flow is not aligned with the control volume faces. Therefore, a higher order discretization scheme is needed to overcome such impractical solutions and to obtain greater accuracy when using an optimal cell size for the domain.

Many higher-accuracy schemes have been developed by researchers and successfully applied to a variety of flow scenarios. For example, the *Pressure Staggering Option* (PRESTO) available in Fluent for pressure discretization [56] is based on the staggered mesh scheme developed by Patankar [55]. PRESTO provides a better way to relate the pressure at the cell center with those on the faces when compared to

linear and second-order discretization schemes. It is also known to provide greater accuracy for vortex flows even when using larger cells. The second-order, QUICK, and Third-MUSCL are the higher-order schemes available in Fluent for momentum discretization. The Quadratic Upstream Interpolation for Convective Kinematics (QUICK) scheme was developed by Leonard [57]. QUICK is known for its greater accuracy in comparison to central-differencing scheme while retaining the stable convection sensitive properties of an upstream-differencing scheme for most of the flow scenarios. However, in his later work, Leonard [58] highlighted QUICK's lack of accuracy in determining the sudden changes in a function, e.g., a step function at $Re = 200$. This negative feature is critical in the present study to determine the shape of the recirculation zone accurately using an optimal cell size. Therefore, a third-order MUSCL scheme is used to discretize the momentum equation for the simulations in the present study. This scheme is reported to provide better accuracy in the recirculation zones [59,60]. There are many variants of MUSCL schemes available in the literature; Fluent's version is closely based on the early method developed by van Leer [59].

In summation, the PRESTO and third-order MUSCL schemes are used for the pressure (mass) and momentum discretization, respectively, for simulating flows in the present study. Upon applying these schemes to Eq. (3.1) and Eq. (3.2), a set of coupled algebraic equations are generated of the form

$$a_p \phi_p = \sum_{nb} a_{nb} \phi_{nb} + b, \tag{3.5}$$

where a is the coefficient derived from the discretization scheme, ϕ is the velocity or pressure depending on the equation, p refers to the property at the cell center and nb refers to the properties on the neighboring cell faces, and b is the source term.

3.1.3 Solution algorithm

The set of algebraic equations, represented by Eq. (3.5), can be solved either by a direct or an iterative method. The iterative methods provide a clear advantage over direct methods, as they need lower memory to perform the calculations. In the case of the Navier-Stokes equations, there is strong coupling between the momentum

and mass conversation equations, the effect of which is dependent on the Reynolds number of the flow. Segregated algorithms such as SIMPLE decouple these equations and solve them sequentially; this algorithm is explained in detail by Patankar [55]. This approach has a clear advantage over the coupled schemes due to its simplicity, which results in faster calculations and low memory requirements [61]. However, as the Reynolds number increases due to strong coupling effects, the convergence rates of segregated algorithms are poor when compared to the coupled algorithms. Fluent's coupled algorithm is based on the fully-coupled implicit algorithm developed by Vanka [62].

In the following example, the convergence time for SIMPLE and the coupled-implicit algorithm is tested for a sample case of a microchannel with a miter bend, a 300 µm x 100 µm cross-section, and inlet and outlet channel lengths of 3 mm and 10 mm, respectively. A hydrodynamically fully-developed velocity profile was used at the inlet for an inlet-based $Re = 200$. The flow domain was discretized with a structured and uniform cell size of 5 µm, resulting in a total of 2173500 cells. The simulation was run on a server using a single processor clocked at 2.5GHz and a physical memory of 65GB. The convergence criteria was set to the scaled continuity residual $R_s^c \leq 10^{-7}$. Fig. (3.1) shows the plot of scaled residuals for SIMPLE and coupled-implicit algorithms.

The number of iterations for convergence is higher for the SIMPLE algorithm. It took approximately 5.1h for the SIMPLE algorithm to converge to the solution using 2.9% of the physical memory while the fully-coupled implicit algorithm needed only 1h 40min to converge. However, the memory needed by the coupled implicit algorithm is more than double ($\approx 6.1\%$) the memory needed for SIMPLE. Further, the convergence time of SIMPLE increases with Re of the simulated flow. In the present work, due to the abundance of the physical memory, the fully-coupled implicit algorithm is used to save simulation time. The convergence rate is further accelerated by using multigrid methods [63] and parallel execution. Fluent offers an option to use the interpolated solution from a previous simulation as the initial guess for the next simulation. This option further reduces the number of iterations to solution convergence. By using these options, the simulation time for the coupled-implicit

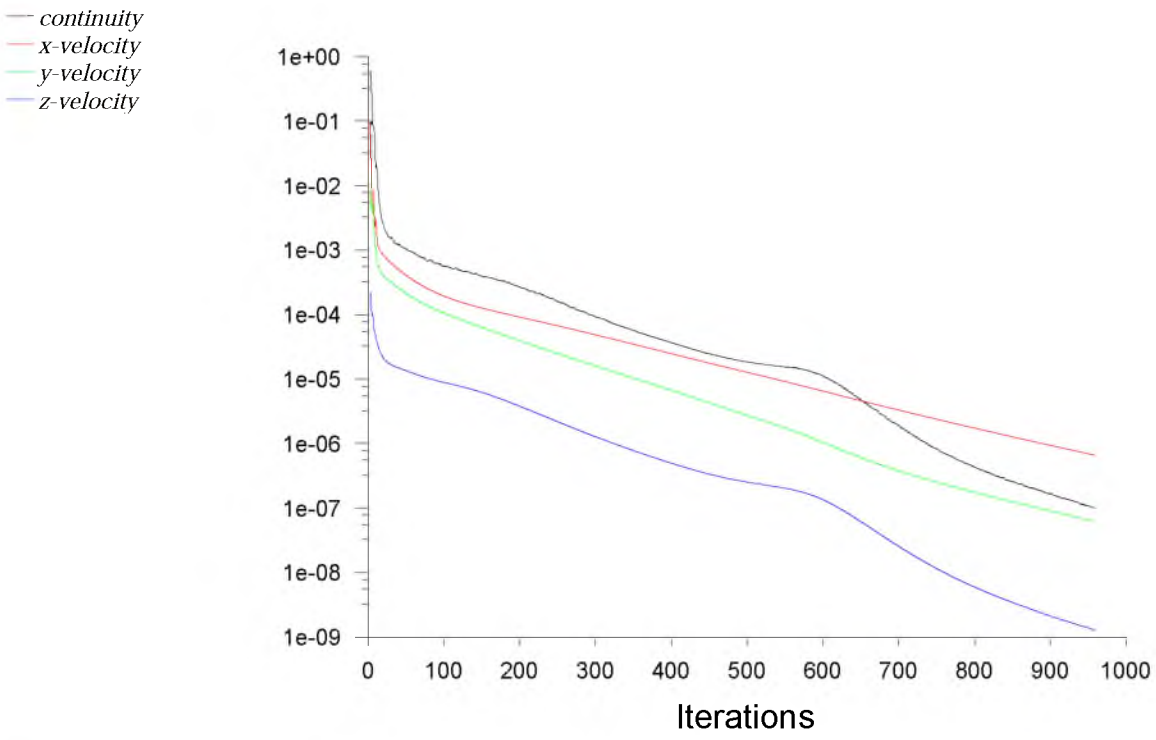

(a)

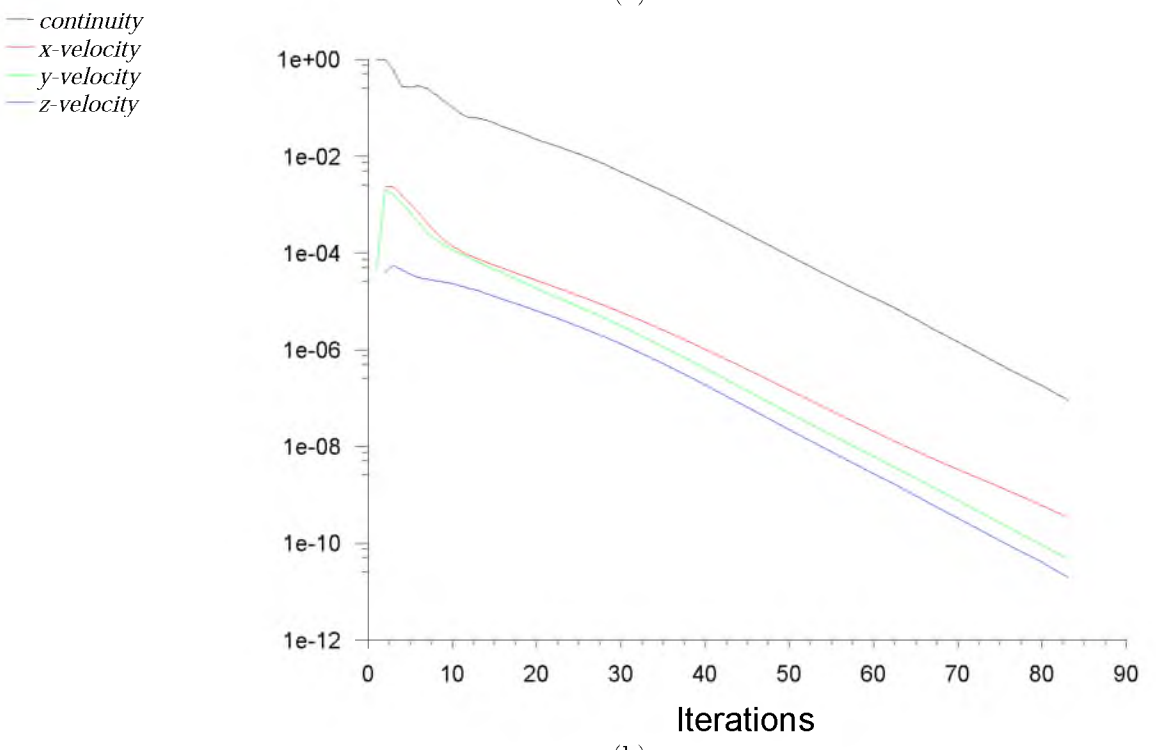

(b)

Figure 3.1: **Convergence rate of solution algorithm:** The images show the scaled residuals of continuity, x, y, and z-*velocities* for two solution algorithms plotted against the number of iterations. (a) SIMPLE. (b) Coupled-Implicit.

algorithm for the same $Re = 200$ was reduced to less than one hour.

3.2 Flow domain

In the present work, the flow domain can be divided into three categories based on the area ratios at the miter bends. The microchannels with $A_r > 1$, $A_r = 1$, and $A_r < 1$. In the first two categories, the inlet channel is 3 mm long, while in the last category, it is 5 mm. The outlet channel is longer for $A_r < 1$ to capture the effects associated with the flow acceleration, and the lengths are set using Eq. (2.12) and the hydraulic diameter of the outlet channel. This is done to ensure that the outlet channel is long enough to capture the downstream effects of the miter bend.

Many researchers have used a uniform mesh in the bend region, with a nonuniform mesh in both the inlet and outlet channels [40, 50, 51]. In this approach, the size of an element in the nonuniform region is gradually increased in the flow direction. The advantage of using this approach is that the number of cells in the domain is significantly reduced, thereby reducing the simulation time. The key to success in this approach is the location at which the transition in cell size begins. If the cell size transition begins early in the channel, where the flow is highly multidimensional, the simulation produces highly erroneous results. Therefore, the present work employs a uniform structured mesh to discretize the channel domain. A uniform boundary layer, with ten rows beginning at 1 µm and growing at a rate of 1.19, is attached to the side and bottom walls of the channel (see Fig. (3.2) for the wall notation). The mesh on the symmetry wall of the channel is as shown in Fig. (3.3), where the structured mesh is slightly distorted to accommodate the boundary layer. This distortion effect is very small on the final solution and therefore can be neglected. The entire process of meshing is conducted using the preprocessing package, Gambit 2.4 [64]. The symmetry wall does not have a boundary layer attached to it in all the channels used in these simulations.

3.2.1 Boundary conditions

The Reynolds number Re is used as a parameter in the flow simulations. The average velocity at the inlet of the channel is calculated from the Re definition, as shown in Eq. (1.1). The boundary conditions commonly used in computational

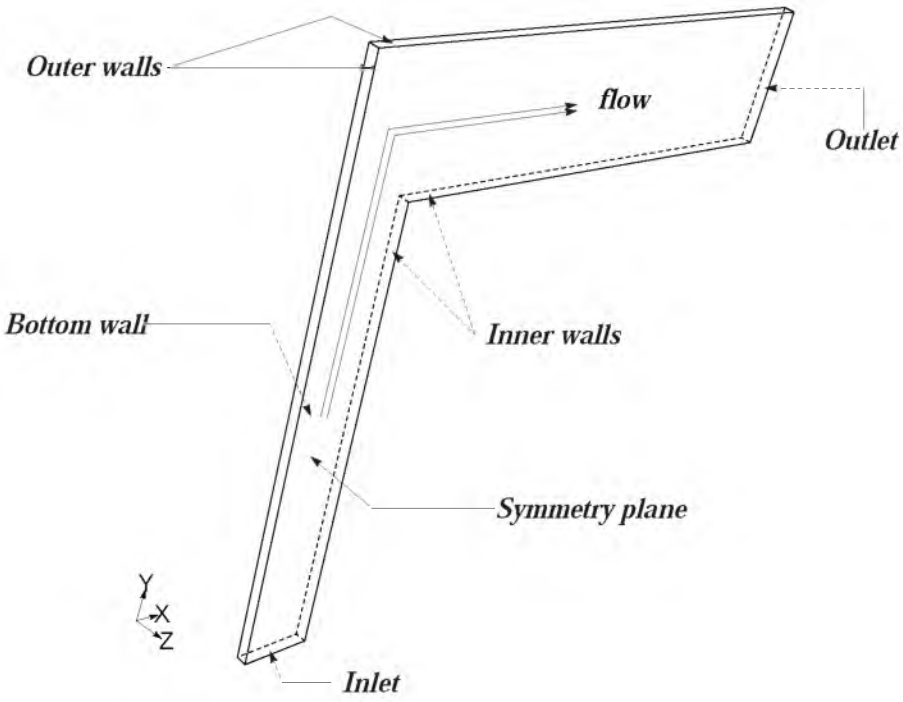

Figure 3.2: **Walls in the flow domain:** The image shows the wall notation of the microchannel flow domain used in this report.

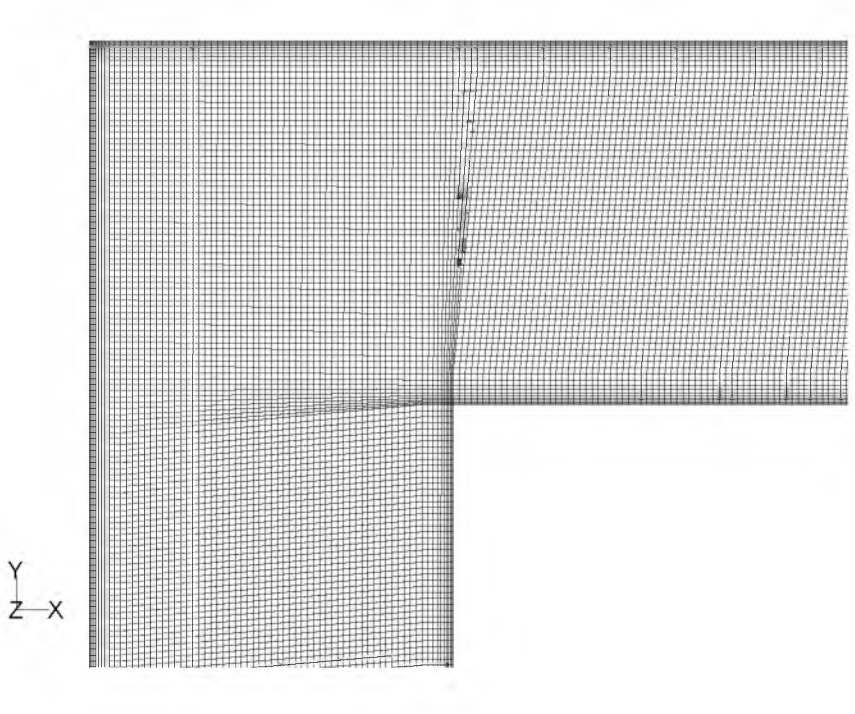

Figure 3.3: **Mesh generation scheme:** This image shows the mesh on the symmetry wall at the miter bend, along with the boundary layers.

simulations are:

- isothermal,
- a uniform velocity at the inlet,
- atmospheric pressure at the outlet, and
- no slip at the walls.

In order to calculate the excess pressure loss due to the presence of a miter bend in the microchannel, the flow needs to be

- steady, and
- hydrodynamically fully-developed

before it encounters the bend as well as the outlet. This implies that the inlet and outlet channels should be longer than L_e, as derived from Eq. (2.12), to accommodate flow development and bend effects [44]. This approach doubles the number of cells in the flow domain, increasing computational resources significantly; hence, it is undesirable.

A better alternative is to assume a fully-developed velocity profile at the inlet, instead of uniform velocity, as proposed by Spiga and Morini [65]. With this assumption, only a small inlet channel (3 mm or 5 mm, depending on A_r) is required to accommodate the upstream effects of the miter bend. The profile is given by the analytical expression [65]

$$\bar{v}(x,y) = \frac{v(x,y)}{v_n} = \frac{16\beta^2}{\pi^4} \sum_{n\ odd}^{\infty} \sum_{m\ odd}^{\infty} \frac{\sin(n\pi\frac{\xi}{a})\sin(m\pi\frac{\eta}{b})}{nm(\beta^2 n^2 + m^2)} \tag{3.6}$$

where $\bar{v}(x,y)$ is the normalized velocity at a location (x,y) in the inlet cross-section and v_n is the normalizing constant derived using the average velocity

$$v_n = \frac{v_{avg}\pi^6}{64} \frac{1}{\sum_{n\ odd}^{\infty} \sum_{m\ odd}^{\infty} \frac{1}{n^2 m^2 \left(n^2 + \frac{m^2}{\beta^2}\right)}} \tag{3.7}$$

where v_{avg} is calculated by using the Eq. (1.1). A test simulation was performed to check the accuracy of this velocity profile using 75 modes for m and n, the details of which are presented in Section 3.3.1. In addition to the above boundary conditions, a symmetry plane is present in the x-y plane as shown in Fig. (1.4) between the top and bottom walls [40,44] of the microchannel (see Fig. (3.2)). By using the symmetry boundary condition, the flow domain is reduced by half, reducing the simulation time and resources. From this point forward, the cross-section of the channel is always mentioned in full, even though the simulation is performed on half of the section; i.e., if the cross-section is 300 µm wide and 100 µm thick, the simulation uses a domain of 300 µm wide and only 50 µm thick, using the symmetry boundary condition.

3.2.2 Fluid properties

Density and viscosity of water are the only properties needed in the simulation as the flows in the present work are assumed to be incompressible and isothermal. These properties are obtained using the following curve-fit equations, as presented in [66].

$$\begin{aligned}\rho = (1.4385 \text{ x } 10^{-8})T_{avg}^5 - (1.8895 \text{ x } 10^{-6})T_{avg}^4 + (1.2318 \text{ x } 10^{-4})T_{avg}^3 \\ - (9.2686 \text{ x } 10^{-3})T_{avg}^2 + (6.6821 \text{ x } 10^{-2})T_{avg} + 999.8748\end{aligned} \tag{3.8}$$

$$\begin{aligned}\mu = -(1.3109 \text{ x } 10^{-12})T_{avg}^5 + (2.7464 \text{ x } 10^{-10})T_{avg}^4 - (2.5655 \text{ x } 10^{-8})T_{avg}^3 \\ + (1.4718 \text{ x } 10^{-6})T_{avg}^2 - (6.0390 \text{ x } 10^{-5})T_{avg} + 1.7866 \text{ x } 10^{-3}\end{aligned} \tag{3.9}$$

where T_{avg} is the temperature of water in $°C$, ρ is in $\mathrm{kg\,m^{-3}}$ and μ is in $\mathrm{N\,s\,m^{-2}}$. The temperature range for the ρ curve-fit is $-20°C \leq T_{avg} \leq 46°C$ while that of μ is $0°C \leq T_{avg} \leq 50°C$. The properties of water at $22.5°C$ are used in these simulations, as shown in Table (3.1).

Table 3.1: **Properties of water**: The density and viscosity of water at $22.5°C$.

Name	ρ ($\mathrm{kg\,m^{-3}}$)	μ ($\mathrm{N\,s\,m^{-2}}$)
Water	997.78	0.0009772

3.3 Validation and convergence tests

3.3.1 Hydrodynamically fully-developed velocity profile

Laminar water flow is simulated in a straight microchannel 25 mm long with a cross-section of 300 µm x 100 µm. The length of the channel is greater than the development length (L_e) calculated from Eq. (2.12) for $Re = 200$. This ensures that the velocity at the outlet of the channel is hydrodynamically fully-developed. A uniform velocity (v_{avg}) is assumed at the inlet of the channel and the other boundary conditions are set as described in the previous section. The axial component of the velocity at the outlet is extracted from the simulation and compared to the hydrodynamically fully-developed velocity calculated from Eq. (3.6), which is shown in Fig. (3.4). The root mean square value of the difference between the analytical calculated velocity profile and that of the simulation is 2.3%. As reported by Herwig et al. [44], for a microchannel with a curved 90° bend, the effects of the bend are observed up to a distance of $\approx 0.3D_h = 30$ µm for $D_h = 100$ µm. For the microchannels with the miter bends, this distance is expected to be slightly higher, but the inlet length of 3 mm or 5 mm used in the present simulations is sufficient to accommodate this distance as well as the differences in the velocity profile condition boundary condition. Therefore, it is concluded that the velocity calculated by using Eq. (3.6) can be used as the inlet velocity boundary condition for the simulations.

3.3.2 Grid independence

The solution to the linear algebraic equations defined in Eq. (3.5) has an approximation error, which is a function of the cell size and Re. In order to obtain an accurate solution with a minimum approximation error, it is necessary to find a mesh resolution beyond which the solution is independent of the cell size. Therefore, a set of flow simulations is performed on a microchannel domain by systematically increasing the mesh resolution. The flow properties like pressure drop, mass flow rate, etc., are then evaluated and evaluated as a function of the domain resolution, as shown in the Fig. (3.5). A microchannel with a cross-section of 200 µm x 100 µm, and 3 mm and 10 mm long inlet and outlet channels, respectively, is used to evaluate the grid dependence of the solution. The grid resolution, cell size, and the number of cells for each resolution are shown in Table (3.2). The pressure drops (f_x) across the

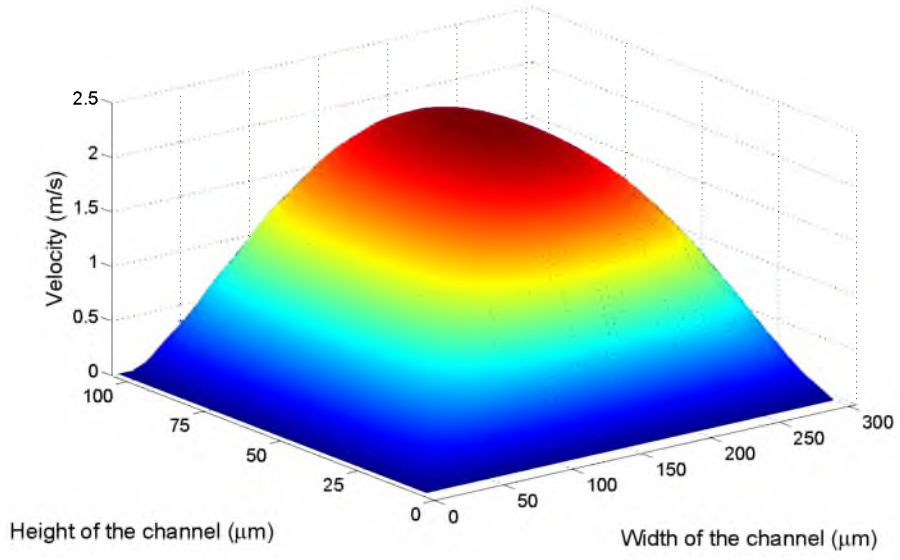

Figure 3.4: **Hydrodynamically fully-developed velocity profile:** The image shows a hydrodynamically fully-developed inlet velocity profile for a rectangular channel with a cross-section of 300 µm x 100 µm at $Re = 200$ as proposed by Spiga and Morini [65].

channel are shown in Table (3.3) along with the mesh resolution for $Re = 500$.

As shown in Fig. (3.5), the estimation of pressure drop significantly increases ($\approx 2.4\%$) by reducing the cell size from 10 µm to 5 µm, while the number of cells in the domain increases from 132,000 to more than a million. Further reducing the cell size to 2.5 µm increases the pressure drop by another 0.6%; however, this improvement requires over eight million cells. The simulation's computation time in the f_1 case is more than ten hours even with parallel execution. A Richardson's extrapolation is performed to obtain the pressure drop f_0 when the cell size approaches to zero using the pressure drop f_x values from the simulations. This analysis indicates that the value of f_2 is within 0.9% of the value of f_0. Considering the optimal simulation time and the accuracy of f_2, the simulations are performed using a structured uniform cell size of 5 µm.

The mass flow rates at the inlet and the bend are shown in Fig. (3.6) as the resolution of the domain is increased, in addition to the theoretical mass flow rate for $Re = 500$. The difference between the theoretical value and the mass flow rate at the bend is reduced by 0.62%, when the cell size is reduced by half from 10 µm to

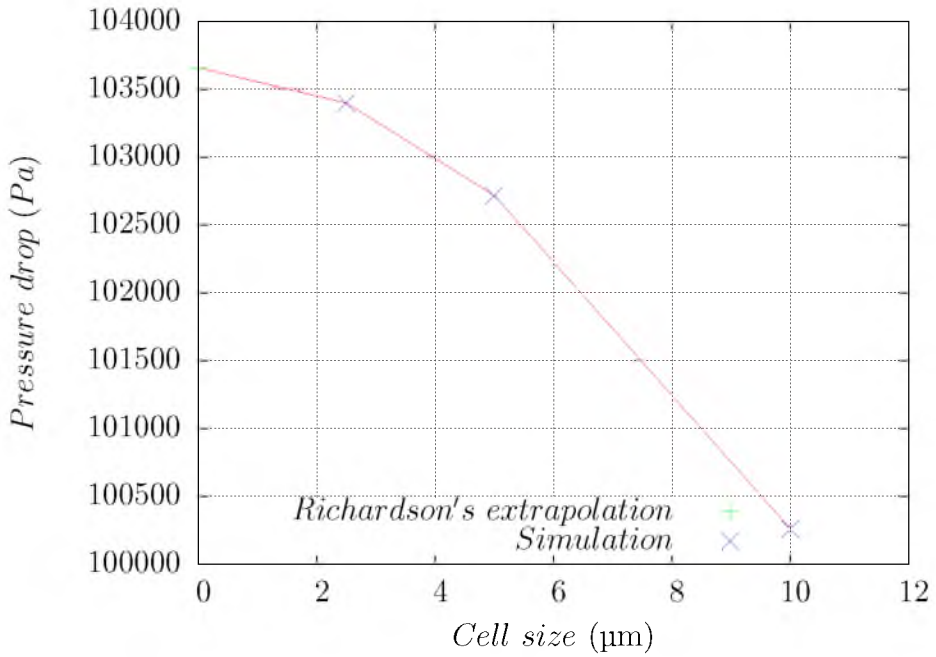

Figure 3.5: **Change in pressure drop with mesh resolution:** The plot shows the pressure drop across a microchannel at different mesh resolutions and the extrapolated value as the cell size $\rightarrow 0$.

Table 3.2: **Resolutions for grid independence analysis:** Total number of cells in the domain with the mesh resolution.

Mesh resolution	Cell size (µm)	Number of cells
100 nodes/mm	10	132,000
200 nodes/mm	5	1,056,000
400 nodes/mm	2.5	8,448,000

Table 3.3: **Grid independence analysis (Pressure drop):** Pressure drop across the microchannel as a function of mesh resolution.

Variable name	Cell size (µm)	Pressure drop(Pa)
f_3	10	100257.89
f_2	5	102716.28
f_1	2.5	103397.66
f_0	0(Richardson's Extrapolation)	103658.75

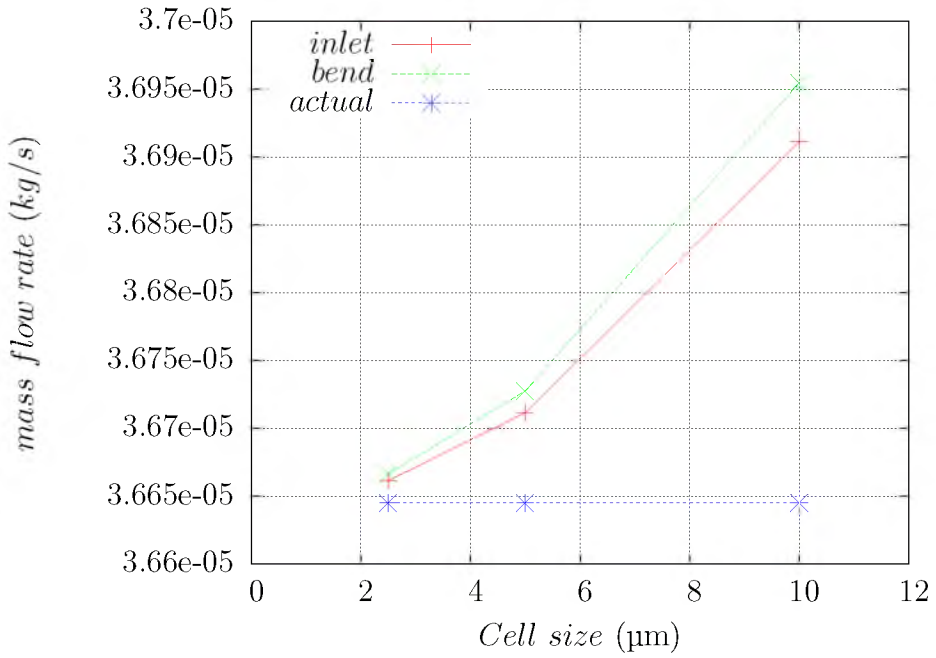

Figure 3.6: **Mass flow rate with mesh resolution:** The plot shows the mass flow rates at the inlet and the bend at different mesh resolutions along with the theoretical value for $Re = 500$.

5 µm. As the cell size is reduced to 2.5 µm, the difference in mass flow rates is reduced to 0.16%, but the simulation time is increased to more than ten hours. Further, the velocity magnitudes are compared the mesh resolutions. Fig. (3.7) shows the velocity magnitude along line (see Fig. (3.8)) in the recirculation zone 0.1 mm downstream of the miter bend for three cell sizes. Clearly, the velocity magnitudes from the coarsest grid fails to provide a sufficient accuracy in the primary recirculation zone, while the velocity magnitudes for the cell sizes of 5 µm and 2.5 µm are almost identical with an average difference of 2.5%.

From this analysis, it is evident that the accuracy of the simulations are highest when the cell size = 2.5 µm, very closely followed by the cell size of 5 µm. However, the time and computational resources needed for the simulations are significantly higher for the 2.5 µm cell size when compared to the 5 µm cell size, for a very small gain in accuracy. Therefore, to reduce the computational effort and improve the computation speed, the present study conducts all the flow simulations at a resolution of 200 nodes/mm, or a cell size of 5 µm.

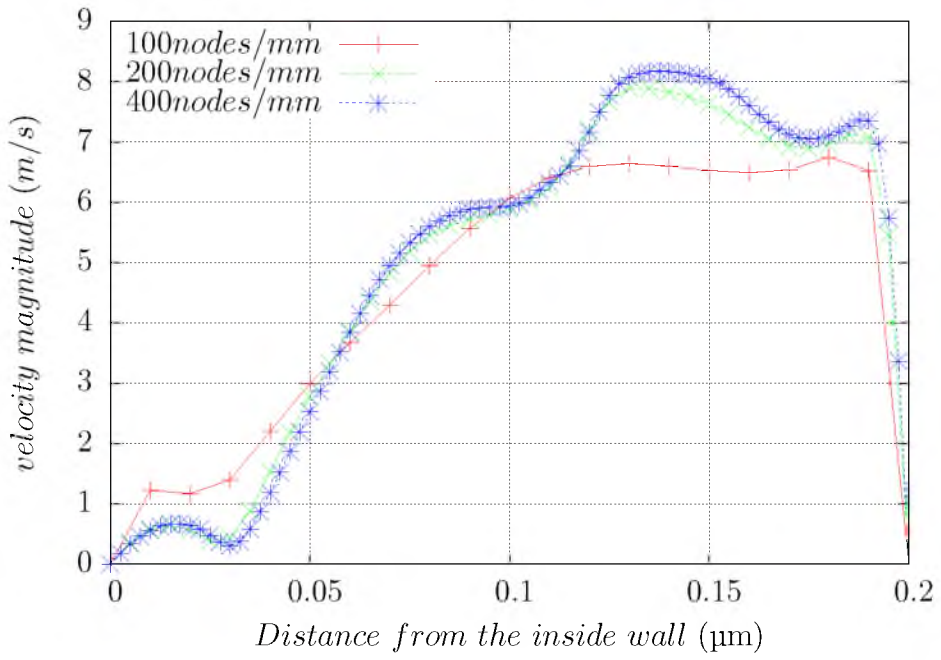

Figure 3.7: **Velocity magnitude with mesh resolution:** The velocity magnitude along the extraction line in the recirculation zone (see Fig. (3.8)) for different mesh resolutions.

The global order of accuracy $p = 1.85$ for the present configuration of the simulations, calculated as

$$p = \frac{\log_e\left(\frac{f_3 - f_2}{f_2 - f_1}\right)}{\log_e(r)}, \tag{3.10}$$

where f_x are the pressure drops, as shown in Table (3.3), and r is the ratio of the cell sizes h_x for two subsequent resolutions and is given by

$$r = \frac{h_2}{h_1} = 2. \tag{3.11}$$

Further, the error estimator E [67], which gives the error band for the simulation results at the resolution of 200 nodes/mm, is 0.99%. E is calculated as

$$E = \frac{\epsilon r^p}{r^p - 1}, \tag{3.12}$$

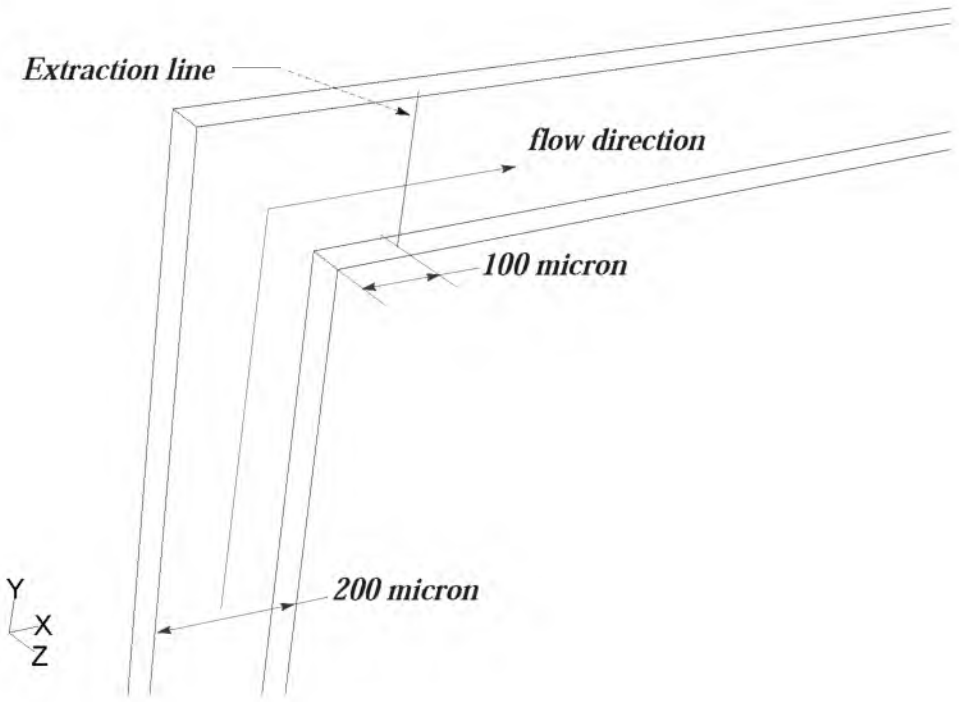

Figure 3.8: **Velocity magnitude for grid independence:** Image shows the line in the outlet channel, at a distance of 100 µm from the bend, at which the velocity magnitude is extracted.

and

$$\epsilon = \frac{f_2 - f_1}{f_1}, \tag{3.13}$$

where f_x values are given in Table (3.3). When E is multiplied by a factor of safety $F_s = 3.0$ as shown

$$GCI_{f_2} = F_s E = F_s \frac{\epsilon r^p}{r^p - 1}, \tag{3.14}$$

the result is the grid convergence index (GCI) for the coarse grid with a cell size of 5 µm. The GCI relates the present grid independence study to a generalized grid dependence study performed by doubling the grid size while using a second-order discretization scheme [67]. It also provides a very conservative method for reporting the error band of the results of a CFD simulation. The GCI for the present set of simulations is 2.98%.

3.3.3 Solution convergence

Theoretically, in any simulation, the governing equations need to be solved iteratively until the residuals are reduced to zero. However, in many cases, the solution remains unchanged after a certain cut-off value of the residuals. It is typically sufficient to run a simulation until this cut-off residual is reached to obtain accurate results and eventually save computational resources. Therefore, a systematic solution convergence study is necessary to get an estimate of these cut-off residual values. As shown in Fig. (3.1), the continuity and velocity component residuals can be monitored to check the convergence of the flow simulations. As the continuity residual is the largest of the four residuals, it acts as the limiting criteria for the solution convergence. The continuity residual R^c is calculated as [56]

$$R^c = \sum_{cells\ P} |\text{rate of mass creation in cell P}|. \tag{3.15}$$

Fluent has an option to scale the residuals so that all the residuals are of $\mathcal{O}(1)$. Scaled residuals R_s^c are calculated as

$$R_s^c = \frac{R_N^c}{R_5^c}, \tag{3.16}$$

where R_5^c is the residual after the first five iterations while R_N^c is the residual after N iterations. The present work uses the scaled residual for continuity to monitor the convergence of all the simulations.

Using the flow simulation from the previous section for the microchannel with the cell size of 5 µm, the pressure drop across the microchannel is evaluated for three values of the scaled continuity residual, as shown in Table (3.4). The values of residuals are chosen such that they are of $\mathcal{O}(1)$, $\mathcal{O}(-1)$, and $\mathcal{O}(-2)$ times the theoretical mass flow rate of 3.6645 x 10^5 kg s^{-1} for $Re = 200$. The change in the pressure drop as the continuity residual is reduced is almost zero. Further, the velocity magnitudes, extracted along the same line as discussed earlier, are shown in Fig. (3.9) for the said residual values. Although the pressure drop and the velocity magnitude remain constant after $R_s^c = 10^{-5}$, the convergence criteria is set to $R_s^c = 10^{-7}$ so that R_s^c is less than 1% of the theoretical mass flow rate.

3.4 Summary

The mass and momentum conservation equations of the Navier-Stokes equations are used to simulate the water flow in the microchannels containing a 90° miter bend. The viscosity and density of the water (at $T_{avg} = 22.5°C$) are the only properties required for the simulation, as the flow is assumed to be laminar ($Re \leq 600$), incompressible (ρ = constant), isothermal (T_{avg} = constant), and at steady state. A hydrodynamically fully-developed velocity profile, calculated by using the infinite summation analytical solution proposed by Spiga and Morini [65], is used at the inlet while atmospheric pressure is assumed at the outlet and the no-slip condition is

Table 3.4: Solution convergence analysis (Pressure drop): Change in pressure drop across the microchannel with continuity residual.

Continuity residual (R_s^c)	Pressure (Pa)
$1e^{-5}$	102716.24
$1e^{-6}$	102716.27
$1e^{-7}$	102716.28

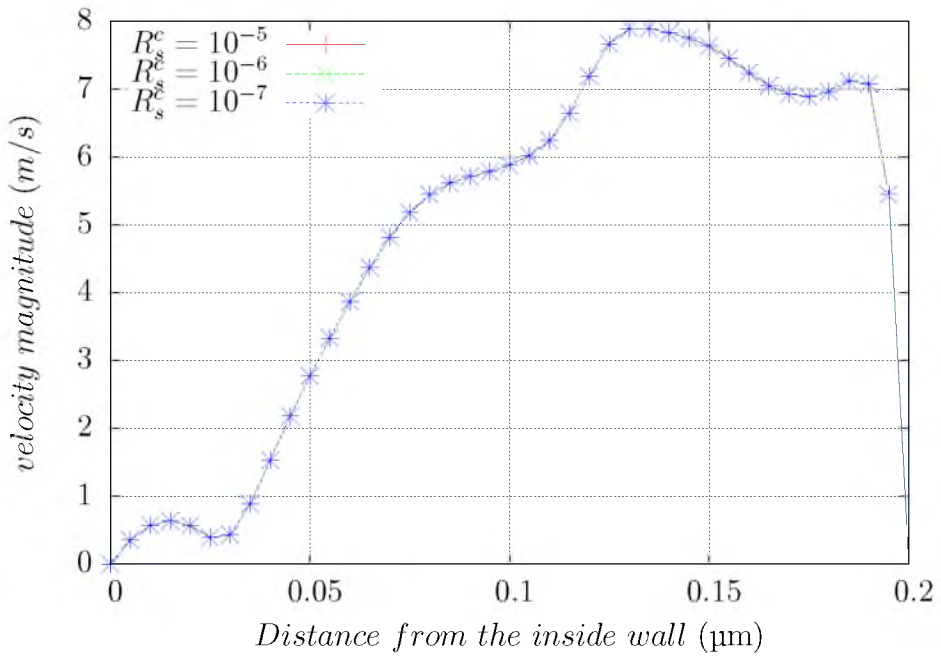

Figure 3.9: **Solution convergence analysis:** The image shows the velocity profile along the extraction line shown in Fig. (3.8) at three cut-off values for the continuity residual in the flow simulation.

applied on all walls. A plane of symmetry is present in the flow parallel to the width of the inlet along the center of the channel, which reduces the simulation domain by a factor of two.

A uniform structured grid is used throughout the domain to capture the downstream effects of the bend accurately and a boundary layer is attached to all the walls (except the symmetry plane) to smooth the gradients at the wall and improve the accuracy of the simulation. The third-order MUSCL scheme is used to discretize the momentum equation due to its accuracy for reasonably large cell sizes. The PRESTO scheme is used to discretize the pressure as it has a better performance in cases of vortex flow, even though it is only first-order accurate. A fully-coupled implicit algorithm, with a multigrid method, is used because of its better convergence rate than the SIMPLE algorithm.

A test simulation, using a straight microchannel with the above-mentioned configuration, is performed to verify the hydrodynamically fully-developed velocity profile used for the inlet boundary condition. The outlet velocity from the simulation is

within 2.5% of the calculated velocity profile. A systematic grid independence study is performed to evaluate the optimal cell size for the simulations. The pressure drop across the channels for three cell sizes of 10 µm, 5 µm, and 2.5 µm is analyzed, in addition to the mass flow rates and velocity magnitudes. The simulation results for a cell size of 5 µm are optimal based on computation time and solution accuracy. The pressure drop for the test case is found to be within 0.92% of the asymptotic value and the error estimate is $E = 0.99\%$. A solution convergence test reveals that the scaled continuity residual of $R_s^c = 10^{-5}$ is sufficient to ensure the solution convergence.

The dimensions of the microchannels used in the simulations, the data for the flow development length in the outlet channel, the size of recirculation zones at the miter bend, and the bend excess loss coefficients are presented in the next chapter.

CHAPTER 4

RESULTS AND DISCUSSION

A numerical simulation of water flow in microchannels with miter bends, featuring varying area ratios, is conducted using Fluent and Gambit. The details of the channel dimensions and the results of the simulations, such as the flow structure changes with Reynolds number, aspect ratio and area ratio of the channels, the flow development lengths, and the pressure excess loss coefficients, are presented in this chapter.

4.1 Simulation cases

A comprehensive set of nine microchannels with an inlet length of 3 mm and outlet length ranging from 15 mm to 25 mm is used to study the flow characteristics of miter bend microchannels. The height of these channels is kept constant at 100 µm, simulating the thickness of double-sided adhesive tape that defines the channel pattern using xurography, while the widths vary from 100 µm to 500 µm, as presented in Table (4.1). The hydraulic diameters of these channels range from 100 µm to 167 µm.

In addition to these miter bend microchannels, a set of seven microchannels with abrupt expansions and contractions at the miter bends is also studied. The dimensions of these channels are shown in Table (4.2) and Table (4.3), respectively. The area ratios of these channels range from a low 10% to a maximum of 300%, thereby enabling data for a complete range of area ratios to be collected. The data reduction procedure and the results from the above set of simulations are presented in the following sections, along with a comparison of the relevant results from the literature.

4.2 Flow structure

A flow structure analysis for water flows through a miter bend for different Reynolds numbers, in a microchannel with $\alpha = 0.33$, is conducted using the streamlines and

Table 4.1: **Dimensions of miter bend microchannels:** The table lists the dimensions of the microchannels, with aspect ratio $0.2 \leq \alpha \leq 1.0$.

Width (µm)	Height (µm)	Aspect ratio (α)	Channel Length (mm)	
Inlet			Inlet	Outlet
100	100	1.00	3	15
150	100	0.67	3	15
200	100	0.50	3	20
250	100	0.40	3	20
300	100	0.33	3	25
350	100	0.28	3	25
400	100	0.25	3	25
450	100	0.22	3	25
500	100	0.20	3	25

Table 4.2: **Dimensions of miter bend expansion microchannels:** The table lists the dimensions of the miter bent expansion microchannels, with area ratios $1.10 \leq A_r \leq 3.0$.

Width (µm)		Height (µm)	Area ratio (A_r)	Channel Length (mm)	
Inlet	Outlet			Inlet	Outlet
300	330	100	1.10	3	15
300	360	100	1.20	3	15
300	390	100	1.30	3	15
300	450	100	1.50	3	15
300	600	100	2.00	3	15
300	750	100	2.50	3	15
300	900	100	3.00	3	15

Table 4.3: **Dimensions of miter bend contraction microchannels:** The table lists the dimensions of the miter bent contraction microchannels, with area ratio $0.33 \leq A_r \leq 0.91$.

Width (µm)		Height (µm)	Area ratio (A_r)	Channel Length (mm)	
Inlet	Outlet			Inlet	Outlet
330	300	100	0.91	5	20
360	300	100	0.84	5	20
390	300	100	0.77	5	20
450	300	100	0.66	5	20
600	300	100	0.50	5	20
750	300	100	0.40	5	25
900	300	100	0.33	5	27

velocity magnitude distribution, as shown in Fig. (4.1) to Fig. (4.6). The figures show the velocity magnitude and streamlines for the flow at Reynolds numbers Re ={25, 75, 150, 300, 400, 600}. The velocity magnitude field is shown in the planes orthogonal to the channel at distances of 0, 50, 100, 150, 200, 250, 400, 500, 600, 700, 850, and 1000 µm from the bend upstream into the inlet channel. In the outlet channel, the planes are located at distances of 0, 100, 200, 300,400, 500, 600, 700, 950, 1200, 1450, 1700, 2200, and 2700 µm from the bend. In the miter bend region, three planes are shown which are oriented at angles of 102.5°, 135°, and 157.5° with respect to the positive X-axis.

From Fig. (4.1) and Fig. (4.2), it is evident that streamlines are detached from the outer walls as early as $Re = 25$, forming an outer recirculation zone, as shown by the streamlines in Fig. (4.1b) and the dark blue area of velocity magnitude in the angular planes in Fig. (4.1a). The flow separation on the inner wall is evident in Fig. (4.2a), as a dark blue area in the velocity magnitude plane in the outlet channel and as a minor distortion of the streamlines in Fig. (4.2b). From this observation, it can be deduced that the flow separation on the outer wall takes place as early as $Re = 25$ and for the inner wall in the range of $25 < Re < 75$, which is consistent with the experimental results reported by Xiong and Chung [43].

As the Reynolds number is increased, both the primary and secondary recirculation zones increased in the length and width up to $Re = 300$, after which the outer (secondary) recirculation zone's length into the outlet channel decreases while its depth into the inlet channel increases. On the other hand, the primary recirculation zone remained constant in size while the magnitude of the reversed flow increases with increasing Reynolds number. In addition to the size changes, as the Reynolds number increases beyond $Re = 400$, an axial vortex is developed in the outlet channel, as shown by the streamlines in Fig. (4.5b), which grows in magnitude with the increasing Reynolds number (see also Fig. (4.6b)). A further increase in the Reynolds number beyond $Re = 600$ results in convergence issues, where a flow transition is assumed. The Reynolds number Re_{cr}, after which the solution could not converge, was observed to change with α. Dreher et al. [52] reported that the simulation could not converge for $Re > 500$ while simulating the flow in a square microchannel with 90° miter bend

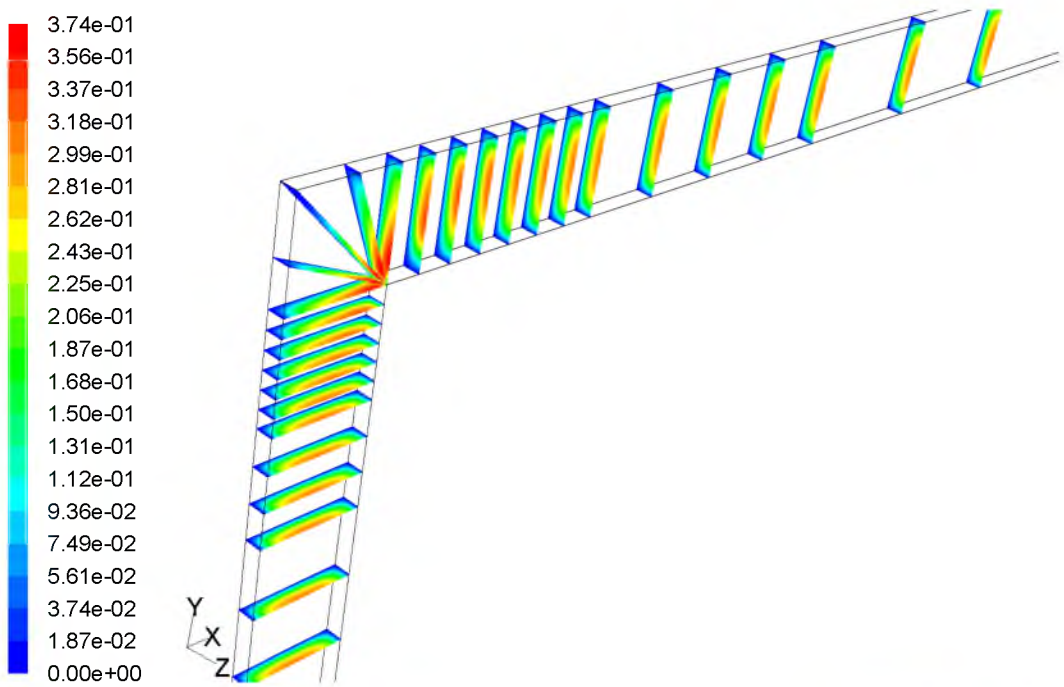

(a) Velocity magnitudes for $Re = 25$

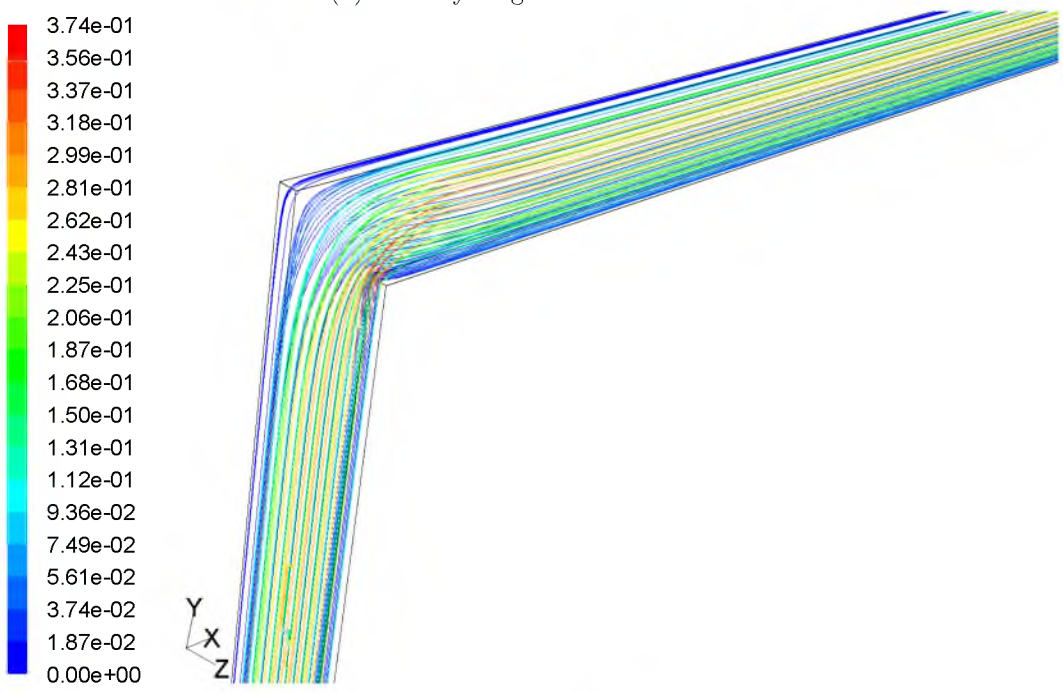

(b) Streamlines for $Re = 25$

Figure 4.1: **Contours of velocity magnitudes and streamlines** *I*: The figure shows the contours of the velocity magnitude at various planes along the microchannel and the streamlines for $Re = 25$.

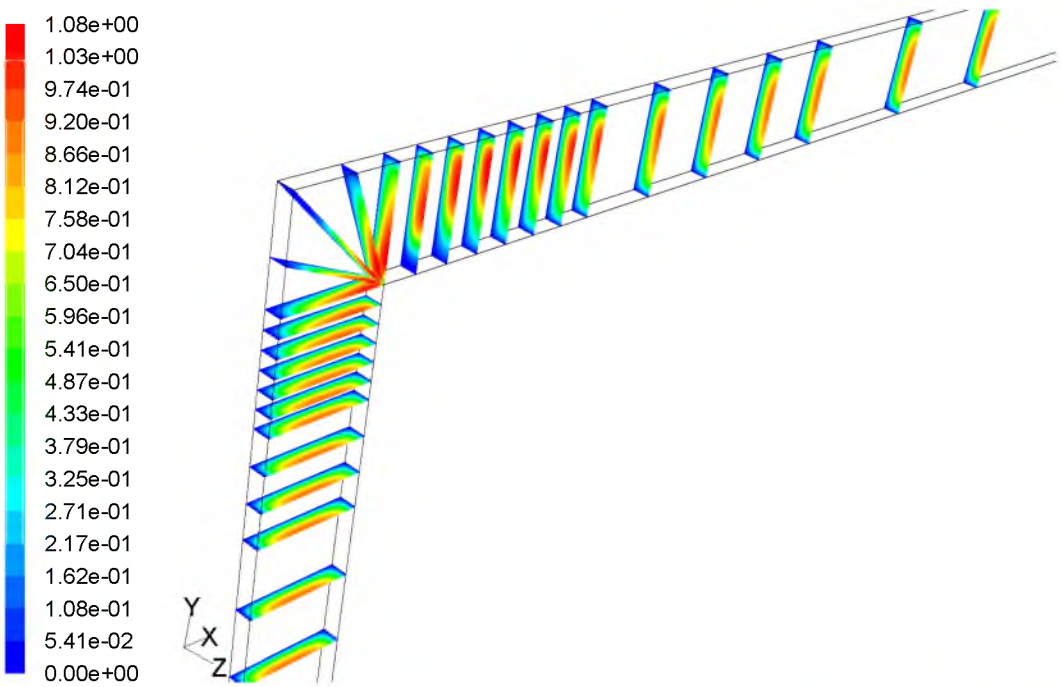

(a) Velocity magnitudes for $Re = 75$

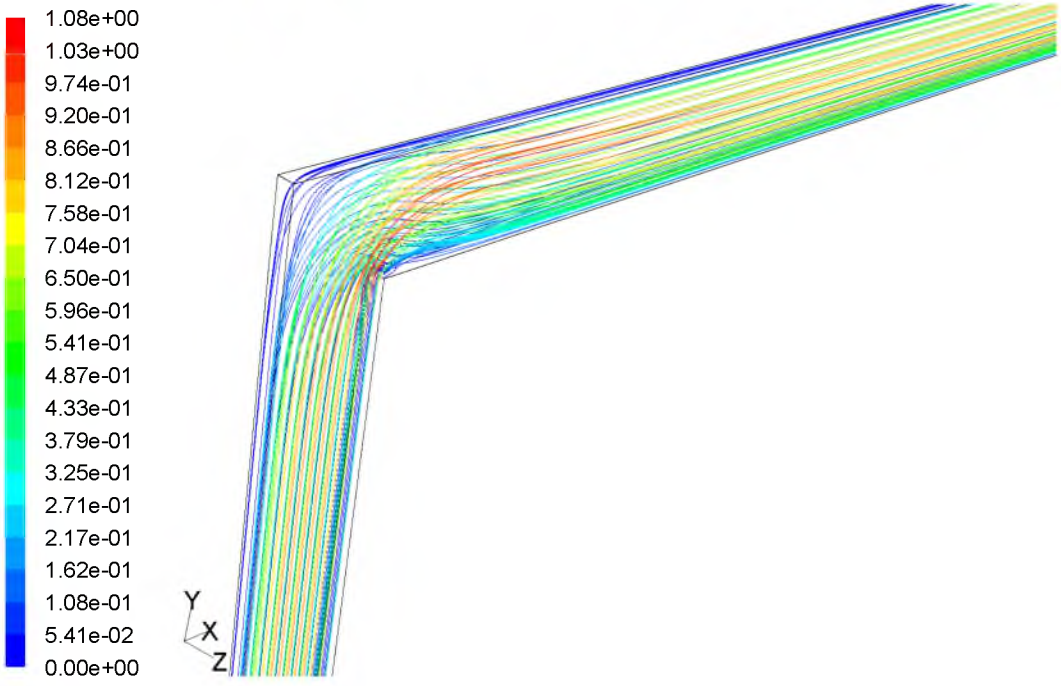

(b) Streamlines for $Re = 75$

Figure 4.2: **Contours of velocity magnitudes and streamlines *II*:** The figure shows the contours of the velocity magnitude at various planes along the microchannel and the streamlines for $Re = 75$.

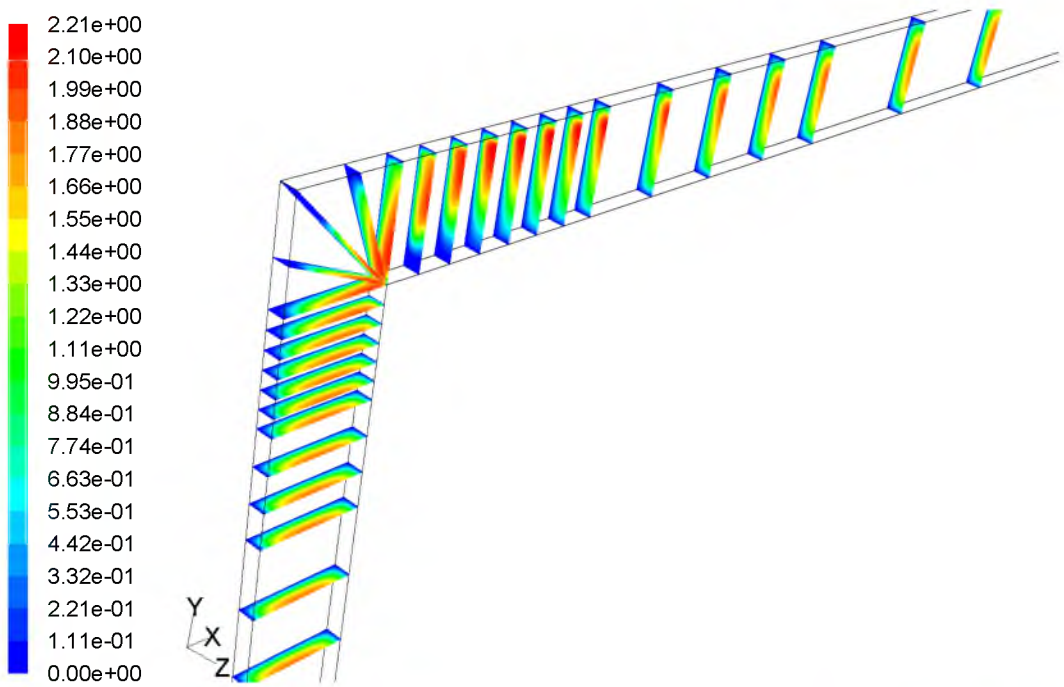

(a) Velocity magnitudes for $Re = 150$

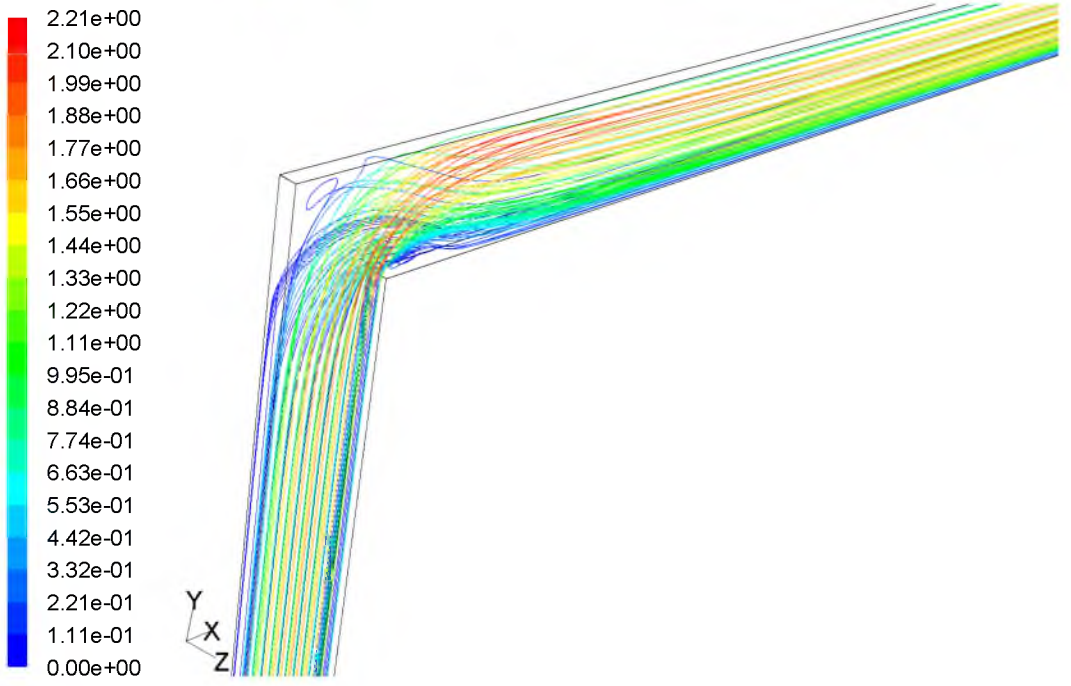

(b) Streamlines for $Re = 150$

Figure 4.3: **Contours of velocity magnitudes and streamlines *III*:** The figure shows the contours of the velocity magnitude at various planes along the microchannel and the streamlines for $Re = 150$.

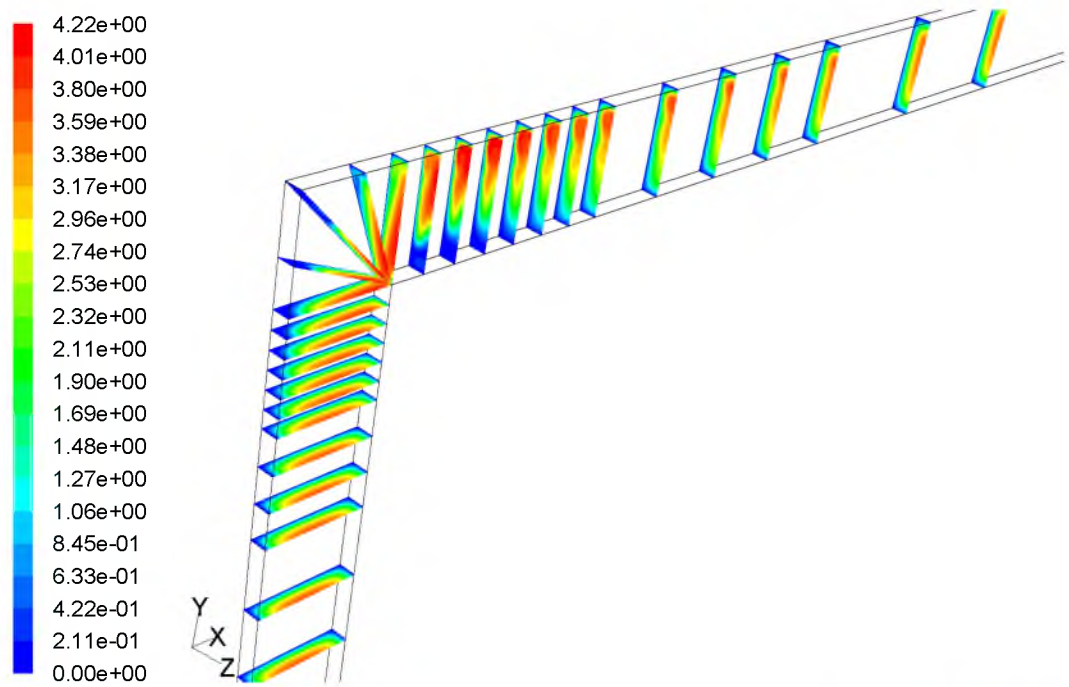

(a) Velocity magnitudes for $Re = 300$

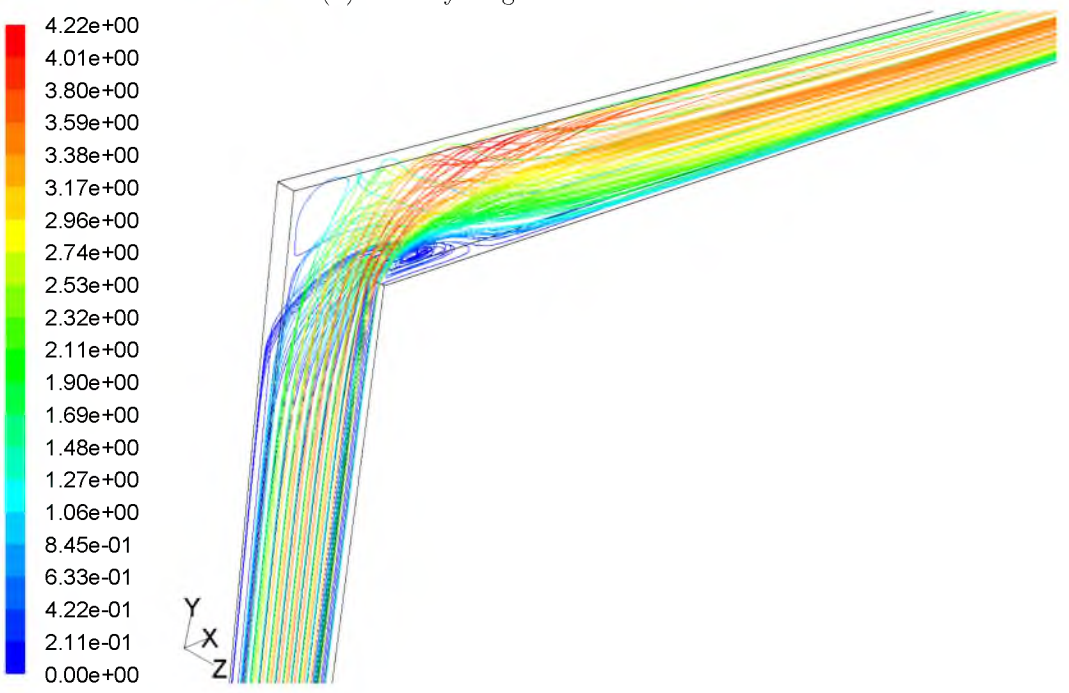

(b) Streamlines for $Re = 300$

Figure 4.4: **Contours of velocity magnitudes and streamlines** *IV*: The figure shows the contours of the velocity magnitude at various planes along the microchannel and the streamlines for $Re = 300$.

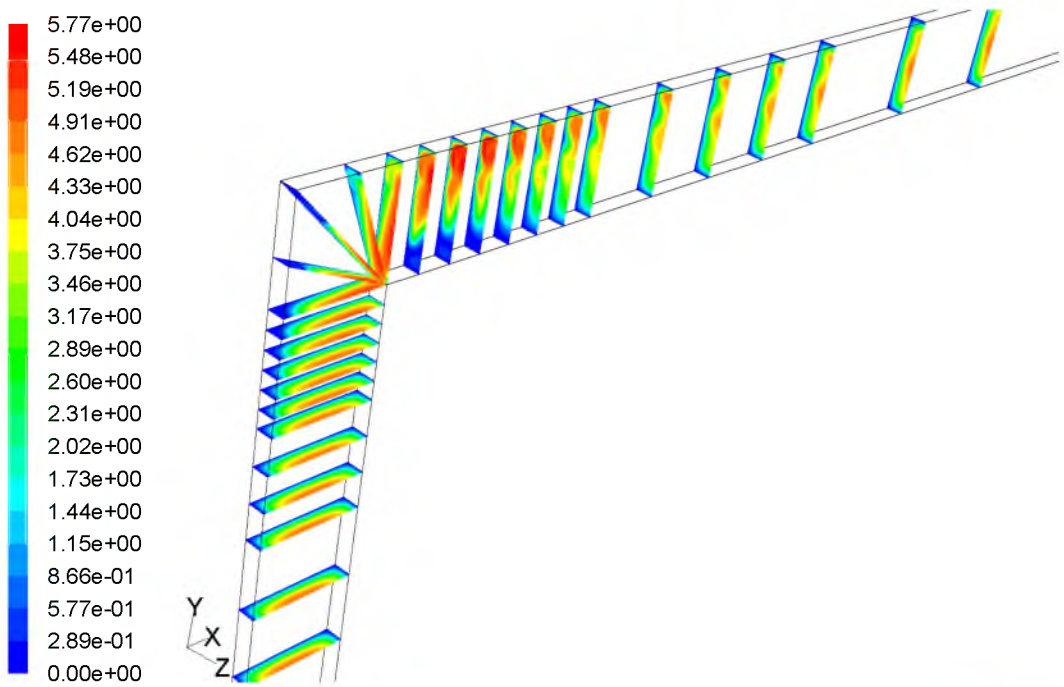

(a) Velocity magnitudes for $Re = 400$

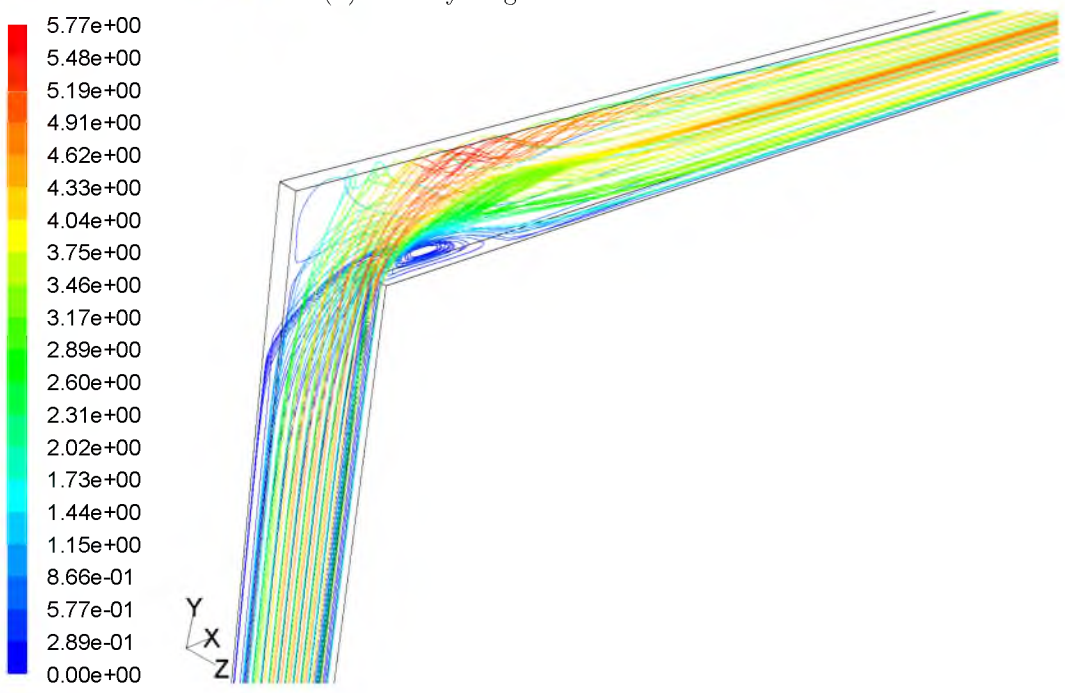

(b) Streamlines for $Re = 400$

Figure 4.5: **Contours of velocity magnitudes and streamlines V:** The figure shows the contours of the velocity magnitude at various planes along the microchannel and the streamlines for $Re = 400$.

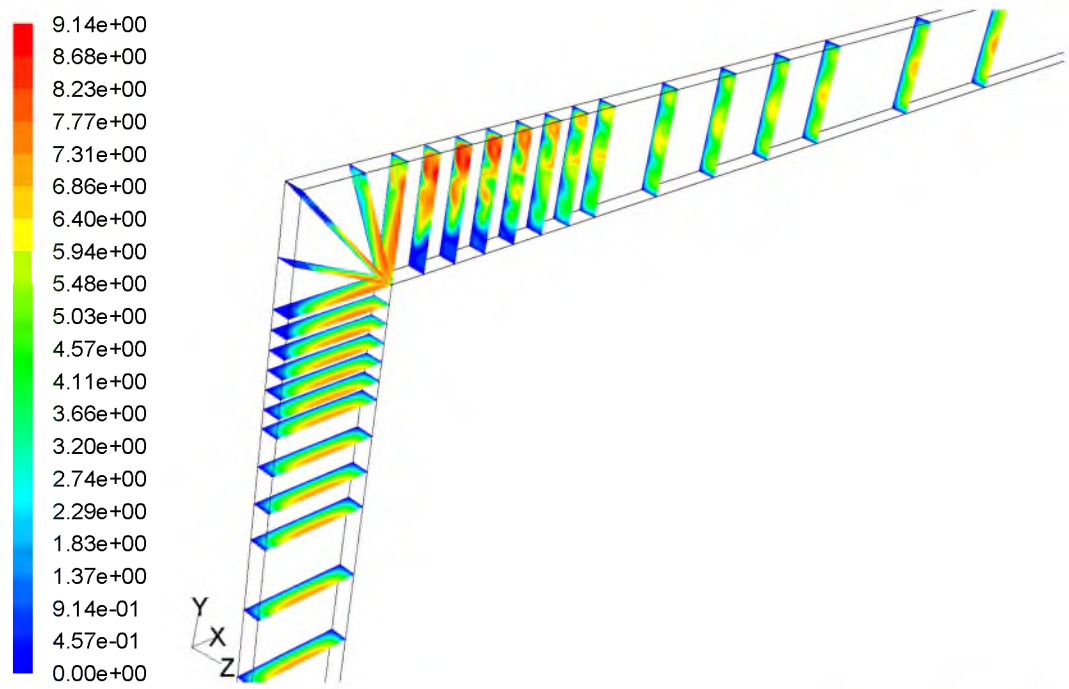

(a) Velocity magnitudes for $Re = 600$

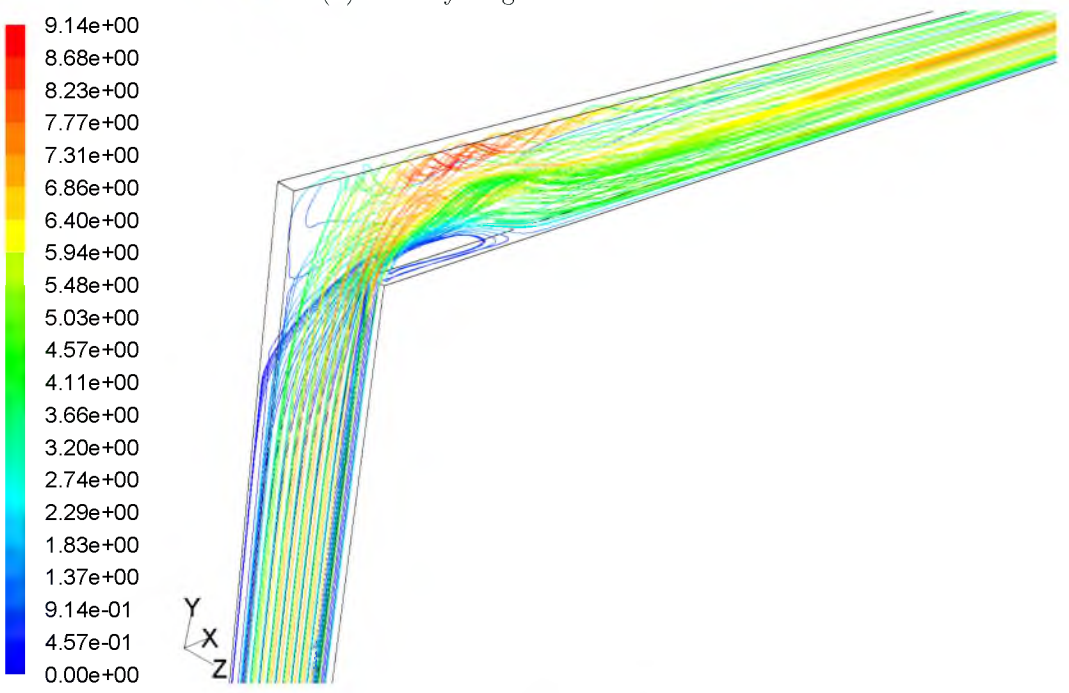

(b) Streamlines for $Re = 600$

Figure 4.6: **Contours of velocity magnitudes and streamlines** VI**:** The figure shows the contours of the velocity magnitude at various planes along the microchannel and the streamlines for $Re = 600$.

and $D_h = 200\,\mu m$.

Fig. (4.5b) shows that a complete axial vortex has developed in the outlet channel when $Re = 400$. The effects of abrupt expansions on this flow vortex can be observed in Fig. (4.7) to Fig. (4.12) where the area ratio at the miter bend is in the range of $3.0 \leq A_r \leq 1.2$ for an inlet flow Reynolds number of $Re = 400$. Due to abrupt expansions in the channel, the flow is significantly decelerated, resulting in larger flow separation distances. The width and length of the primary recirculation zones decrease with the area ratio at the miter bend. Since the flow is decelerated, the axial vortex has not formed yet for $Re = 400$ at the higher area ratio channels, but a closer look into Fig. (4.9a) and Fig. (4.9b) shows a very small axial vortex that develops in strength as the area ratio is further reduced, which is shown in Fig. (4.11) and Fig. (4.12).

A comparison of flow structure in microchannels with minor expansion and contraction to that of a normal channel is shown in Fig. (4.13), Fig. (4.14), and Fig. (4.15). Minimal change in the flow structure is noted as A_r is reduced from 1.1 to 0.91. The only discernible change is the increase in velocity magnitude of the primary recirculation zones and the strength of the axial flow vortex when the flow accelerates in the contracting channel. Further reduction in the area ratio results in the flow acceleration increasing the velocity magnitude of the primary recirculation zone along with the strength of the axial vortex, as observed in the velocity magnitude scales shown in Fig. (4.15) to Fig. (4.21). Another interesting observation made from these figures is that the size of the primary recirculation zone is almost the same, while the size of the secondary recirculation zone is increasing with decreasing area ratio.

4.3 Recirculation zones

The flow separation and the size of the recirculation zones are the important aspects in the microchannel flows with bends. Fig. (4.22) shows the dimensions of the recirculation zones and their respective measurement references. L_{rp} is the length of the primary recirculation zone and w_{rp} is its width, while L_{rso} and L_{rsi} are the length and depth of the secondary recirculation zone, respectively.

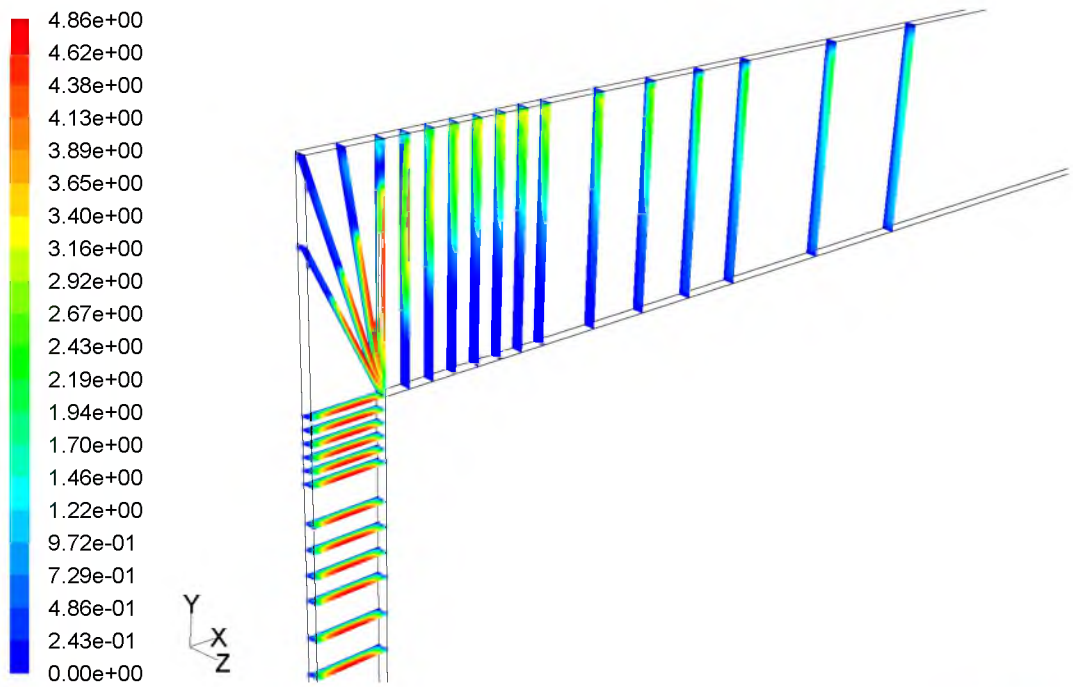

(a) Velocity magnitudes for $A_r = 3.0$

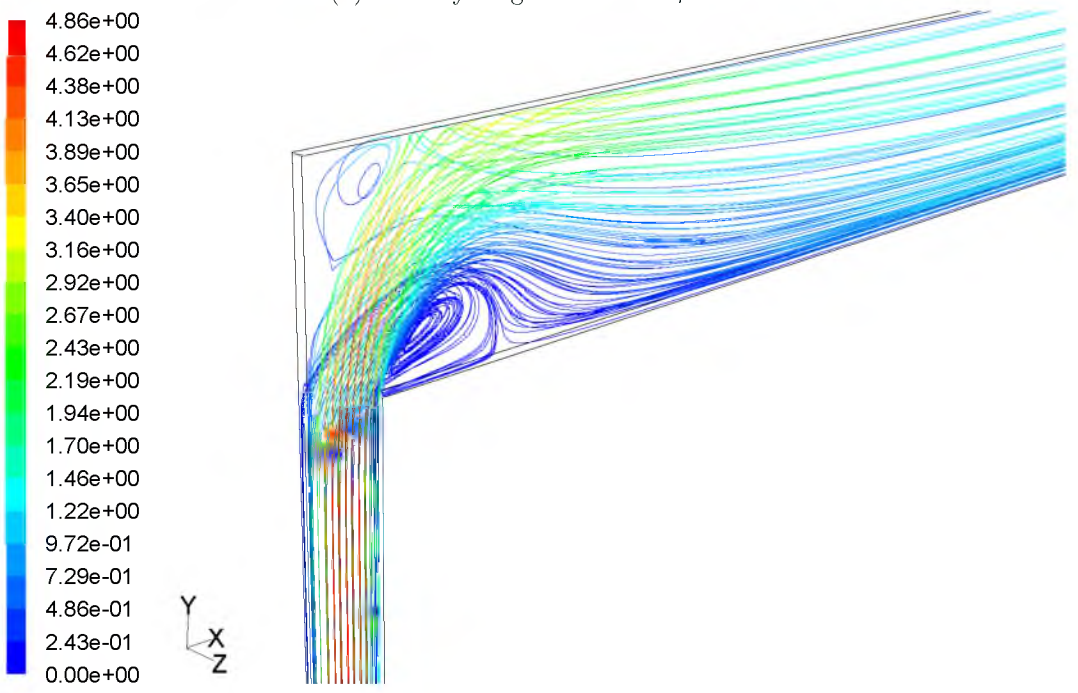

(b) Streamlines for $A_r = 3.0$

Figure 4.7: **Contours of velocity magnitudes and streamlines** *VII*: The figure shows the contours of the velocity magnitude at various planes along the microchannel and the streamlines for $A_r = 3.0$ and $Re = 400$.

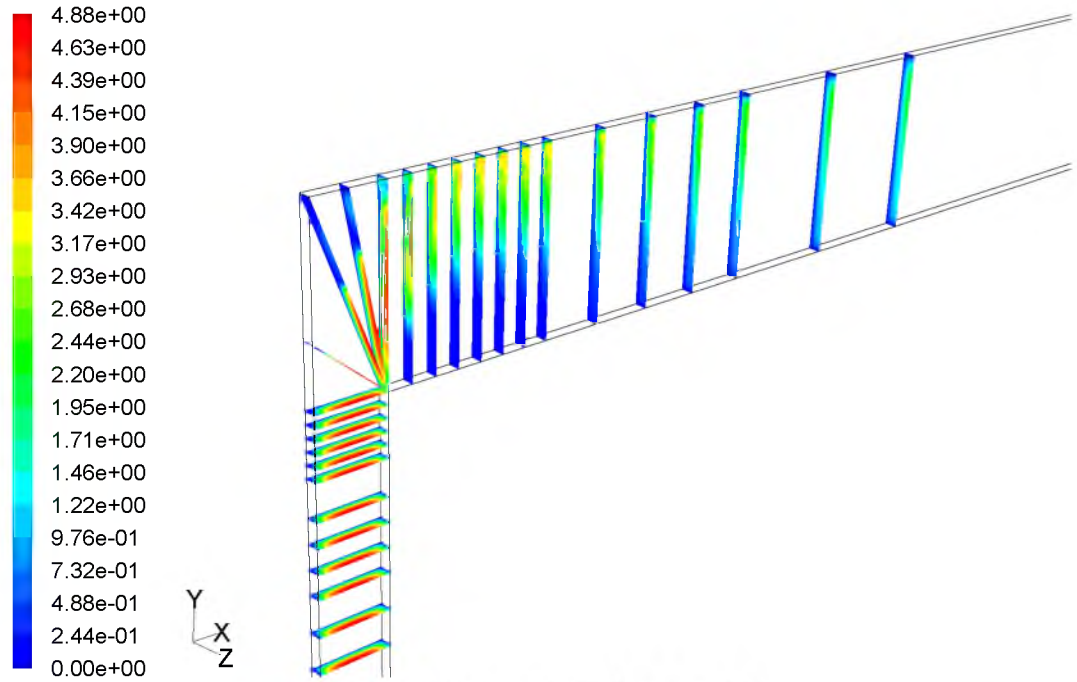

(a) Velocity magnitudes for $A_r = 2.5$

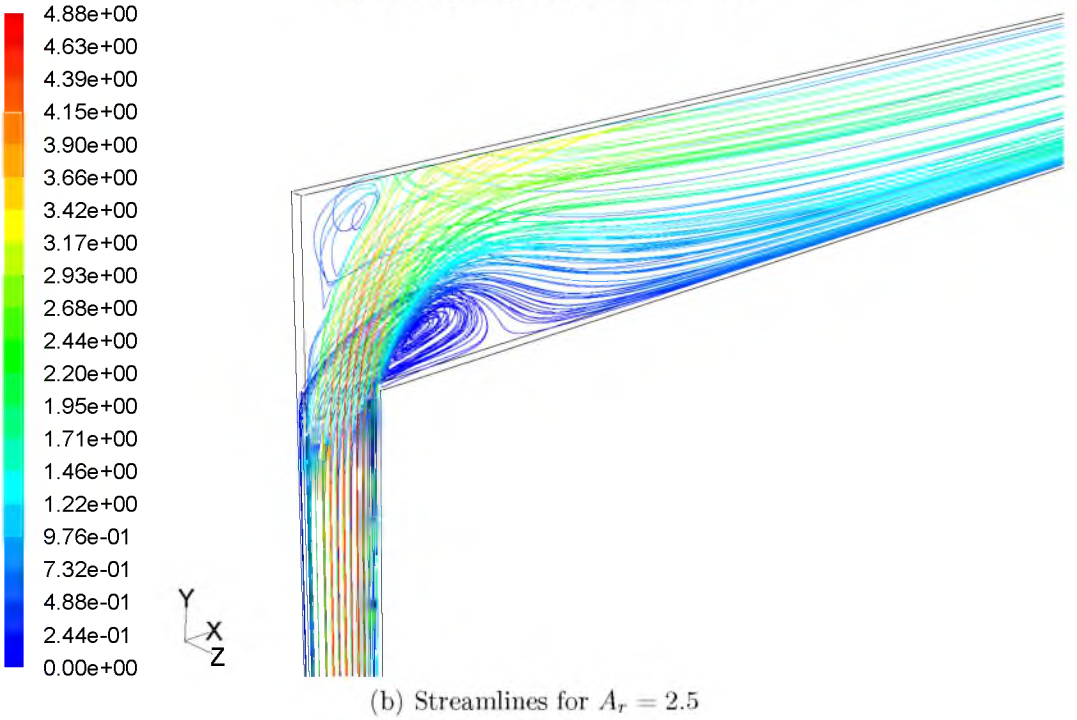

(b) Streamlines for $A_r = 2.5$

Figure 4.8: **Contours of velocity magnitudes and streamlines** *VIII*: The figure shows the contours of the velocity magnitude at various planes along the microchannel and the streamlines for $A_r = 2.5$ and $Re = 400$.

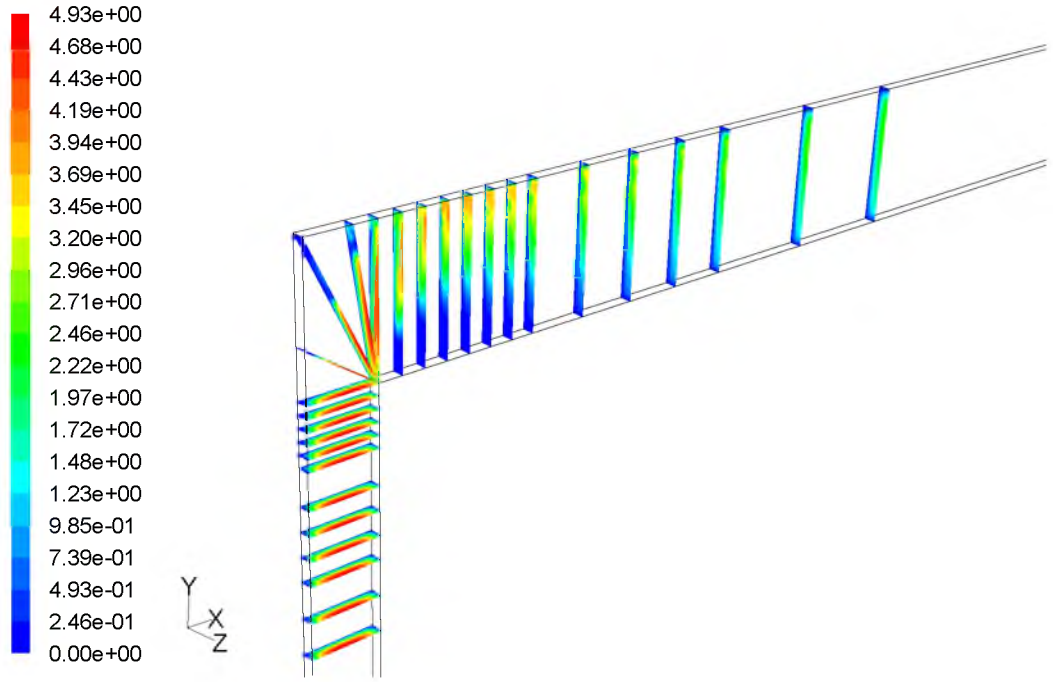

(a) Velocity magnitudes for $A_r = 2.0$

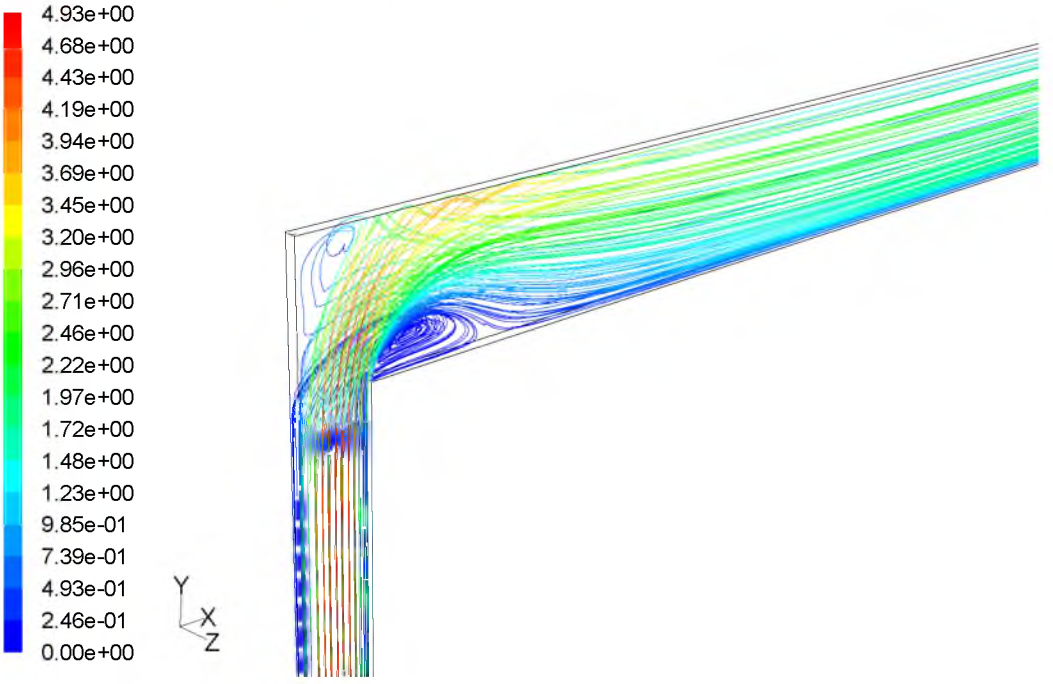

(b) Streamlines for $A_r = 2.0$

Figure 4.9: **Contours of velocity magnitudes and streamlines** IX**:** The figure shows the contours of the velocity magnitude at various planes along the microchannel and the streamlines for $A_r = 2.0$ and $Re = 400$.

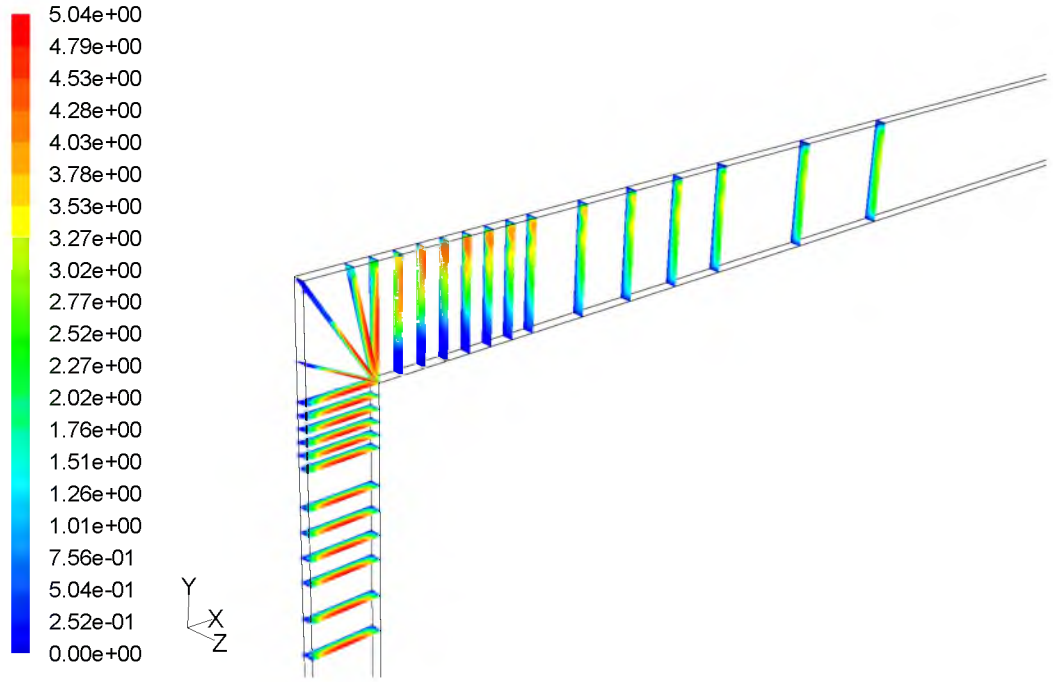

(a) Velocity magnitudes for $A_r = 1.5$

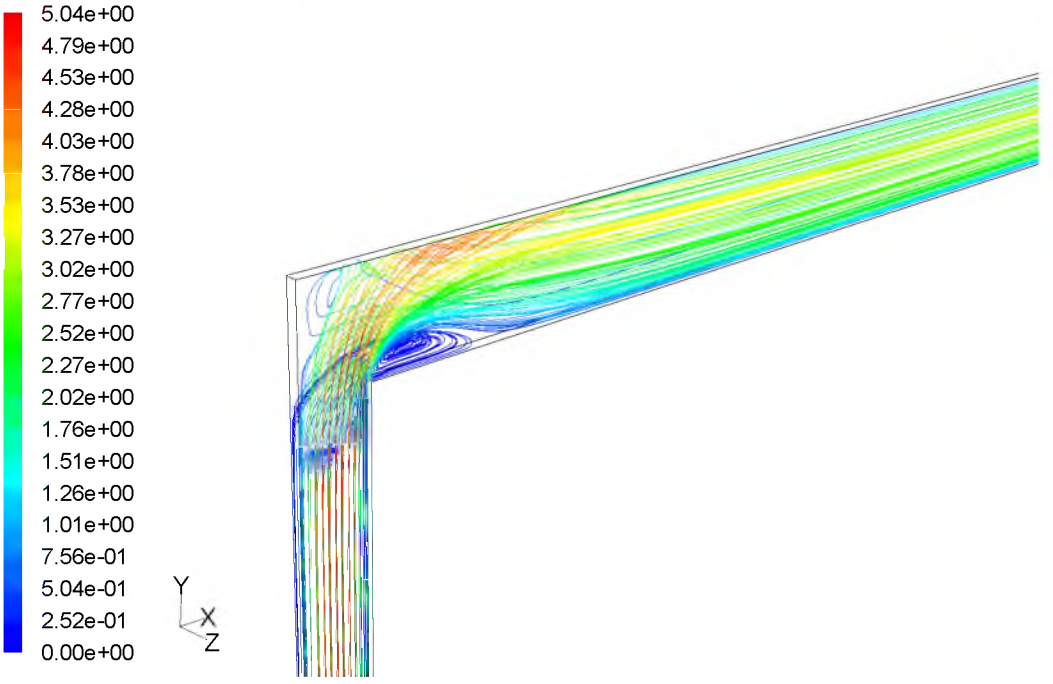

(b) Streamlines for $A_r = 1.5$

Figure 4.10: **Contours of velocity magnitudes and streamlines** X**:** The figure shows the contours of the velocity magnitude at various planes along the microchannel and the streamlines for $A_r = 1.5$ and $Re = 400$.

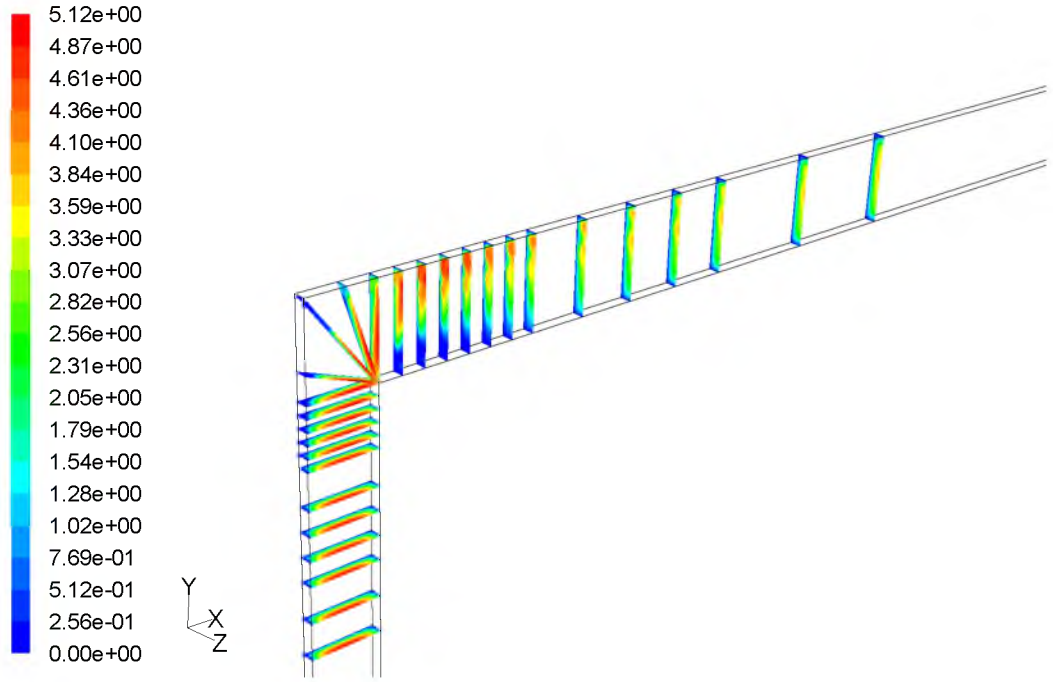

(a) Velocity magnitudes for $A_r = 1.3$

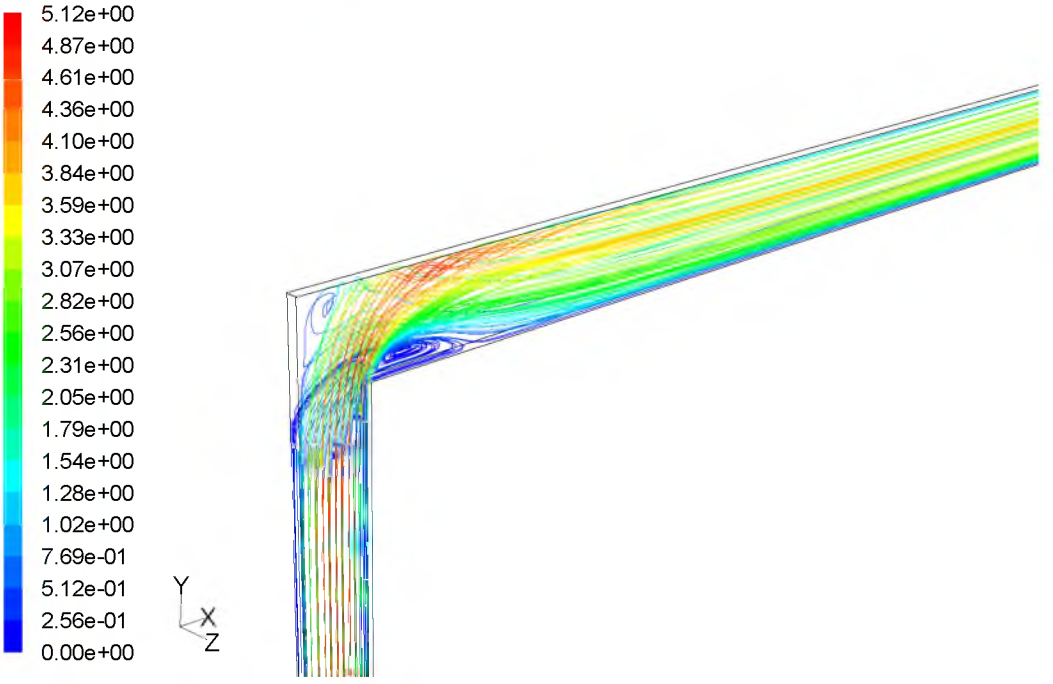

(b) Streamlines for $A_r = 1.3$

Figure 4.11: **Contours of velocity magnitudes and streamlines** XI**:** The figure shows the contours of the velocity magnitude at various planes along the microchannel and the streamlines for $A_r = 1.3$ and $Re = 400$.

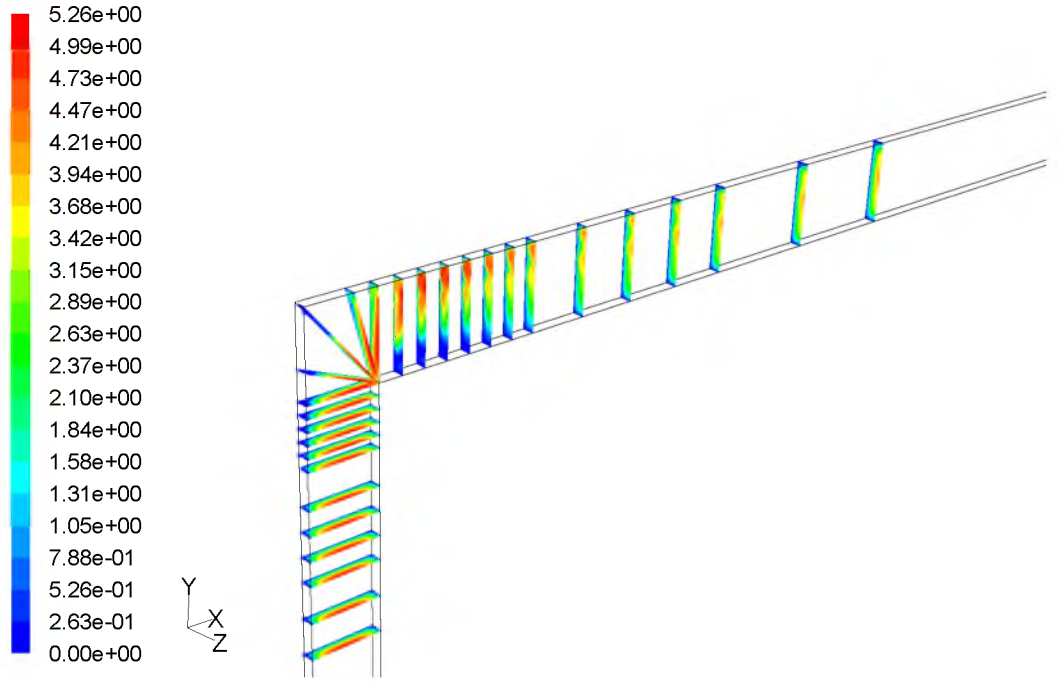

(a) Velocity magnitudes for $A_r = 1.2$

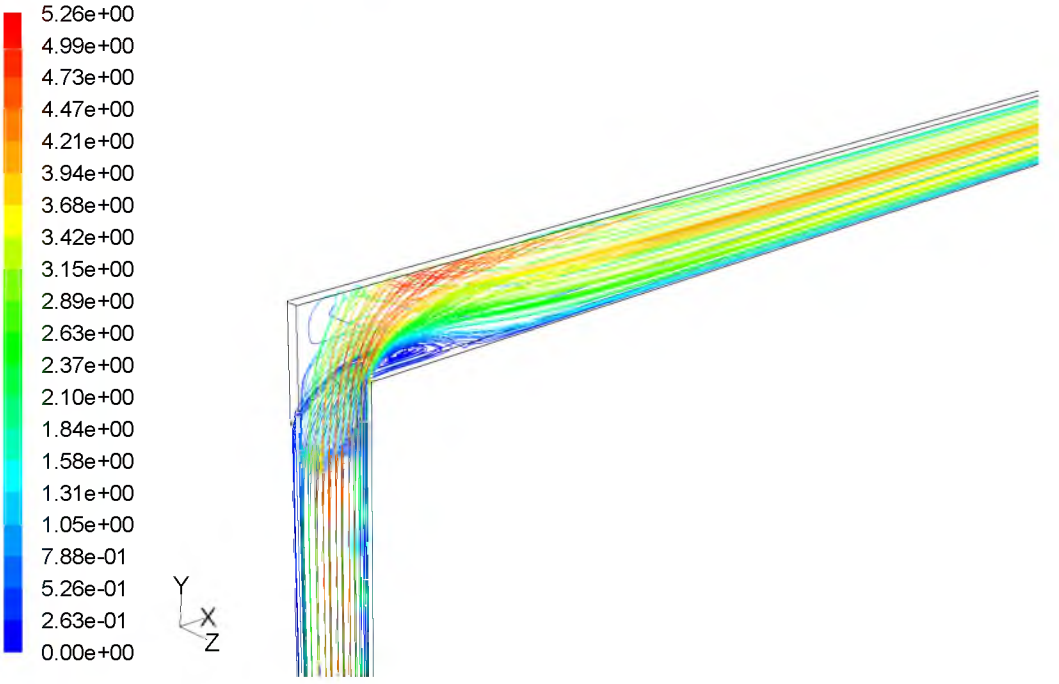

(b) Streamlines for $A_r = 1.2$

Figure 4.12: **Contours of velocity magnitudes and streamlines** *XII*: The figure shows the contours of the velocity magnitude at various planes along the microchannel and the streamlines for $A_r = 1.2$ and $Re = 400$.

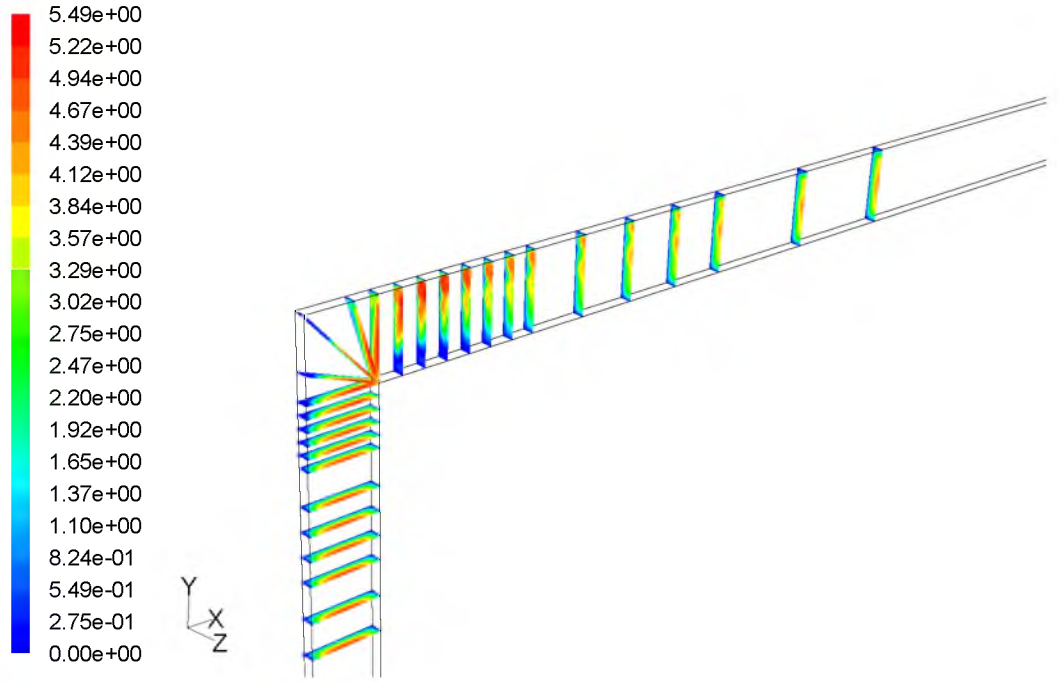

(a) Velocity magnitudes for $A_r = 1.1$

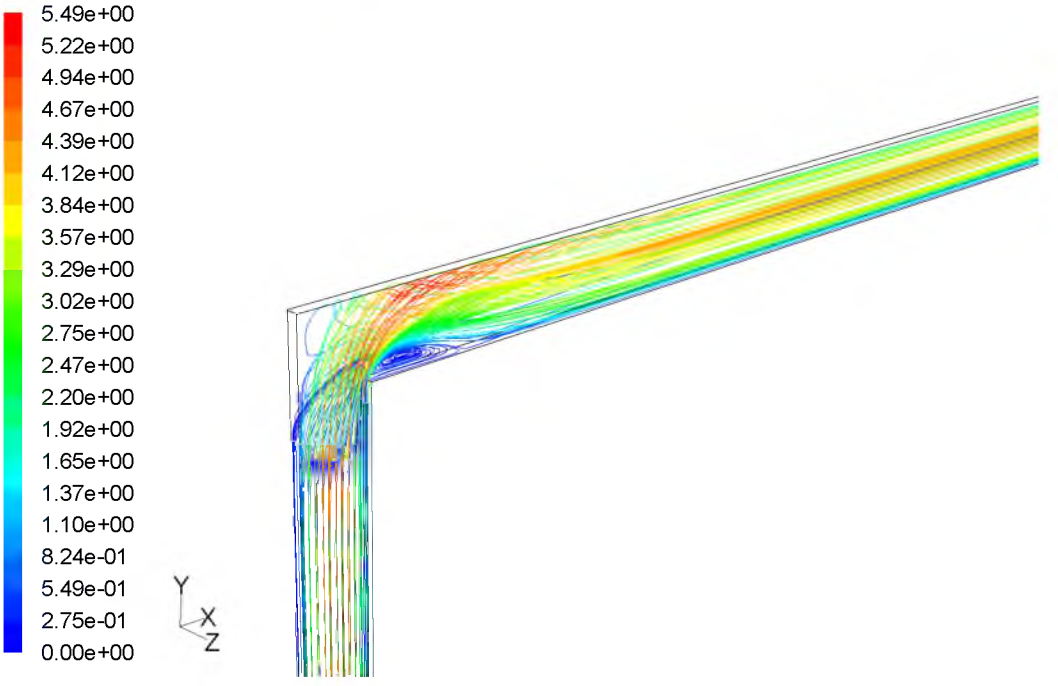

(b) Streamlines for $A_r = 1.1$

Figure 4.13: **Contours of velocity magnitudes and streamlines** $XIII$**:** The figure shows the contours of the velocity magnitude at various planes along the microchannel and the streamlines for $A_r = 1.1$ and $Re = 400$.

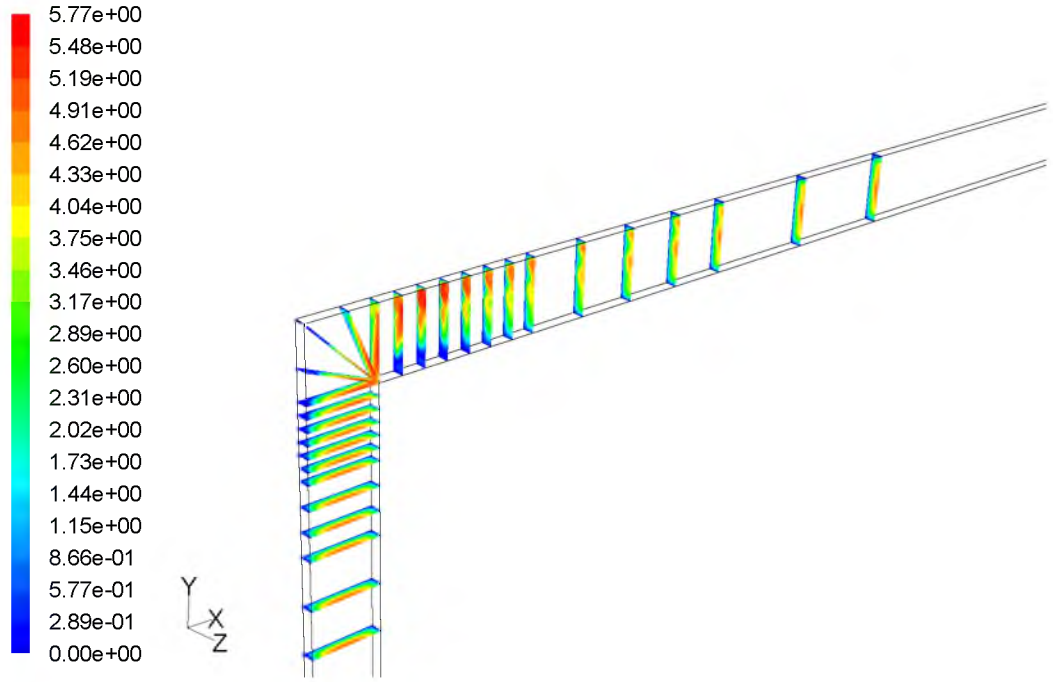

(a) Velocity magnitudes for $A_r = 1.0$

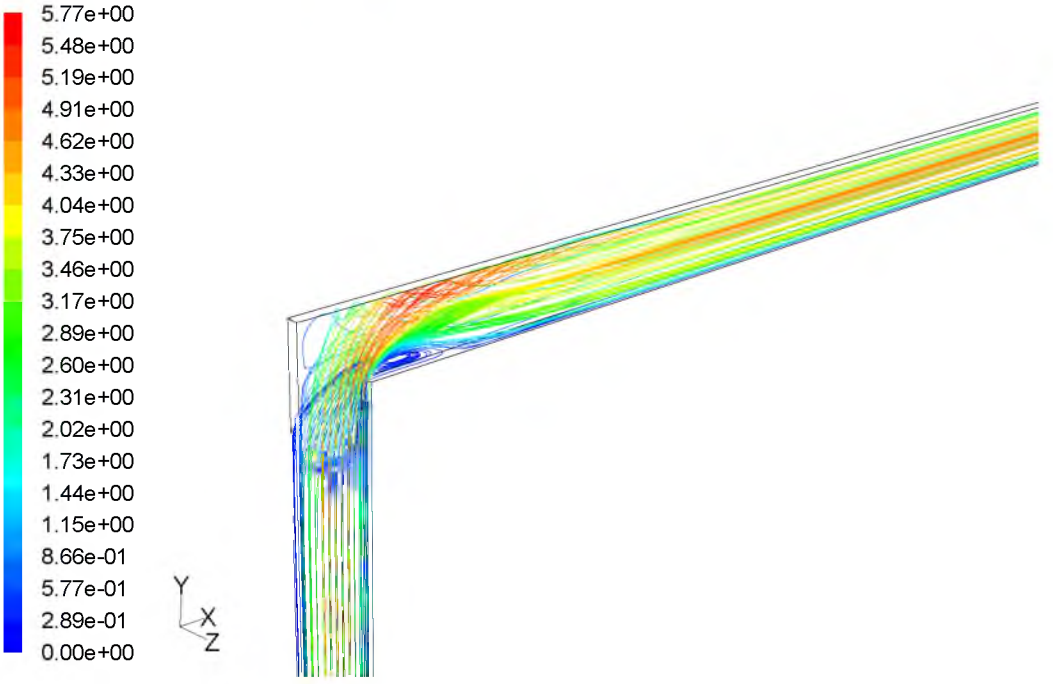

(b) Streamlines for $A_r = 1.0$

Figure 4.14: **Contours of velocity magnitudes and streamlines** XIV**:** The figure shows the contours of the velocity magnitude at various planes along the microchannel and the streamlines for $A_r = 1$ and $Re = 400$.

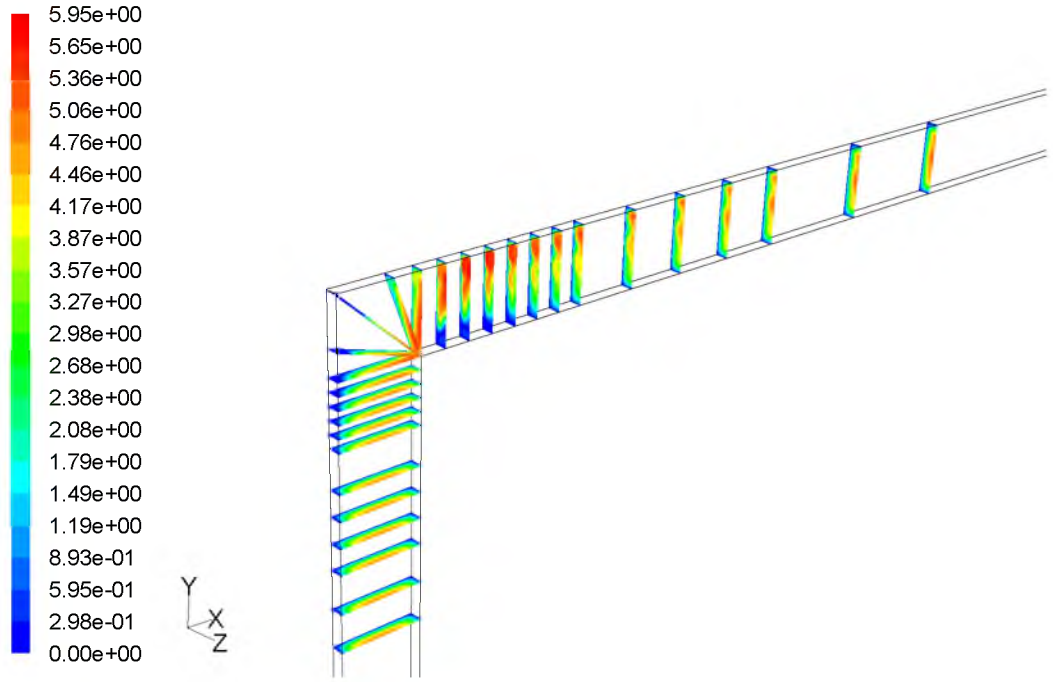

(a) Velocity magnitudes for $A_r = 0.91$

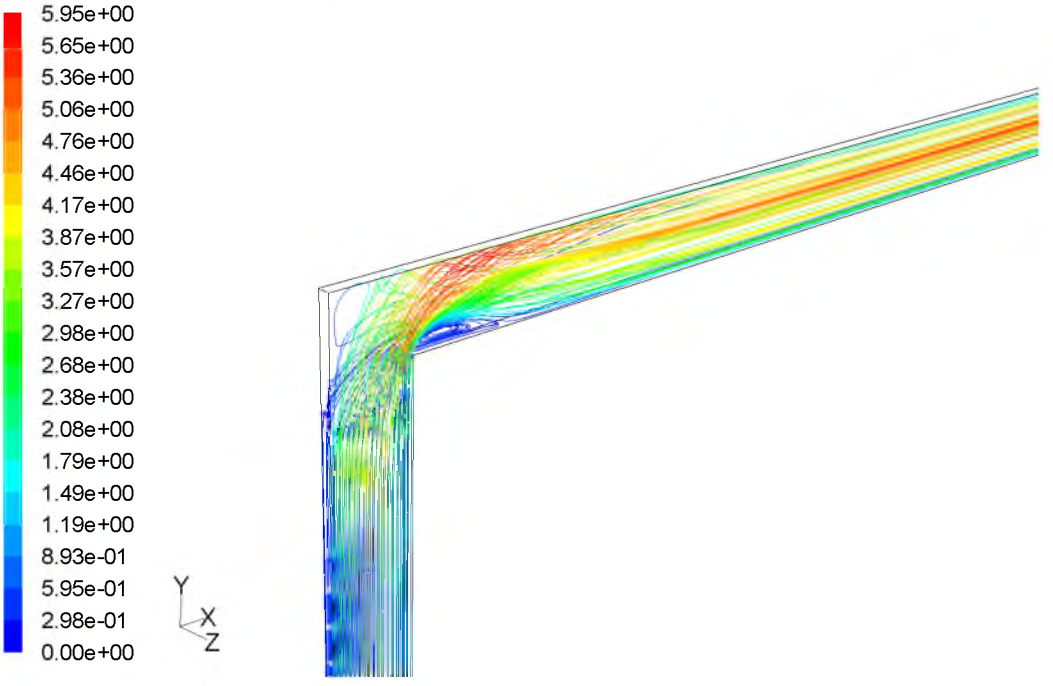

(b) Streamlines for $A_r = 0.91$

Figure 4.15: **Contours of velocity magnitudes and streamlines** XV**:** The figure shows the contours of the velocity magnitude at various planes along the microchannel and the streamlines for $A_r = 0.91$ and $Re = 400$.

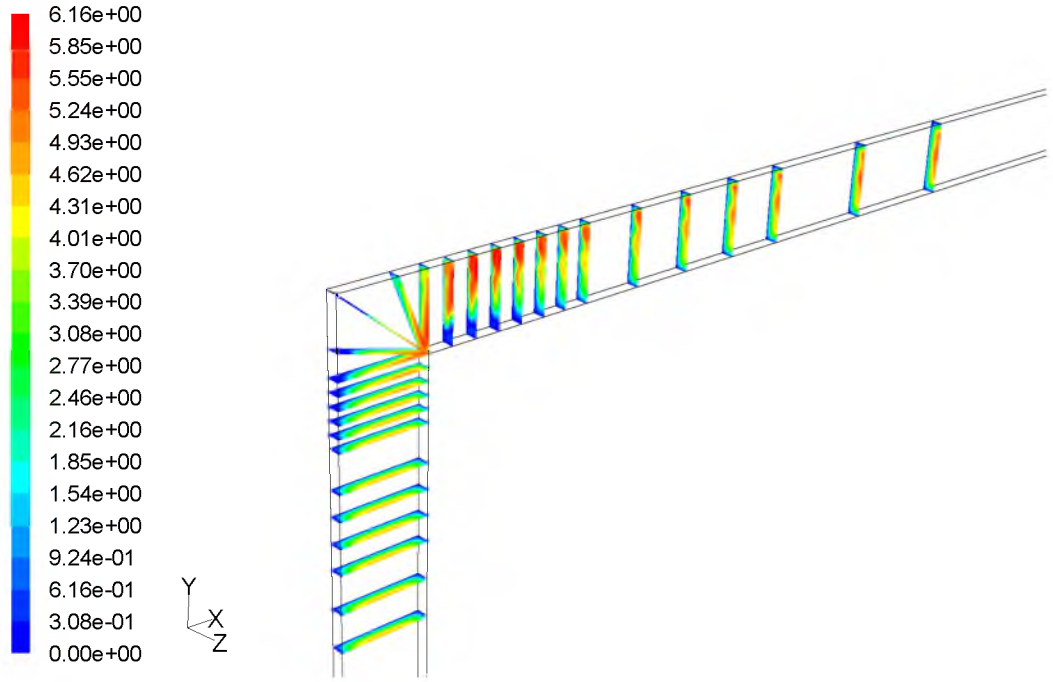

(a) Velocity magnitudes for $A_r = 0.84$

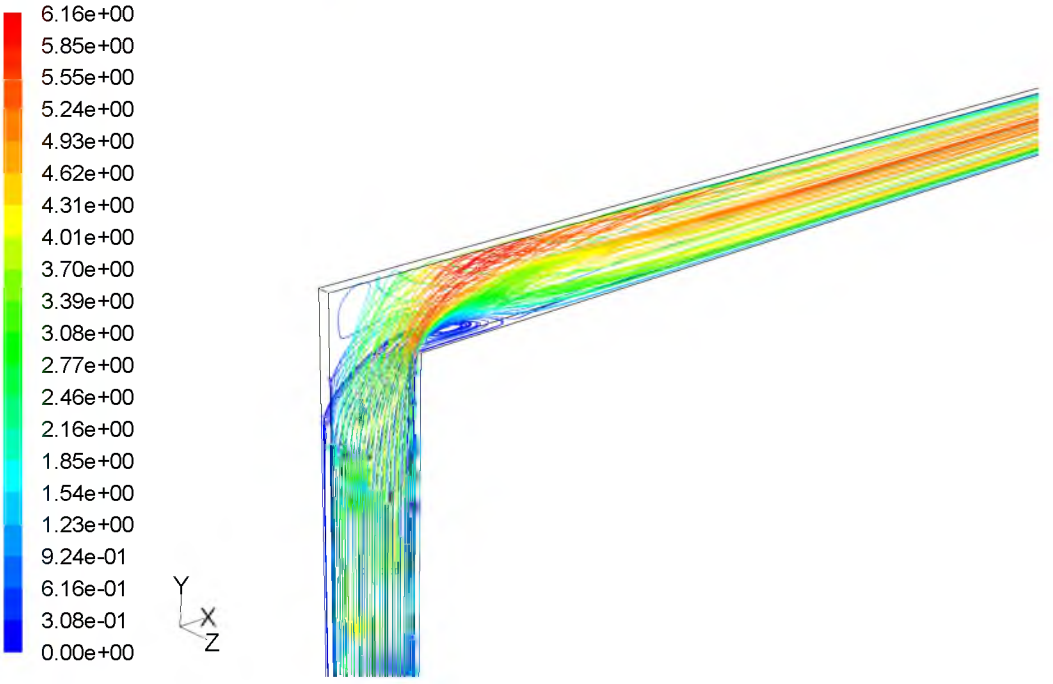

(b) Streamlines for $A_r = 0.84$

Figure 4.16: **Contours of velocity magnitudes and streamlines** XVI**:** The figure shows the contours of the velocity magnitude at various planes along the microchannel and the streamlines for $A_r = 0.84$ and $Re = 400$.

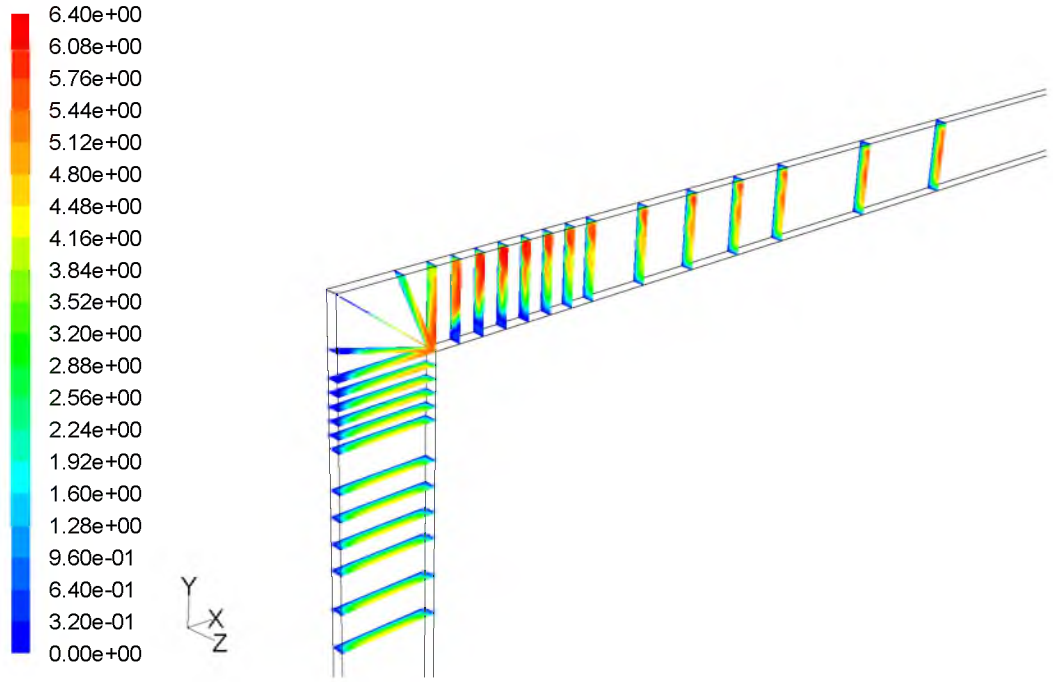

(a) Velocity magnitudes for $A_r = 0.77$

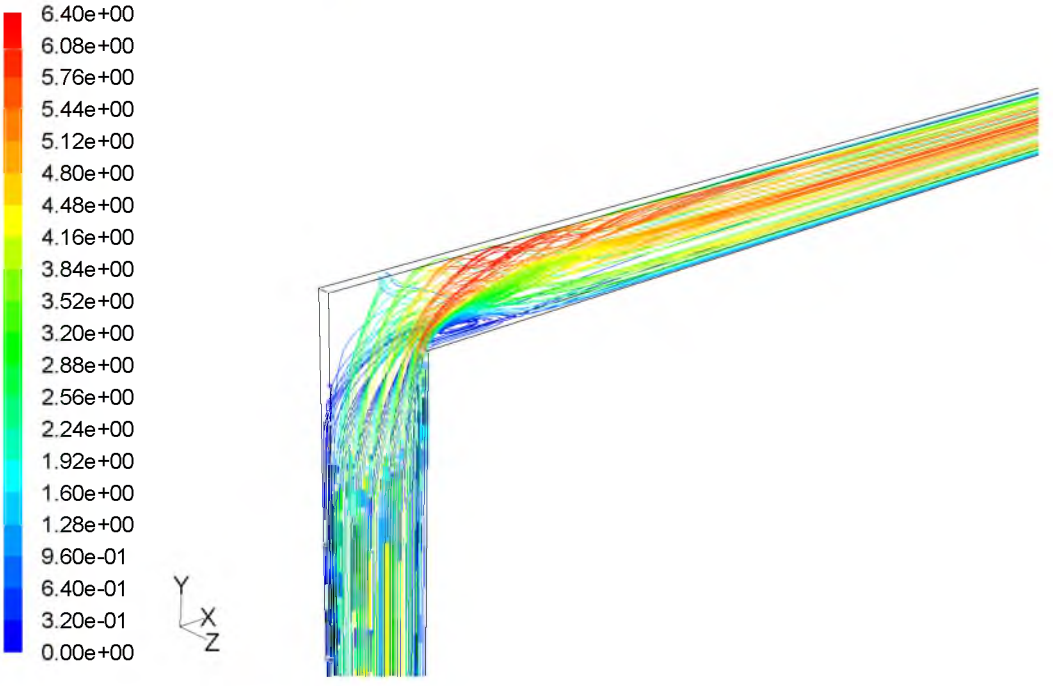

(b) Streamlines for $A_r = 0.77$

Figure 4.17: **Contours of velocity magnitudes and streamlines** *XVII*: The figure shows the contours of the velocity magnitude at various planes along the microchannel and the streamlines for $A_r = 0.77$ and $Re = 400$.

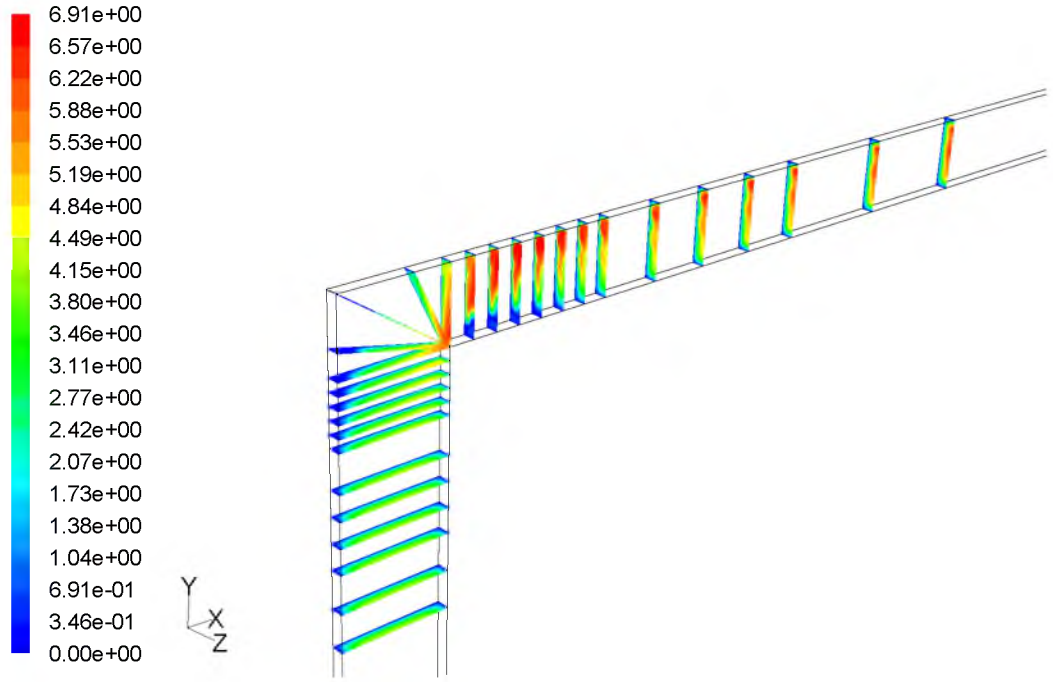

(a) Velocity magnitudes for $A_r = 0.66$

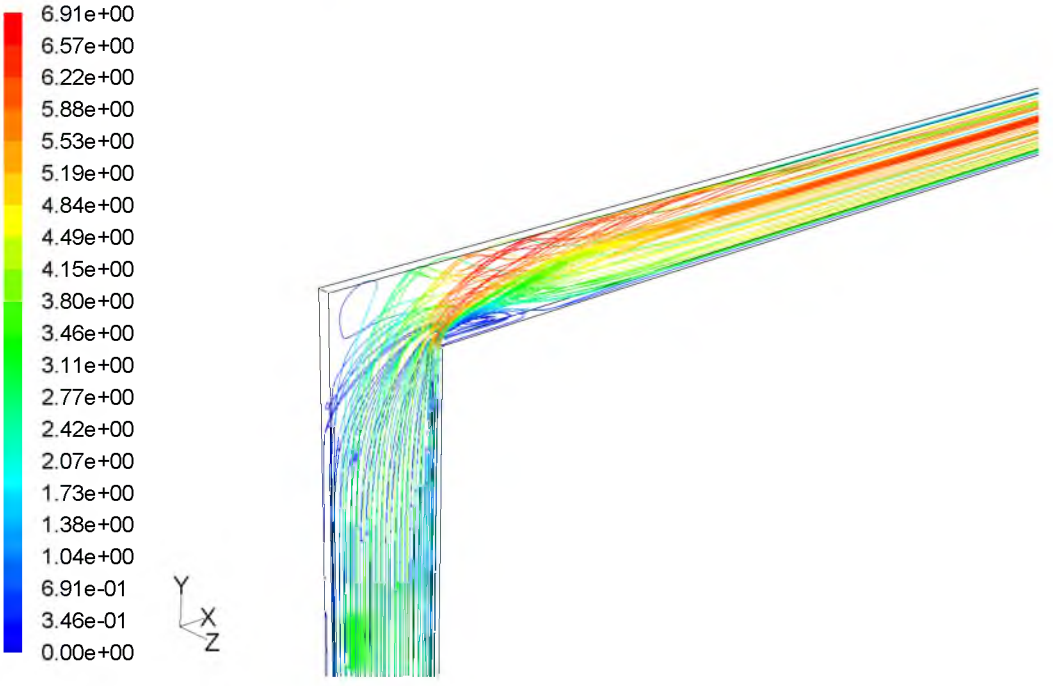

(b) Streamlines for $A_r = 0.66$

Figure 4.18: **Contours of velocity magnitudes and streamlines** *XVIII*: The figure shows the contours of the velocity magnitude at various planes along the microchannel and the streamlines for $A_r = 0.66$ and $Re = 400$.

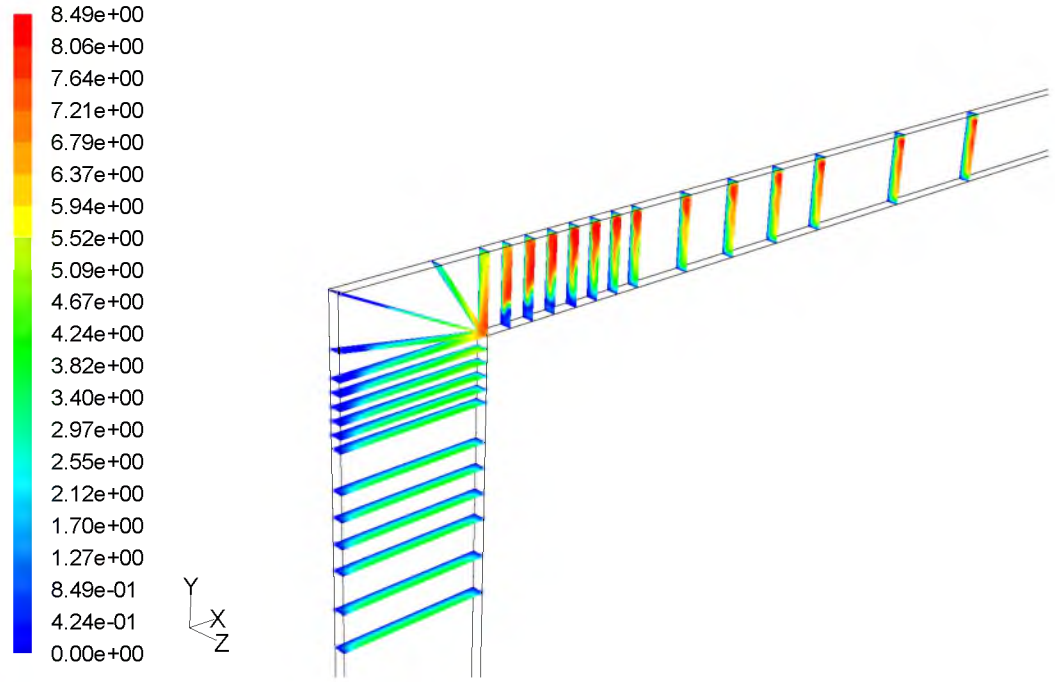

(a) Velocity magnitudes for $A_r = 0.50$

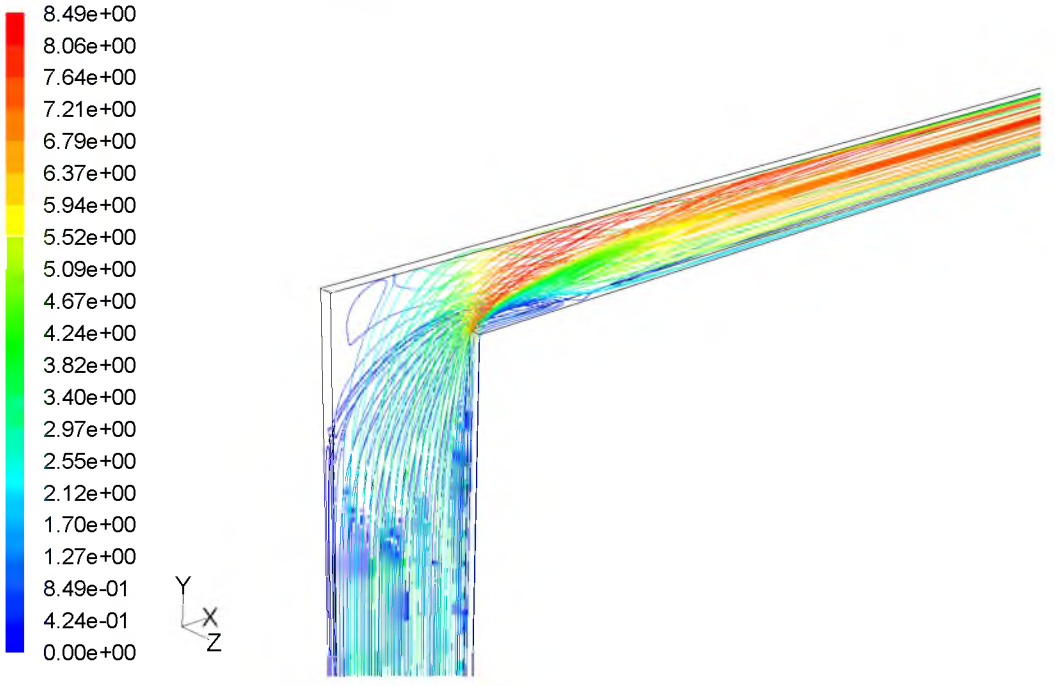

(b) Streamlines for $A_r = 0.50$

Figure 4.19: **Contours of velocity magnitudes and streamlines** XIX**:** The figure shows the contours of the velocity magnitude at various planes along the microchannel and the streamlines for $A_r = 0.50$ and $Re = 400$.

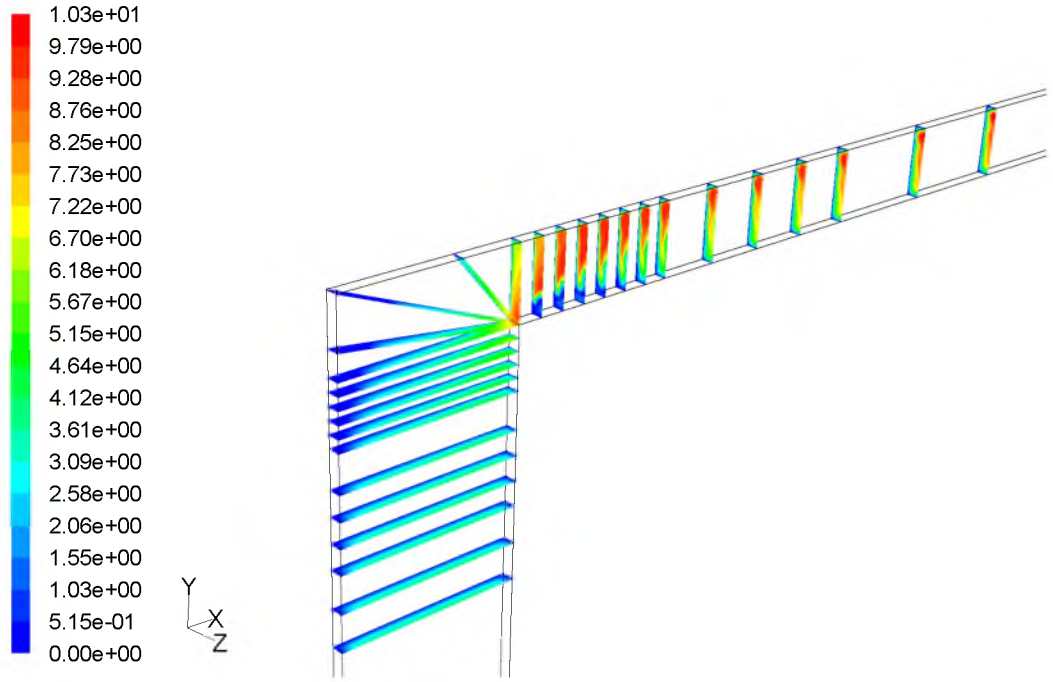

(a) Velocity magnitudes for $A_r = 0.40$

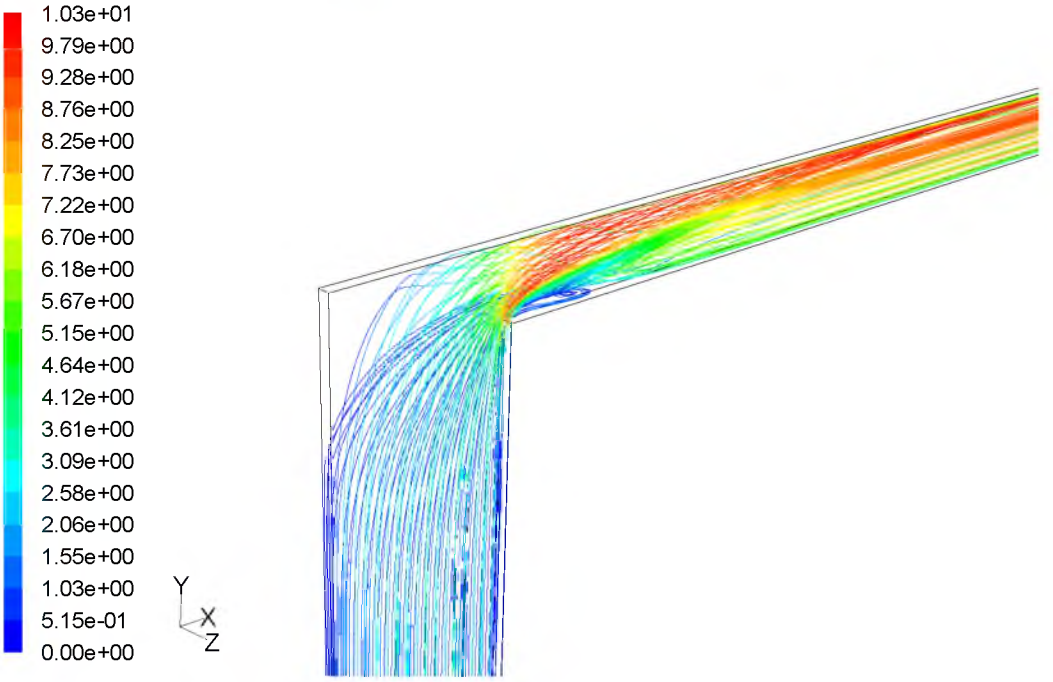

(b) Streamlines for $A_r = 0.40$

Figure 4.20: **Contours of velocity magnitudes and streamlines XX:** The figure shows the contours of the velocity magnitude at various planes along the microchannel and the streamlines for $A_r = 0.40$ and $Re = 400$.

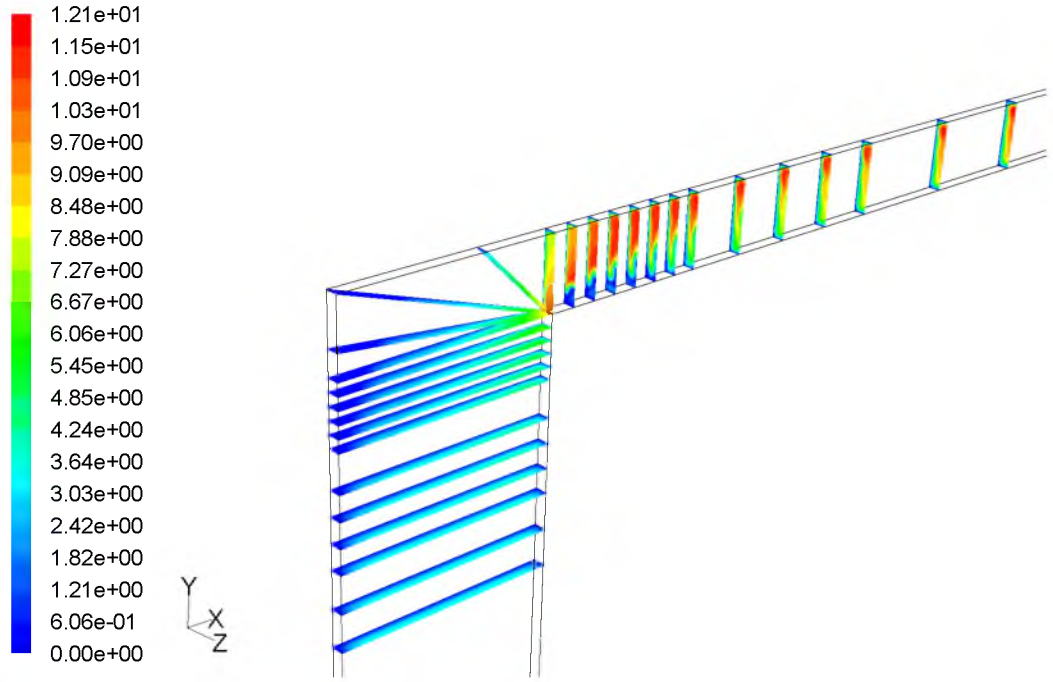

(a) Velocity magnitudes for $A_r = 0.33$

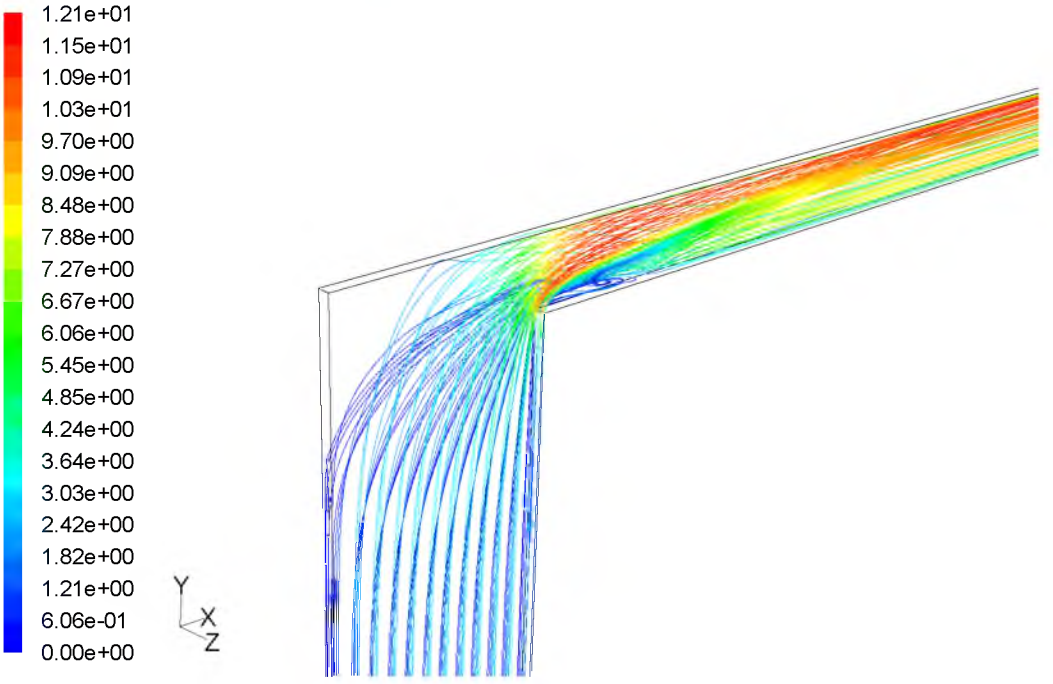

(b) Streamlines for $A_r = 0.33$

Figure 4.21: **Contours of velocity magnitudes and streamlines** XXI**:** The figure shows the contours of the velocity magnitude at various planes along the microchannel and the streamlines for $A_r = 0.33$ and $Re = 400$.

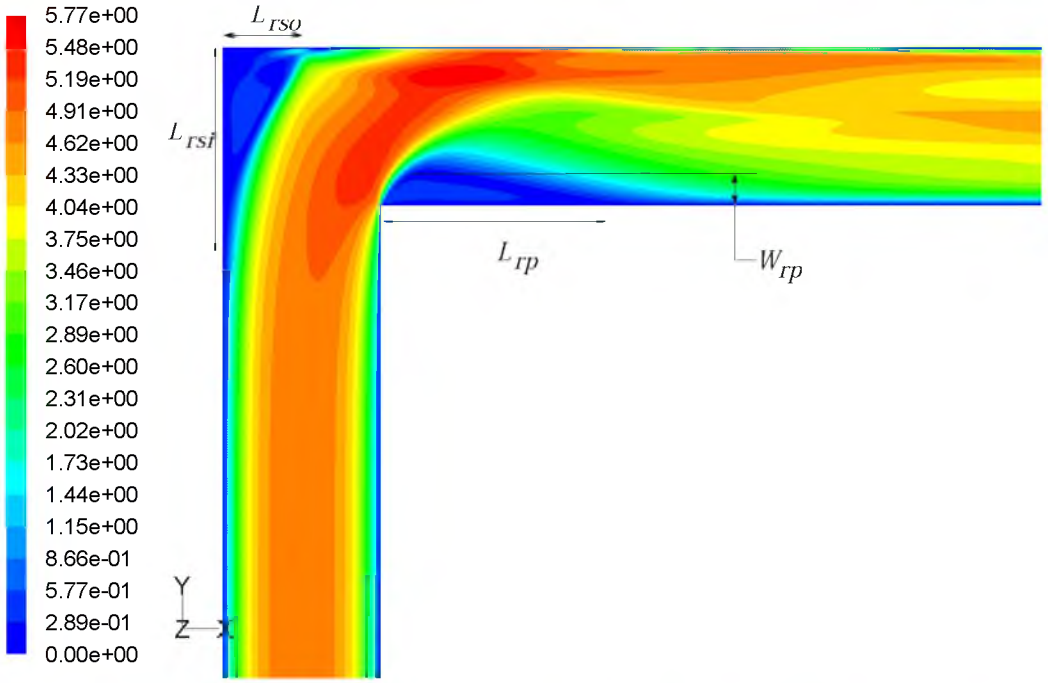

(a) Velocity magnitude in the symmetry plane

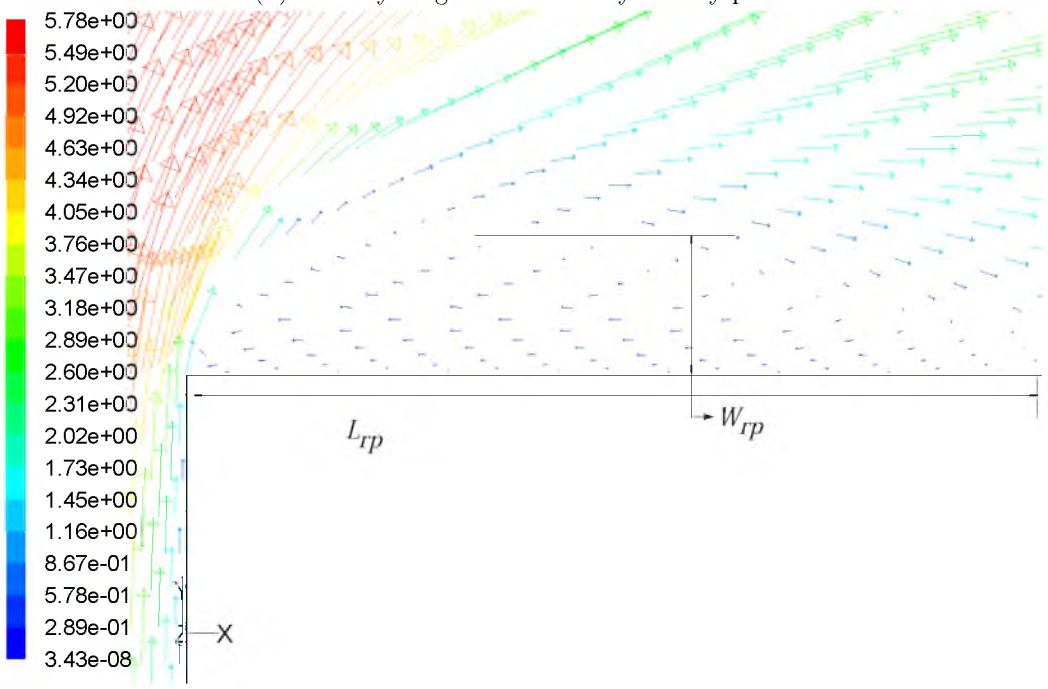

(b) Velocity vectors plot in the primary recirculation zone

Figure 4.22: **Dimensions of recirculation zones:** The above images show the dimensions of the primary and secondary recirculation zones and their measurement references. (b) is a zoomed in view of (a) showing the velocity vectors and height of the core of the primary recirculation zone

4.3.1 Primary zone

The length of the primary recirculation zone L_{rp} is evaluated by checking the change in the direction of the shear stress at the inner wall of the outlet channel. This assessment is equivalent to checking the sign change of the derivative of the axial velocity component with respect to the transverse direction, i.e., the sign change of $\left(\frac{\partial u}{\partial y}\right)$ from negative to positive along the inner wall of the outlet channel. The width of the primary recirculation zone is evaluated by determining the node which has the highest value of the y-coordinate in the outlet channel at which the axial component of the velocity is still negative or zero. A linear-interpolation is performed to obtain the actual y-coordinate where axial-velocity was zero, if the axial velocity at the said node is negative.

Fig. (4.23) shows the ratio of the length of the primary recirculation zone to the inlet hydraulic diameter $\left(\frac{L_{rp}}{D_{hi}}\right)$ for the miter bend microchannels with different aspect ratios. Regardless of the aspect ratio, the flow separation after the bend begins at approximately $Re = 50$ for all microchannels and increases with increasing Reynolds number. For the $\alpha > 0.28$, the increase in L_{rp} is gradual for $Re > 500$, indicating that the length of the primary recirculation zone is nearly constant. This behavior can be attributed to the development of the axial vortex in the outlet channel.

The width of the primary recirculation zone increases with the aspect ratio of the outlet channel. As shown in Fig. (4.24), the ratio of the width of the primary recirculation zone (w_{rp}) to that of the width of the outlet channel (w_o) is the highest for the channel with $\alpha = 1.0$ at $\approx 50\%$, while the remaining channels are between 20% and 30%. The width of the recirculation zone remains constant for the smaller aspect ratio channels when $Re > 500$. The w_{rp} values for these channels are in agreement with those reported by Herwig et al. [44], in which the width of the primary recirculation zones is about 20% of the channel width for $Re > 500$.

As the area ratio of the microchannel at the miter bend is increased (i.e., for expansion channels), the length of the primary recirculation zone (L_{rpe}) increased gradually, as shown in Fig. (4.25), for $A_r = \{1.1, 1.2, 1.3, 1.5\}$. For higher area ratios (i.e., $A_r = \{2.0, 2.5, 3.0\}$), the L_{rpe} values are almost equal for all the Reynolds numbers considered in the simulations. The Reynolds number at which the flow

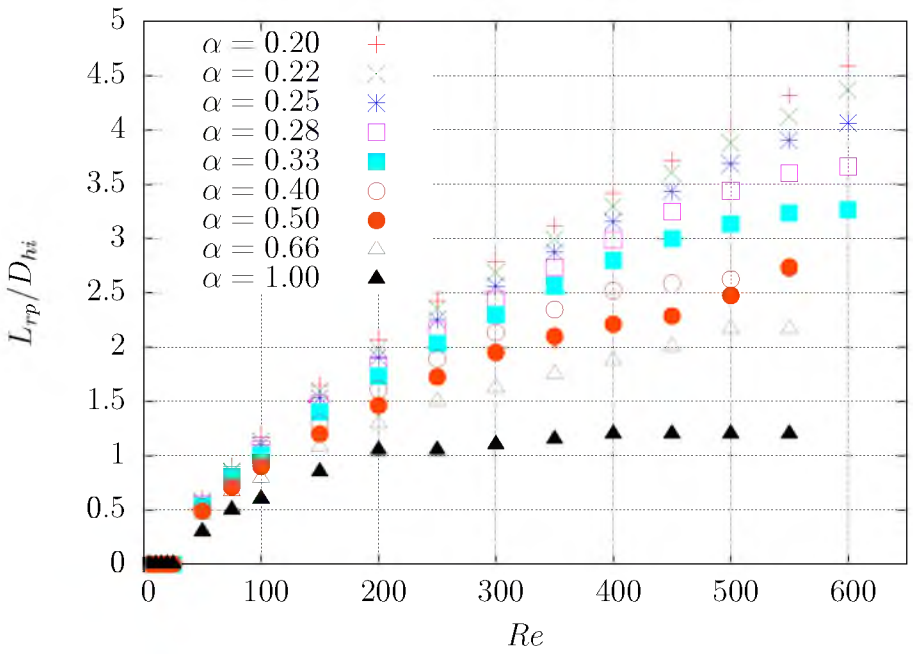

Figure 4.23: **Length of the primary recirculation zone:** The plot shows the ratio of the length of the primary recirculation zone downstream of the miter bend to the inlet hydraulic diameter.

separation begins is approximately $Re = 50$ for all the area ratios considered except for $A_r = \{2.0, 2.5, 3.0\}$. The flow separation for these higher A_r values begins at lower Reynolds number of approximately $Re = 25$. [1]

The width of the primary recirculation zone is nearly independent of A_r for small values of the area ratio $A_r = \{1.0, 1.2, 1.3\}$. The primary recirculation zone width increases steeply after the flow separation up to $Re = 200$, after which the increase is more gradual, as shown in Fig. (4.26). The maximum value of the primary recirculation zone width for these area ratios is between 20% and 25% of the width of the outlet channel. For the higher area ratios of $A_r = \{2.0, 2.5, 3.0\}$, the increase in w_{rpe} with area ratio is significantly high with the maximum values between 25% and 30% of the outlet channel width at $Re = 600$.

For contraction channels, [2] the length of the primary recirculation zone L_{rpc} for

[1]The Reynolds numbers for the expansion and contraction are calculated based on the inlet dimensions. Thus, for the expansion channel, the outlet average Reynolds number is less than that of the inlet.

[2]In this report, regardless of expansion or contraction, the area ratio (A_r) is defined as the ratio

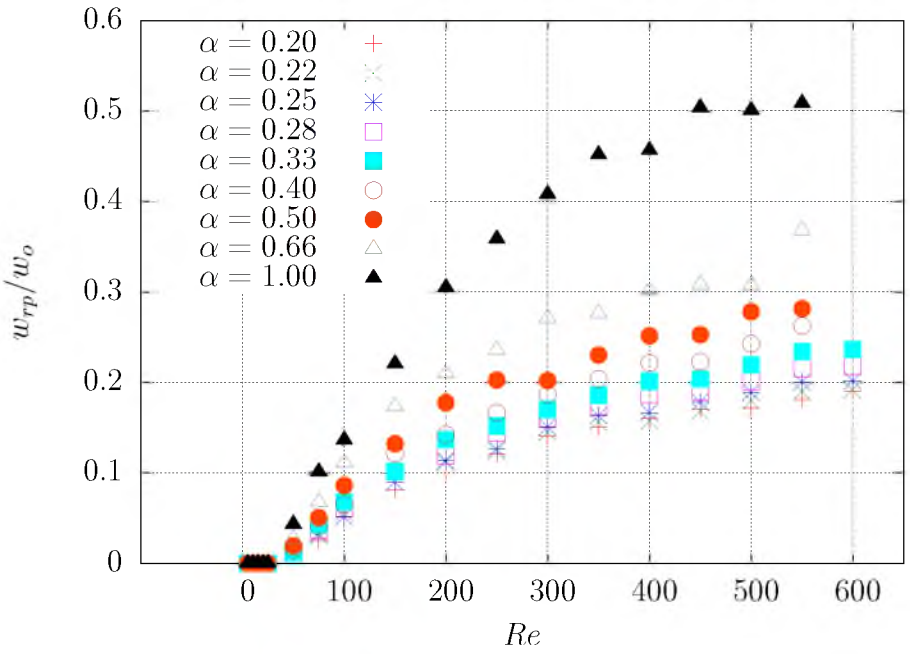

Figure 4.24: **Width of the primary recirculation zone:** The plot shows the ratio of the width of the primary recirculation zone to the width of the outlet channel in the miter bend microchannels.

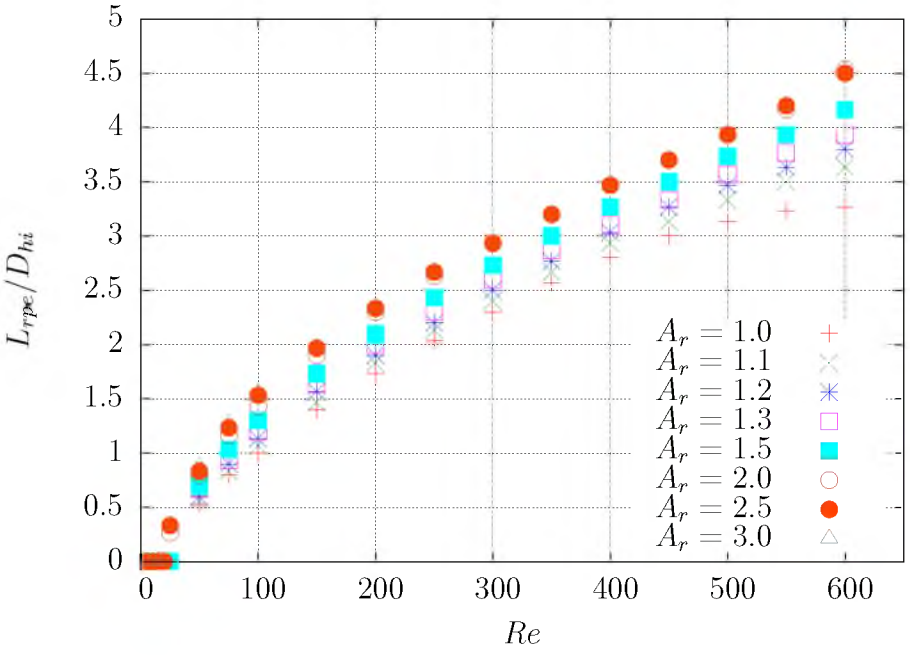

Figure 4.25: **Length of the primary recirculation zone (Expansion):** The plot shows the ratio of the length of the primary recirculation zone downstream of the miter bend to the inlet hydraulic diameter for the expansion channels.

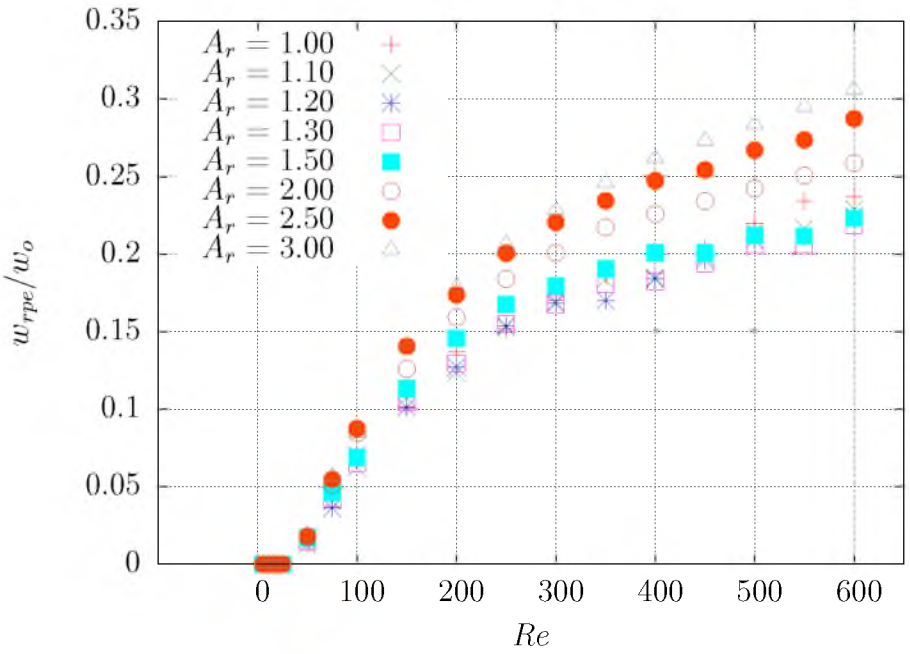

Figure 4.26: **Width of the primary recirculation zone (Expansion):** The plot shows the ratio of the width of the primary recirculation zone to the width of the outlet channel in the miter bend microchannels with abrupt expansion.

minor area ratios changes, i.e., for $A_r = \{0.91, 0.83, 0.77\}$, are nearly equivalent (see Fig. (4.27)). L_{rpc} increases slightly with the decreasing area ratio for these values of A_r in the Reynolds numbers range of $100 \leq Re < 500$, after which they begin to decrease with decreasing A_r, as shown in Fig. (4.27). This trend in the L_{rpc} results points to a shift of the peak value of L_{rpc} to smaller Reynolds number as the area ratio at the miter bend decreases, which is highly magnified in the case of $A_r = \{0.50, 0.40, 0.33\}$. The peak values of L_{rpc} in these latter cases occur at $Re \approx \{450, 400, 350\}$, respectively.

The decreasing trend of L_{rpc} after the peak value can be attributed to the development of the axial vortex flow in the outlet channel. The Reynolds number at which the axial vortex begins to develop decreases with decreasing A_r as the outlet channel's average flow Reynolds number (Re_o) is significantly increased due to flow acceleration. Because of this increase in Re_o, the transitions to turbulence occur at a smaller inlet Reynolds numbers with decreasing area ratios.

The width of the primary recirculation zone in contraction channels increases

---

of the cross-sectional area of the outlet to that of the inlet.

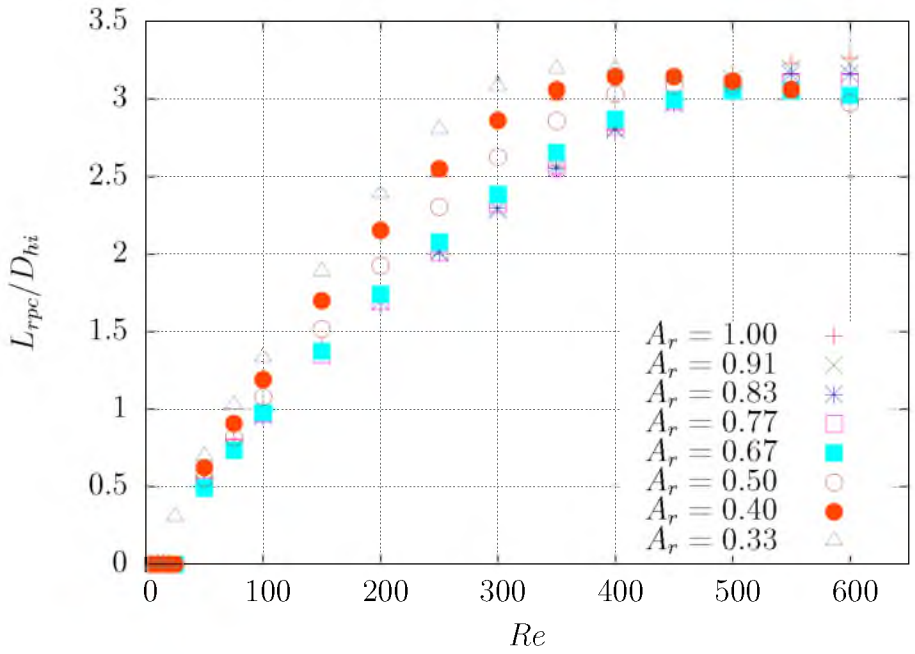

Figure 4.27: **Length of the primary recirculation zone (Contraction):** The plot shows the ratio of the length of the primary recirculation zone downstream of the miter bend to the inlet hydraulic diameter for the contraction channels.

with the decreasing area ratio of the channel, as shown in Fig. (4.28), for the smaller area ratios of $A_r = \{0.4, 0.33\}$. At higher contraction area ratios, w_{rpc} is nearly independent of A_r over the entire range of Reynolds number. A reason for this behavior of w_{rpc} is the constant dimensions of the outlet channel in all of these contraction channels.

4.3.2 Secondary zone

A secondary recirculation zone is developed on the outer corner of the miter bend, the dimensions of which are shown in Fig. (4.22). The length and depth of the secondary recirculation zones, L_{rso} and L_{rsi} (see Fig. (4.22)), are calculated in a similar way as that of L_{rpc}. The ratio of L_{rso} to the inlet hydraulic diameter of the channel is shown in Fig. (4.29) for various aspect ratios of the microchannel. A very small secondary recirculation zone, on the order of $\approx 0.25 D_{hi}$ in both length and depth, exists from $Re = 5$ and up in all the channels considered. As the Reynolds number increases, L_{rso} steeply increases to a peak value, after which it remains nearly constant with increasing Re for the microchannels with larger aspect ratios. As the

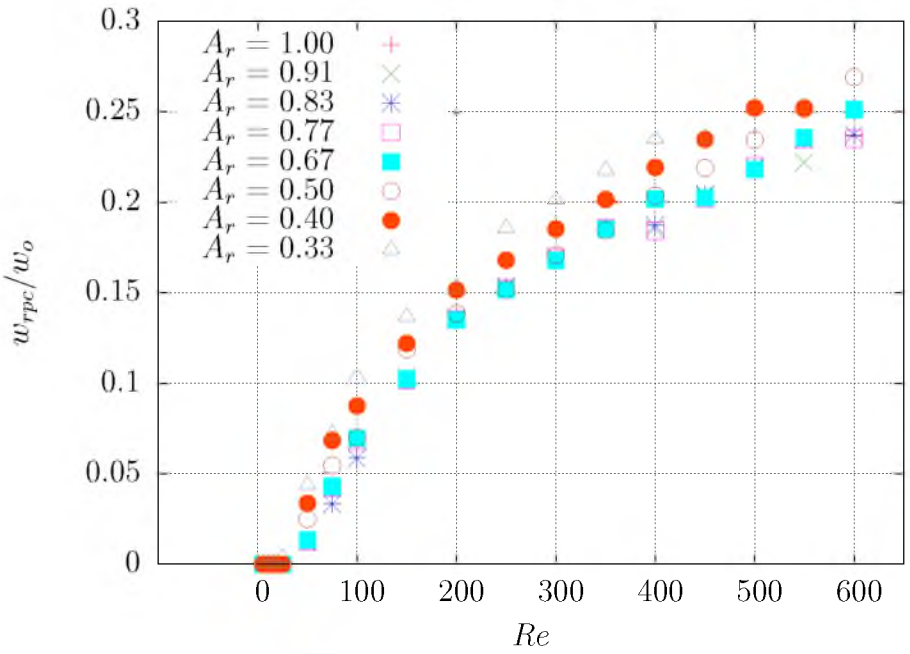

Figure 4.28: **Width of the primary recirculation zone (Contraction):** The plot shows the ratio of the width of the primary recirculation zone to the width of the outlet channel in the miter bend microchannels with abrupt contraction.

aspect ratio decreases, the change in L_{rso} with Re for the smaller Reynolds numbers reduces gradually to an almost constant value for $\alpha = 0.2$. The magnitude of the steep increase in L_{rso} increases with decreasing aspect ratio with a maximum value of $\approx 2.2D_{hi}$ for $\alpha = 0.2$. This steep rise in L_{rso} is likely a result of the increase in the width and magnitude of the primary recirculation zone. The maximum value of L_{rso} is limited by the width of the inlet channel (w_i) and the peak value decreases with increasing aspect ratio. [3]

Fig. (4.30) shows the ratio of L_{rsi} to the hydraulic diameter of the inlet channel for various aspect ratios. The depth of the secondary recirculation zone L_{rsi} into the inlet channel follows a similar trend as that of L_{rso} for the smaller Reynolds number, where it remains nearly constant for the smaller aspect ratio to a gradual increase at the higher aspect ratio. Furthermore, the magnitude of the steep increase in L_{rsi} increases with the decreasing aspect ratio and the Reynolds number at which this

[3]In the present set of simulations, the height of the channels is constant and the aspect ratio of the channels is varied by changing the width of the channels. Therefore, L_{rso} and α are inversely proportional.

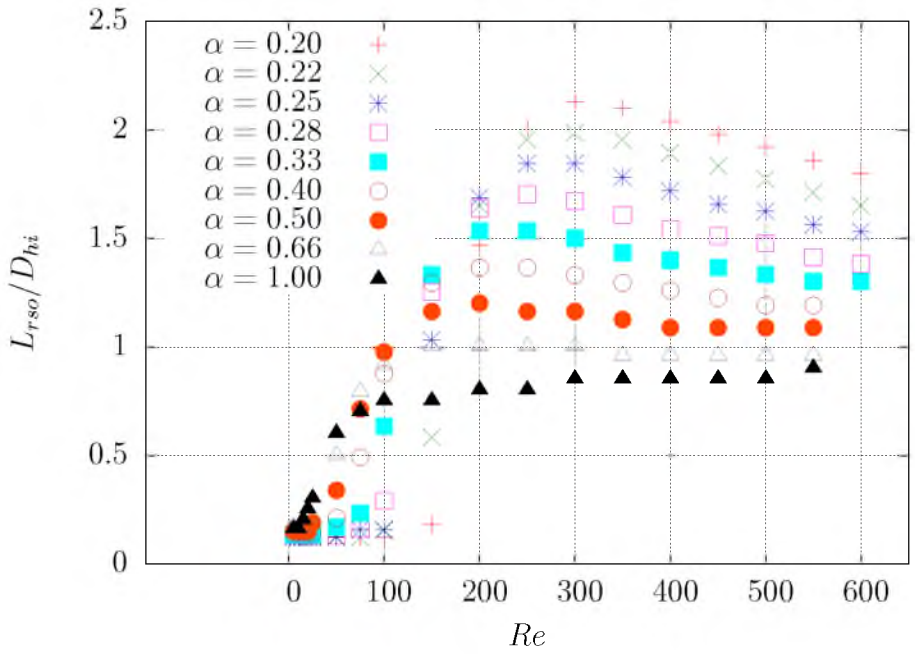

Figure 4.29: **Length of the secondary recirculation zone:** The plot shows the ratio of the length of the secondary recirculation zone downstream of the miter bend to the inlet hydraulic diameter.

increase occurs. The major difference in the trends of L_{rso} and L_{rsi} is that after the steep increase, L_{rso} begins to decrease with the increasing Reynolds number, while L_{rsi} continues to increase with Re. This phenomenon is a direct result of the development of the axial vortex flow in the outlet channel, where the flow structure along the outer wall changes from the axial to the transverse direction due to the vortex.

The effect of abrupt expansions at the miter bend on the length of the secondary recirculation zone L_{rsoe} can be observed in Fig. (4.31). The increasing area ratio effect on L_{rsoe} is the inverse of that on L_{rso}, as shown in Fig. (4.29). The peak value of L_{rsoe} increases with the increase in the area ratio of the expansion. The Reynolds number up to which the initial value of L_{rsoe} remains constant increases with the increasing area ratio as well as the magnitude of the steep increase in L_{rsoe}. Further, L_{rsoe} remains nearly constant for $Re > 550$ regardless of the magnitude of the area ratio of the expansion.

The depth of the secondary recirculation zone L_{rsie} into the inlet channel increases

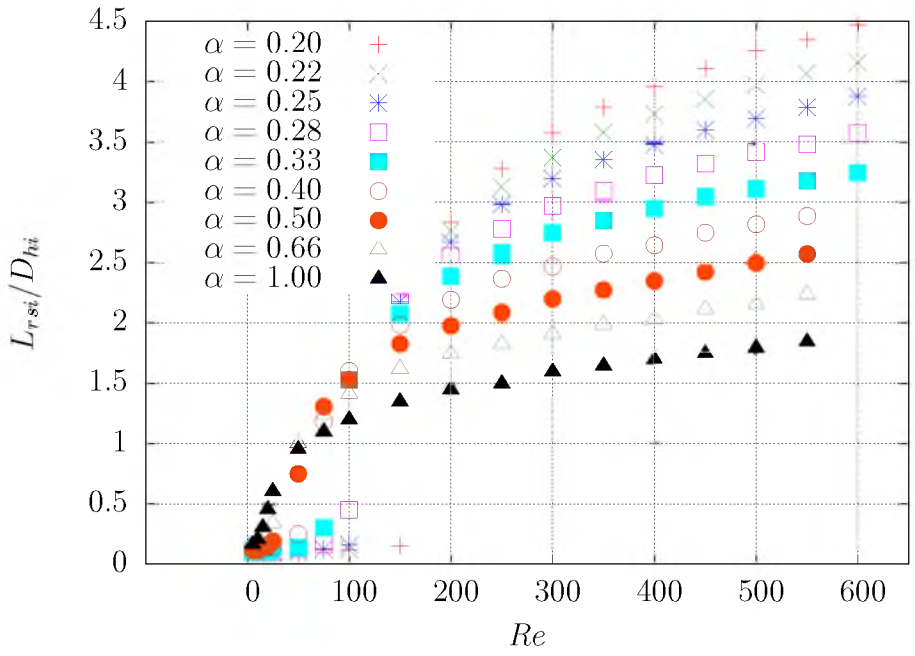

Figure 4.30: **Depth of the secondary recirculation zone:** The plot shows the ratio of the depth of the secondary recirculation zone upstream of the miter bend to the inlet hydraulic diameter.

with an increase in the area ratio of expansion at the miter bend. The values of L_{rsie} for the flows with $5 \leq Re \leq 600$ and $1.0 \leq A_r \leq 3.0$ are shown in Fig. (4.32). It is interesting to note that a steep increase in L_{rsie} occurs at $Re = 100$ for minor area ratio changes, i.e., for $A_r = \{1.0, 1.1, 1.2, 1.3, 1.5\}$, while for $A_r = \{2.0, 2.5, 3.0\}$, this steep gradient occurs at $Re = 150$, which indicates that the flow separation is delayed due to deceleration. Further, the L_{rsie} gradient reduces gradually, after the steep increase, with increasing Reynolds number tending towards a near constant value of L_{rsie} for all A_r values.

The contraction channels, on the other hand, show a very interesting behavior with decreasing A_r. From Fig. (4.33), it can be noted that for minor contractions, i.e., for $A_r = \{1.0, 0.91, 0.84, 0.77, 0.67\}$, $Re = 250$ acts as a pivot point. At this point, the decreasing trend of the L_{rsoc} with decreasing A_r changes to an increasing trend. Further, the peak value of L_{rsoc} is almost equal for minor contractions while it increases significantly for major contractions at the miter bend. In addition, the Reynolds number at which the steep increase in the magnitude of L_{rsoc} occurs

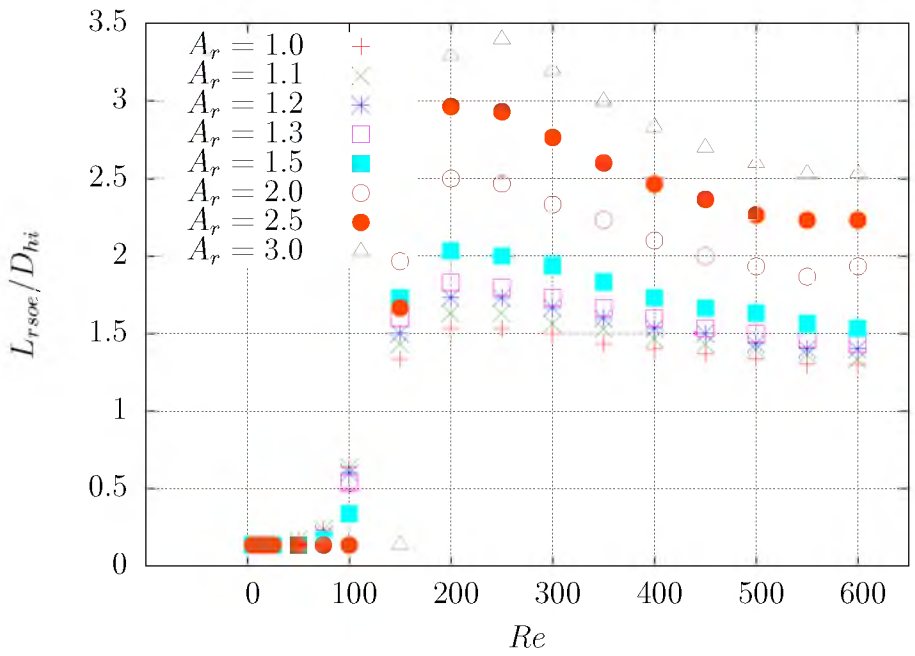

Figure 4.31: **Length of the secondary recirculation zone (Expansion):** The plot shows the ratio of the length of the secondary recirculation zone downstream of the miter bend to the inlet hydraulic diameter for the expansion channels.

increases with decreasing A_r. A comparison of Fig. (4.33) with Fig. (4.31) shows that the Reynolds number at which the peak value of L_{rso} occurs and the axial vortex develops is larger in the contraction channels even though the flow is accelerated. This is because the Reynolds number in both cases is calculated based on the inlet hydraulic diameter, and D_{hi} for the contraction channels is larger than that for the expansion channels.

A similar pivot point at $Re = 250$ is present for the depth of the secondary recirculation zone L_{rsic} for the contraction channels. The ratio of L_{rsic} to that of the inlet hydraulic diameter for all the above contraction area ratios is shown in Fig. (4.34). L_{rsic} continues to increase gradually after a steep rise with increasing Reynolds number. From Fig. (4.34), it is also evident that for the minor contractions ratios of $0.67 \leq A_r \leq 1.0$, the change in L_{rsic} at higher Reynolds number is less than $\approx 2.0\%$, indicating a nearly constant value of L_{rsic}.

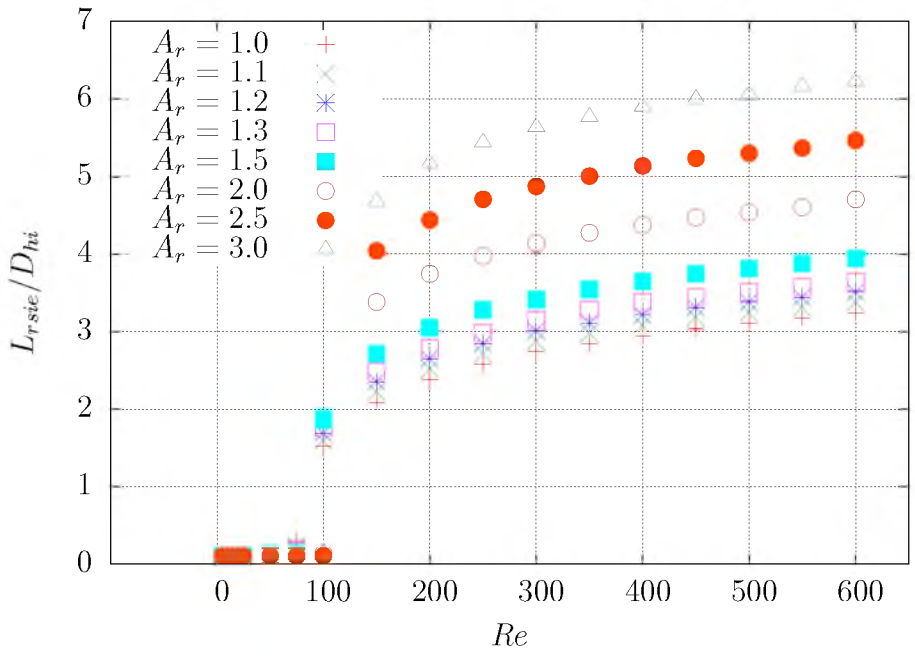

Figure 4.32: **Depth of the secondary recirculation zone (Expansion):** The plot shows the ratio of the depth of the secondary recirculation zone upstream of the miter bend to the inlet hydraulic diameter for the expansion channels.

4.4 Flow development length

The hydrodynamic development length in the outlet channels is estimated by comparing the root mean square difference between the axial velocity, i.e., the x-component of the velocity, at a plane normal to the flow direction in the outlet channel and the analytic velocity calculated using the Eq. (3.6). The distance of the plane from the bend where the *rms* average difference is less than 5% is taken as the flow development length (L_{dev}). A large value of *rms* difference is used here to account for the higher percentage differences of the boundary node values, due to small x-velocity, which increase the average value. For a microchannel with $\alpha = 0.33$, the flow development length in outlet channel from the simulation is compared to the theoretical predictions from the analytical model (see Eq. (2.12)) and the Martinelli equation (see Eq. (2.14)), as shown in Fig. (4.35). The figure shows that the Martinelli's equation underpredicts the development length, with a difference of more than 50%, over the entire Reynolds number range. This difference in L_{dev} can be attributed to the predevelopment of the flow in the simulations

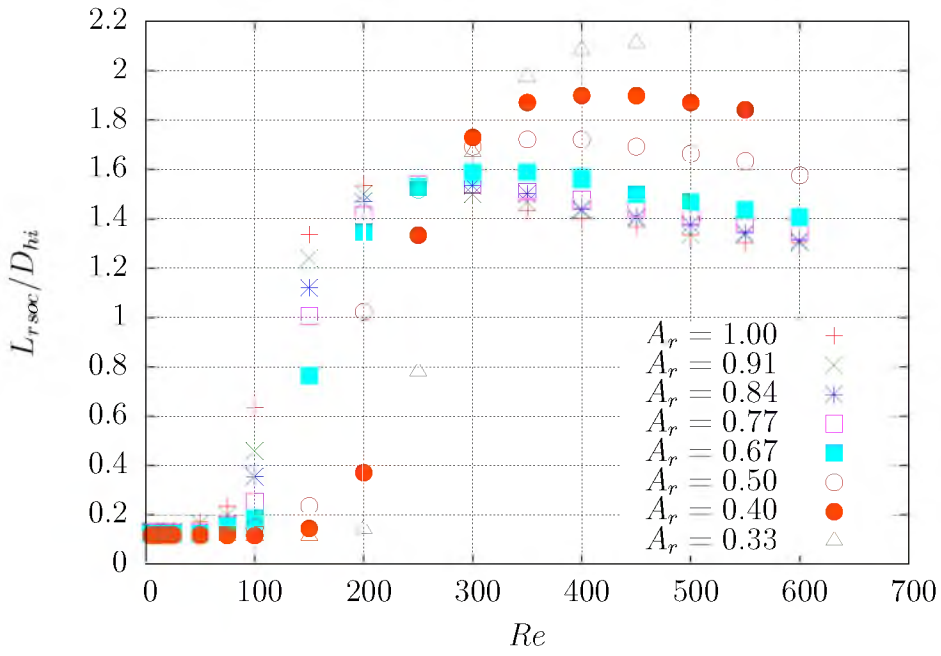

Figure 4.33: **Length of the secondary recirculation zone (Contraction):** The plot shows the ratio of the length of the secondary recirculation zone downstream of the miter bend to the inlet hydraulic diameter for the contraction channels.

conducted by Martinelli and Viktorov [50]. In their CFD simulations, the fluid entered a straight microchannel from a vast tank, resulting in a symmetric and evenly distributed velocity profile at the inlet, where as in the present simulations, the velocity distribution at the bend is highly three-dimensional with a recirculation zone. On the other hand, the conventional equation shows good agreement with the simulated development lengths for $Re \leq 250$, beyond which the L_{dev} is much smaller than the predicted value. Further, L_{dev} remains nearly constant for $250 \leq Re \leq 400$, where the axial vortex begins to take shape in the outlet channel.

A similar comparison of the development lengths for a high aspect ratio microchannel ($\alpha = 1.0$) with the theoretical model reported by Ahmad and Hassan [49] (see Eq. (2.13)), in addition to the above two equations, is shown in Fig. (4.36). In this figure, the flow development lengths from the simulation are in close agreement with the conventional equation up to a $Re = 200$. L_{dev} values estimated by the relation proposed by Ahmad and Hassan [49] for the channels with $\alpha = 1.0$ are also in close agreement with the simulations over the Reynolds number range. Once again, the

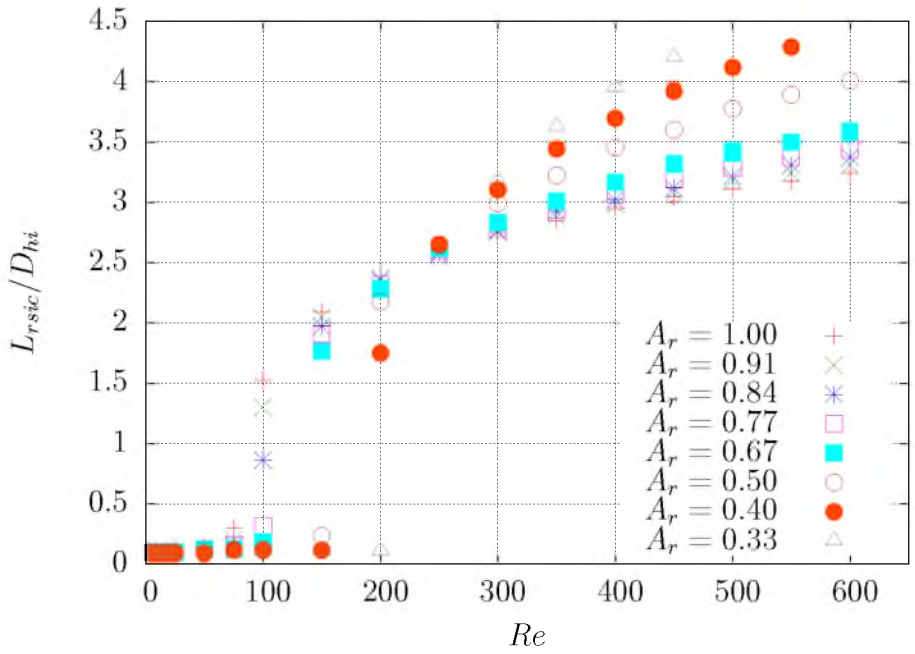

Figure 4.34: **Depth of the secondary recirculation zone (Contraction):** The plot shows the ratio of the depth of the secondary recirculation zone upstream of the miter bend to the inlet hydraulic diameter for the contraction channels.

simulated L_{dev} are far greater than the theoretical prediction by Martinelli's equation. It can be concluded from this observation that L_{dev} in the outlet channel for the miter bend microchannels agrees reasonably well with the conventional equation regardless of the aspect ratio of the microchannel.

Herwig et al. [44] reported that, for a square microchannel with $D_h = 100\,\mu m$ and a curved bend, the bend effects are observed as far as $\approx 15.2 D_h$ downstream of the bend for $Re = 512$, which is consistent with L_{dev}, as shown in Fig. (4.36). The difference in the values of the L_{dev} from the simulations and that reported by Herwig et al. [44] is due to the presence of a curved bend. Maharudrayya et al. [39] reported that the bend effects are observed for shorter distances downstream of the bend as the curvature ratio of the bend is increased and that the sharp bends (curvature ratio = 0) have a maximum L_{dev} for all the aspect ratios.

Fig. (4.37) shows the ratio of the flow development length (L_{dev}) in the outlet channel to the outlet hydraulic diameter (D_{ho}) for $0.2 \leq \alpha \leq 1$ over the Reynolds number range of $5 \leq Re \leq 600$. L_{dev} for $0.5 \leq \alpha < 1.0$ increases almost linearly

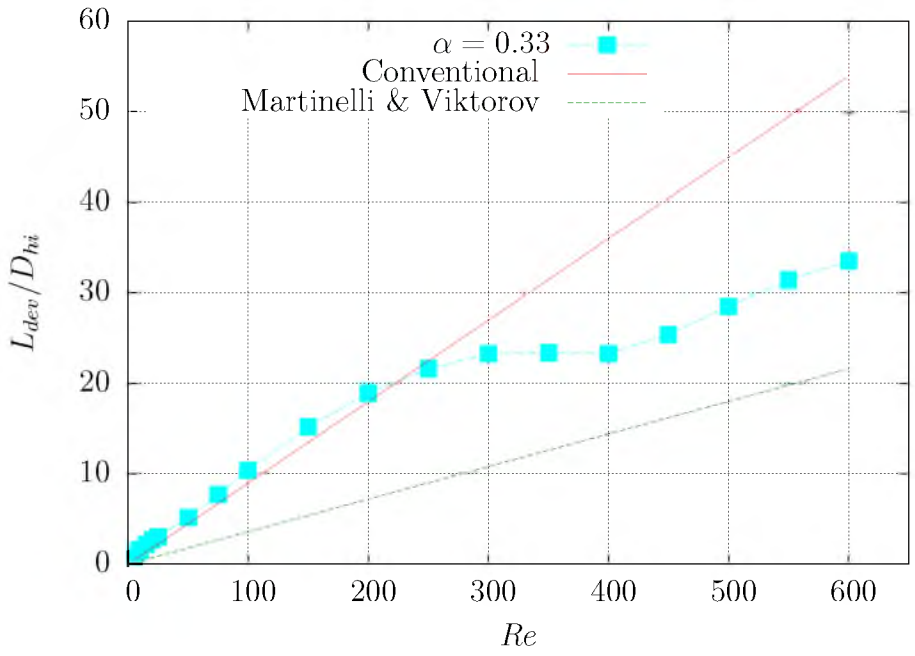

Figure 4.35: **Flow development length from theory and simulation** I **:** The plot compares the flow development length in the outlet channel for a microchannel with $\alpha = 0.33$ from the simulation to the theoretical values obtained from conventional and Martinelli's equation.

with Re, while for $0.2 \leq \alpha < 0.5$, L_{dev} shows a considerable deviation from the linear trend in the approximate Reynolds number range of $300 \leq Re \leq 500$ (see Fig. (4.36) and Fig. (4.35) for a clear distinction in the plots). It is also observed that the wider the channel (i.e., the smaller the aspect ratio), the larger is the Reynolds number at which the deviation from the linear behavior occurs. Further, as the aspect ratio of the channel increases from 0.20 to 0.40, L_{dev} decreases. In addition, the nonlinearity in the dependence of L_{dev} on Re phases out with the increase in the aspect ratio of the channel.

Increasing the area ratio at the miter bend of the microchannel results in the flow deceleration, effectively reducing the Re of the flow and also the aspect ratio of the channel. As shown in Fig. (4.38), L_{dev} decreases with increasing A_r for $Re \leq 300$, after which there is a significant deviation from linear response. Interestingly, in this range of Reynolds numbers ($400 \leq Re \leq 600$), L_{dev} decreases with the increasing A_r up to $A_r = 1.5$. In this range of A_r, flow deceleration plays a significant role on the L_{dev} value. An increase in A_r beyond 1.5 leads to the aspect ratio of the channel playing a

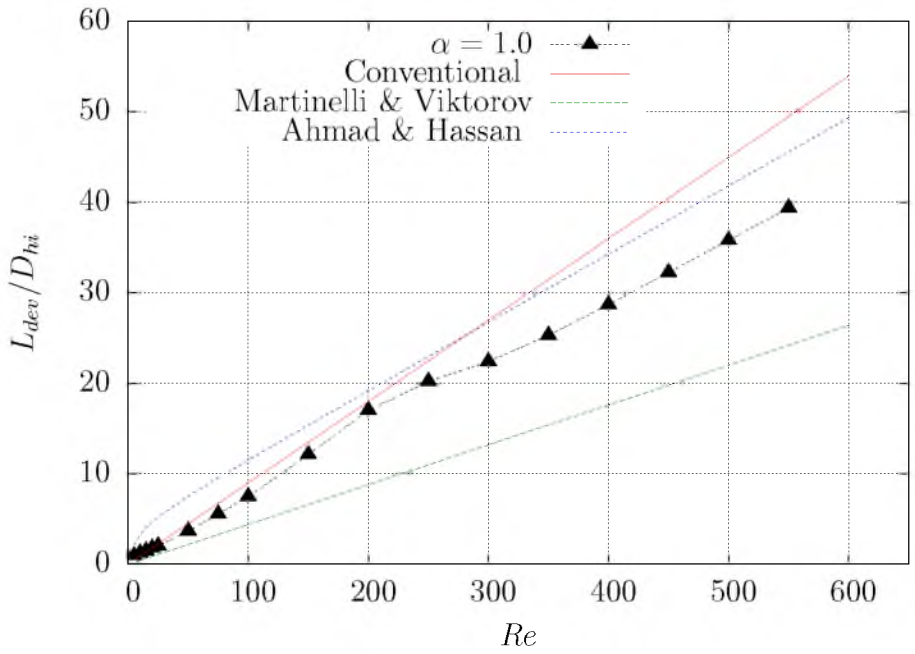

Figure 4.36: **Flow development length from theory and simulation** I **:** The plot compares the flow development length in the outlet channel for a microchannel with $\alpha = 1.0$ from the simulation to the theoretical values obtained from the conventional, Ahmad and Hassan's, and Martinelli's equations.

more significant role in the development length and results in the linear dependence on Re. Further, the increase in the development length with the increase in A_r is the result of the larger size of the primary recirculation zone at the higher Re in these channels. Notably, L_{dev} for larger area ratios (i.e., $A_r = \{2.5, 3.0\}$) is comparable to the L_{dev} of the miter bend microchannel with $A_r = 1.0$, at higher Reynolds numbers, which can also be attributed to the larger flow separation distances in the outlet channel at these area ratios.

On the other hand, decreasing the area ratio at the miter bend results in a larger L_{dev} for a constant Re at the channel inlet (see Fig. (4.39)). The resulting flow acceleration plays a significant role in the flow development length. The ratio of the outlet flow development length to the outlet channel hydraulic diameter is shown in the Fig. (4.39). At large A_r, L_{dev} is linearly related to Re (note that the D_{ho} is constant as A_r changes). The nonlinear dependence of L_{dev} on Re gradually phases out with the decreasing area ratio. The magnitude of L_{dev} for $A_r = 0.5$ is close to twice that for $A_r = 1.0$.

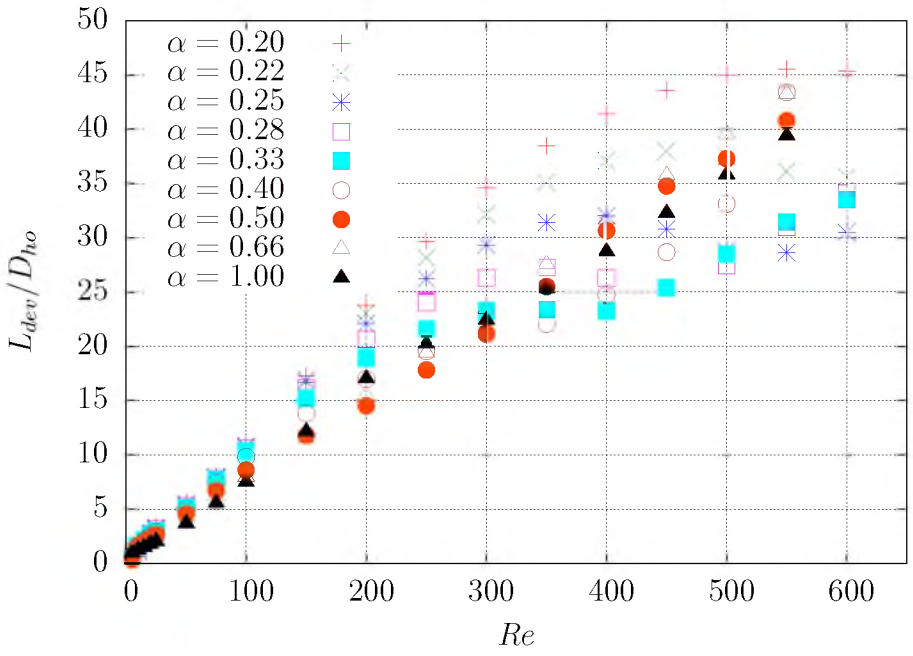

Figure 4.37: **Hydrodynamic development length in the outlet:** The plot shows the ratio of the hydrodynamic development length in the outlet channel to the hydraulic diameter of the outlet channel.

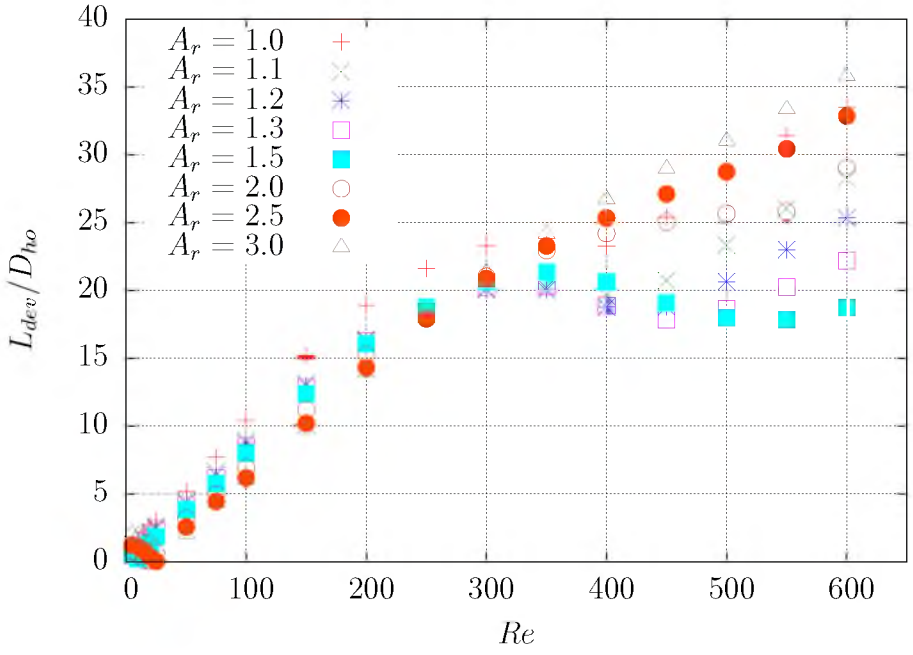

Figure 4.38: **Hydrodynamic development length in the outlet (Expansion Channel):** The plot shows the ratio of the hydrodynamic development length in the outlet channel to the hydraulic diameter of the outlet.

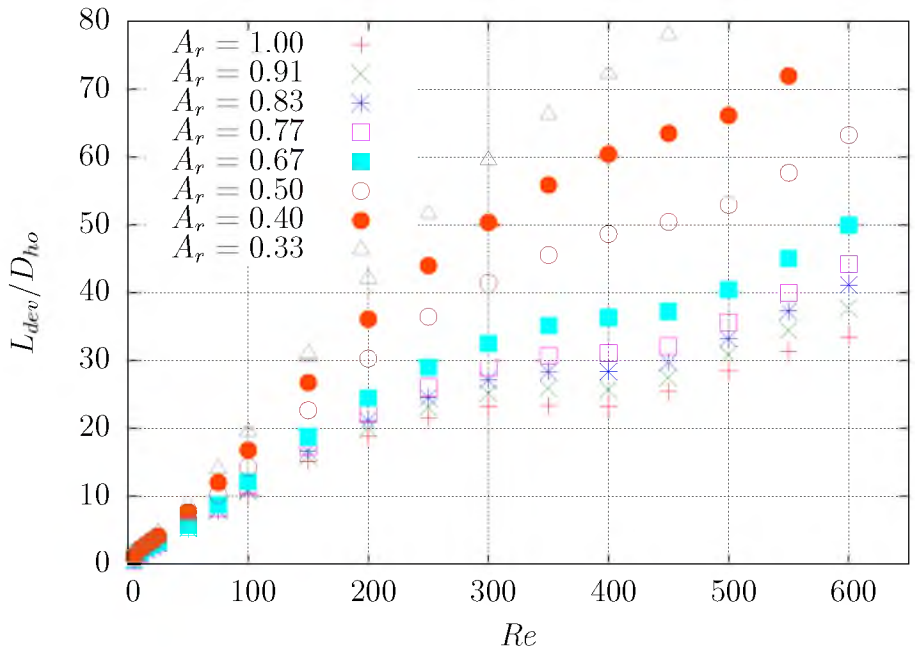

Figure 4.39: **Hydrodynamic development length in the outlet (Contraction Channel):** The plot shows the ratio of the hydrodynamic development length in the outlet channel to the hydraulic diameter of the outlet.

4.5 Excess loss coefficients

The bend excess losses are calculated by subtracting the frictional pressure losses from the total pressure drop across the miter bend microchannel. The flow far upstream and downstream of the bend is considered to be hydrodynamically fully developed; therefore, the calculated loss includes the bend effects on the flow in both the upstream and downstream channels. The ratio of the above losses to the mean kinetic head at the inlet of the channel (defined as K_b) are shown in Fig. (4.40) for $0.2 \leq \alpha \leq 1.0$ over the Reynolds number range considered for the simulations.

K_b decreases rapidly for all aspect ratios as the Reynolds number increases from $5 \leq Re \leq 100$; any increase in Re beyond 100 leads to a gradual increase of K_b. This trend is in agreement with the experimental bend excess loss coefficients reported by Xiong and Chung [43] and Maharudrayya et al. [39] for sharp bends. K_b increases with decreasing α in the Reynolds number range of $5 \leq Re < 100$ and the trend is reversed for $Re > 100$, as shown in Fig. (4.40). K_b values for the microchannel with $\alpha = 1.0$ are consistent with the excess loss coefficients reported by Herwig et al. [44]

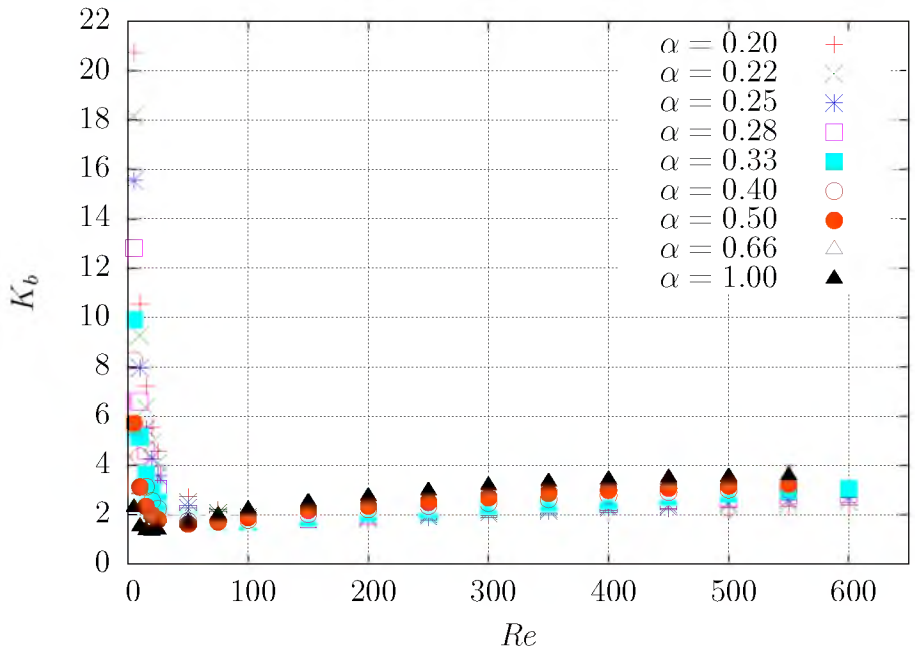

Figure 4.40: **Bend excess loss coefficients:** The plot shows the bend excess loss coefficients for the miter bend microchannels.

for a square microchannel of $D_h = 100\,\mu m$ with a curved bend. Although the K_b from the simulations in this work are a little higher, this is expected as the curved bends have smaller bend excess loss coefficients, as reported by Maharudrayya et al. [39].

The bend excess loss coefficients (K_b) from the present set of simulations are compared to the experimental results reported by Kolekar [16]. Fig. (4.41a) shows the excess loss coefficients calculated from the simulations, for the available Reynolds number range that overlaps with those from the experiments. A plot of the experimental bend excess loss coefficients is shown in Fig. (4.41b), which is adopted with the permission from the author. The aspect ratio of the channels used in these experiments are within the range of the aspect ratios used in the simulations. Channel A has the smallest aspect ratio of $\alpha = 0.196$ and channel G has the largest aspect ratio of $\alpha = 0.40$. The excess loss coefficients K_b for $\alpha = 0.2$ are in the range of 1.5 to 2.5 for $200 \leq Re \leq 600$, which agrees with the experimental results obtained from channel A ($\alpha = 0.196$) and channel B ($\alpha = 0.202$). Similarly, the excess loss coefficients for $\alpha = 0.33$ from the simulations are in close agreement with the loss coefficients from channel F ($\alpha = 0.334$). The aspect ratios of the channels in the

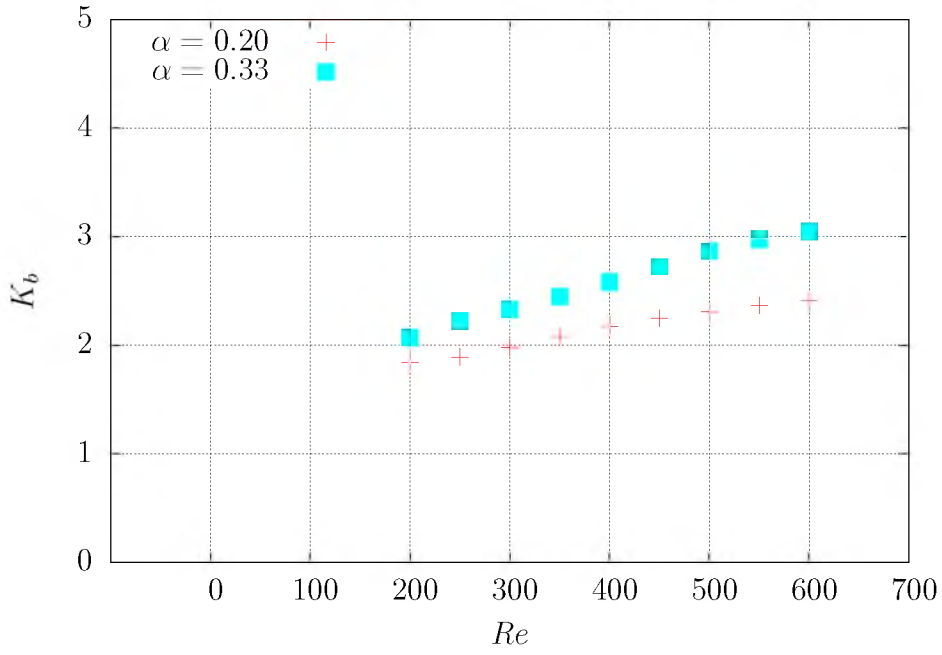

(a) K_b's from the simulations.

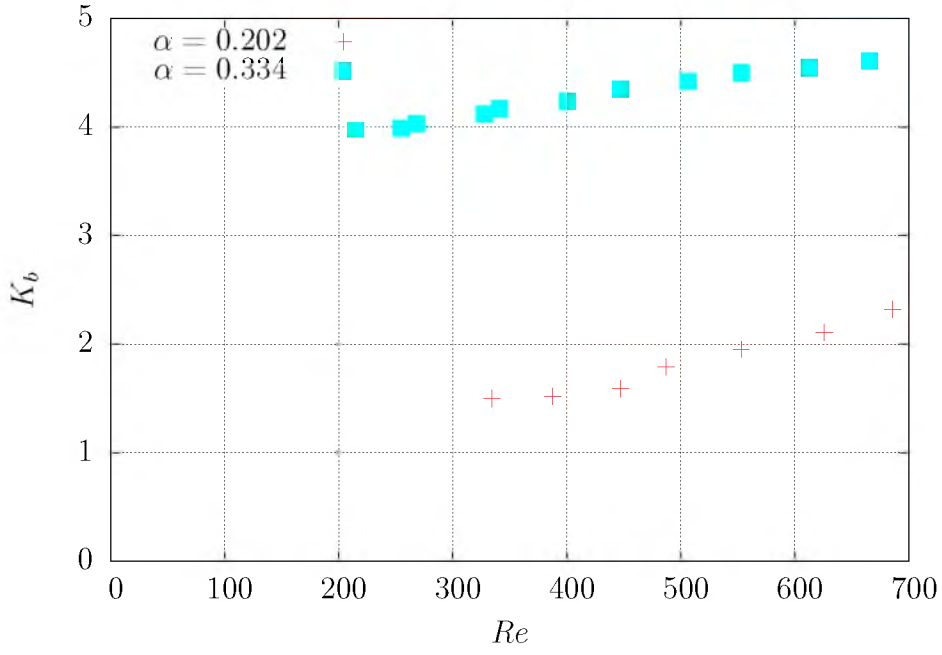

(b) K_b, **(Adopted with permission from ref. [16])**.

Figure 4.41: **Comparison of bend excess loss coefficients:** The above images show the loss coefficients for miter bend microchannels obtained from (a) simulations (b) experiments conducted by Kolekar [16].

experiments are averaged over the channel measurements at various locations, which could produce an excess loss coefficient that differs from the simulation. The loss coefficients from the simulations increase with increasing aspect ratio, which is also observed in the experimental loss coefficients for channels A, B, E ($\alpha = 0.311$), and F, as shown in Fig. (4.41b). The differences in the simulation and experimental excess loss coefficients are most likely due to the inaccuracies and defects in the xurographic channels, in addition to the measurement inaccuracies. The loss coefficients obtained from the simulations are, therefore, in good agreement with the experimental results, which also help provide some validation for the simulation procedure.

Increasing the area ratio at the miter bend, the bend excess loss coefficient, now denoted by K_{be}, decreases with increasing area ratio. Fig. (4.42) shows the variation in K_{be} with the Reynolds number and the area ratio at the miter bend. This behavior of K_{be} is also observed in the experimental excess loss coefficients in the straight rectangular microchannels with abrupt expansions (straight) reported by Torgerson [48]. The magnitude of the experimental K_e for straight channels is in the same range as the miter bend expansion channels. The rapid drop of K_{be} with Re, similar to the K_b for low Reynolds numbers, is observed. The gradual increase in K_{be} with Re, for $Re > 100$, as was observed in the miter bend microchannel with $A_r = 1.0$, decreases with increasing area ratio A_r. K_{be} values for the larger area ratios are nearly equal, and K_{be} for $A_r = 3.0$ are very close to zero. Notably, for smaller expansion area ratios, the change in K_{be} is on the order of $\approx 10\%$ for $100 \leq Re \leq 400$, and increases to a maximum of 20% at $Re = 600$. Further, the bend expansion loss coefficients K_{be} from the simulations for $A_r = 2.0$ are in the same range of $0.3 < K_e < 0.9$ as the experimental loss coefficients reported by Chalfi [47].

The bend excess loss coefficients for expansion channels from the simulations are further compared with the experimental loss coefficients reported by Nguyen [17] for similar area ratios of $A_r = \{2.0, 3.0\}$. Fig. (4.43a) and Fig. (4.43b) show K_{be} data from the simulation and experiments, respectively. The smallest expansion area ratio in these experiments is $A_r = 2.08$, while the largest is $A_r = 6.12$. The expansion area ratios of the experimental channels in ascending order are B, A, D, C, E, and F, which shows that the excess loss coefficients decrease with the increase in the area

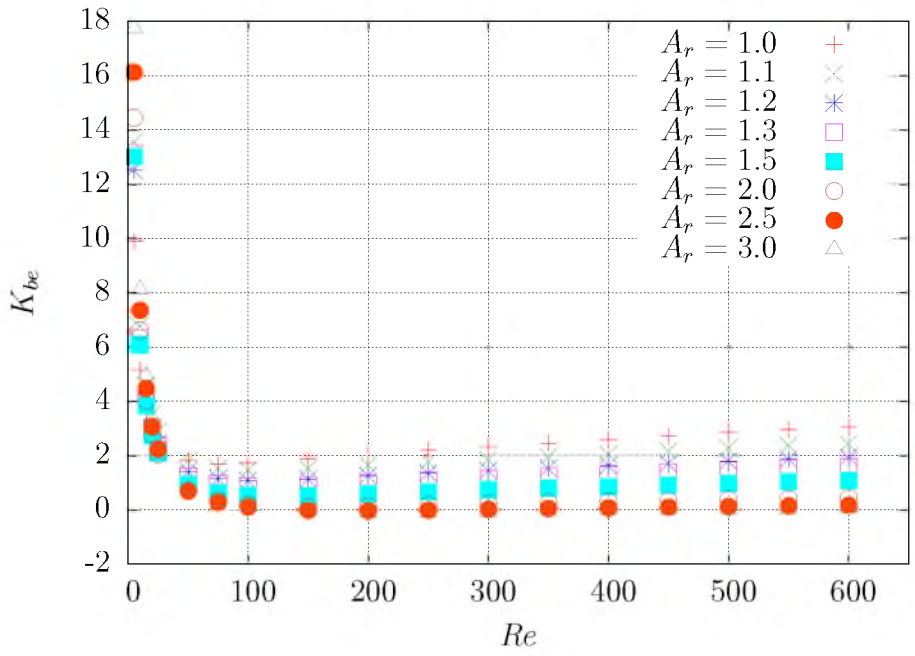

Figure 4.42: **Bend excess loss coefficients (Expansion):** The plot shows the bend excess loss coefficients for the miter bend microchannels with expansions.

ratio of the expansion channels. This trend is well predicted from the simulations, as shown in Fig. (4.43b). The loss coefficients from the experiments are much higher than the predicted K_{be} from the simulations. The larger experimental K_{be} are likely due to a number of nonidealities associated with the channels. These undesired characteristics include fabrications defects (flow tripping elements recall Fig. (1.1) and Fig. (1.2)), wall roughness, and inconsistent channel dimensions. In addition, although the friction factor f[4]is calculated from the experimental pressure drop for the inlet channel, the theoretical f was used in the outlet channel, which may introduce another source of error into the experiment.

The reduction in area ratio at the miter bend leads to an increase in the bend excess loss coefficients, here denoted by K_{bc}.[5] Fig. (4.44) shows the dependence of K_{bc} on the area ratio of contraction at the miter bend and the Reynolds number.

[4]Here, f denotes the Darcy-friction factor, not to confuse with the pressure drop f_x values for grid convergence analysis and calculating order of accuracy p from Table (3.3) and Eq. (3.10), respectively.

[5]The K_{bc} in the simulations is obtained by normalizing the bend excess head loss with the kinetic head from the inlet channel.

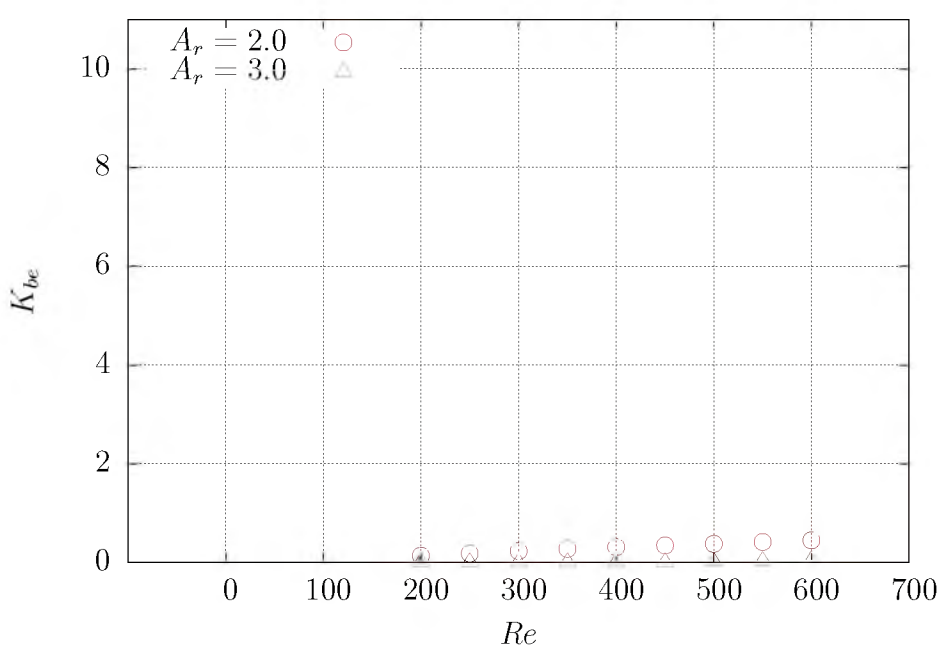

(a)

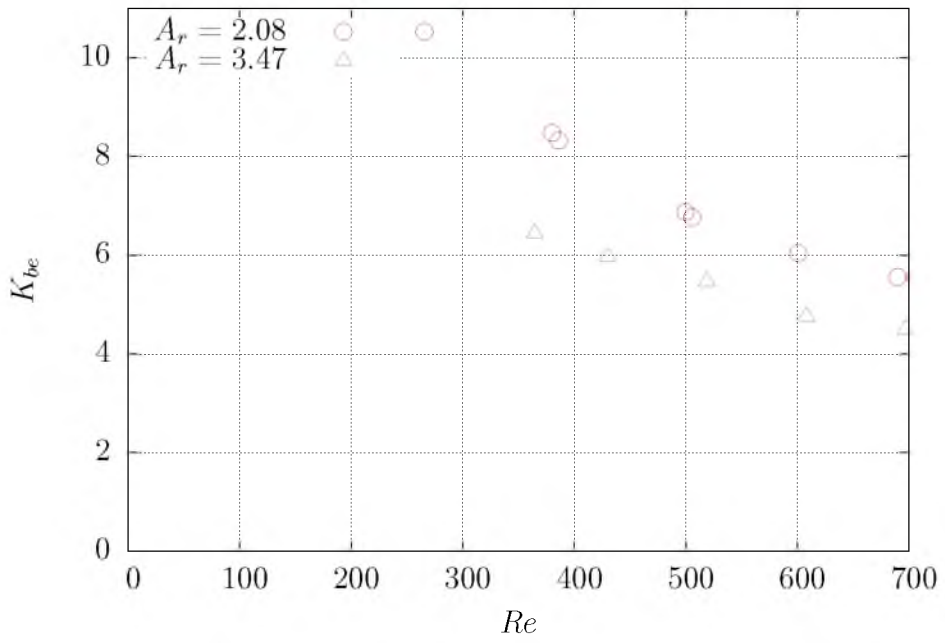

(b) **(Adopted with permission from ref. [17])**

Figure 4.43: **Comparison of bend excess loss coefficient (Expansion):** The plots shows the bend excess loss coefficients for the abrupt expansions in microchannels with $A_r = 2.0$ and $A_r = 3.0$. (a) Simulations. (b) Experiments [17]

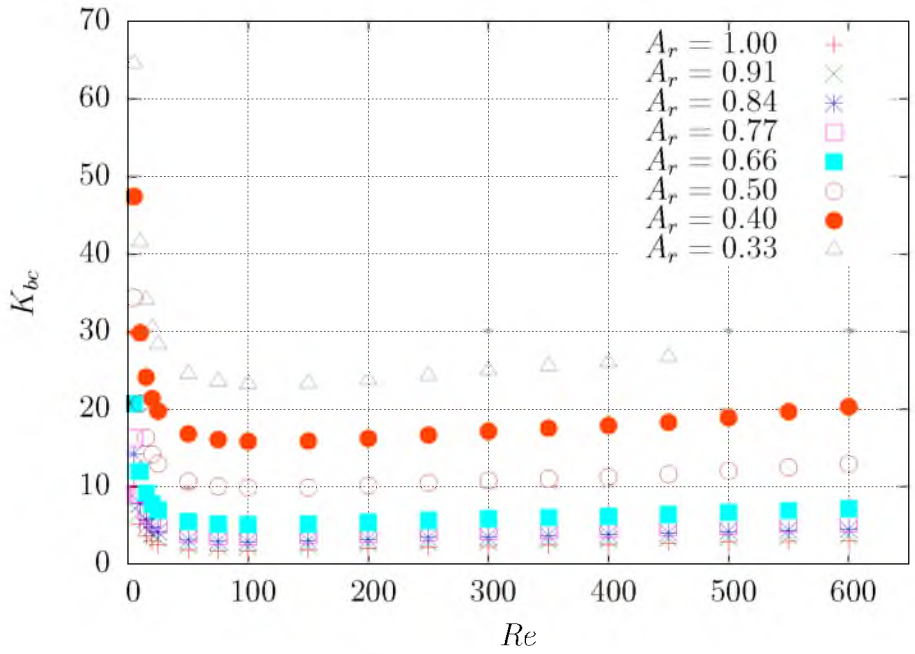

Figure 4.44: **Bend excess loss coefficients (Contraction):** The plot shows the bend excess loss coefficients for the miter bend microchannels with contractions.

Fig. (4.45) shows K_b for both minor expansion and contraction area ratios at the miter bend and Reynolds number. The percentage increase in K_{bc} with minor changes in the contraction area ratio is significantly higher when compared to the minor expansions. This behavior is the result of increased fluid shear stress at the wall due to the flow acceleration. The increase in K_{bc} with the decrease in the area ratio at the miter bend is consistent with the experimental K_c reported for straight contraction channels by Torgerson [48].

Nguyen [17] normalized the bend excess loss coefficients for the contraction channels with the kinetic head from the outlet channels, thereby reducing the order of K_c to match with K_e. The bend excess loss coefficients from his experiments are shown in Fig. (4.46b), which shows that the K_c reduces with the increase in the magnitude of contraction at the miter bend, i.e., K_c decreases with the decrease in the A_r.[6] In order to compare K_{bc} to those obtained from the experiments by Nguyen, K_{bc} for microchannels with $A_r = \{0.5, 0.33\}$ are normalized with the kinetic head from the

[6] A_r is defined as the ratio of outlet to the inlet cross-section areas

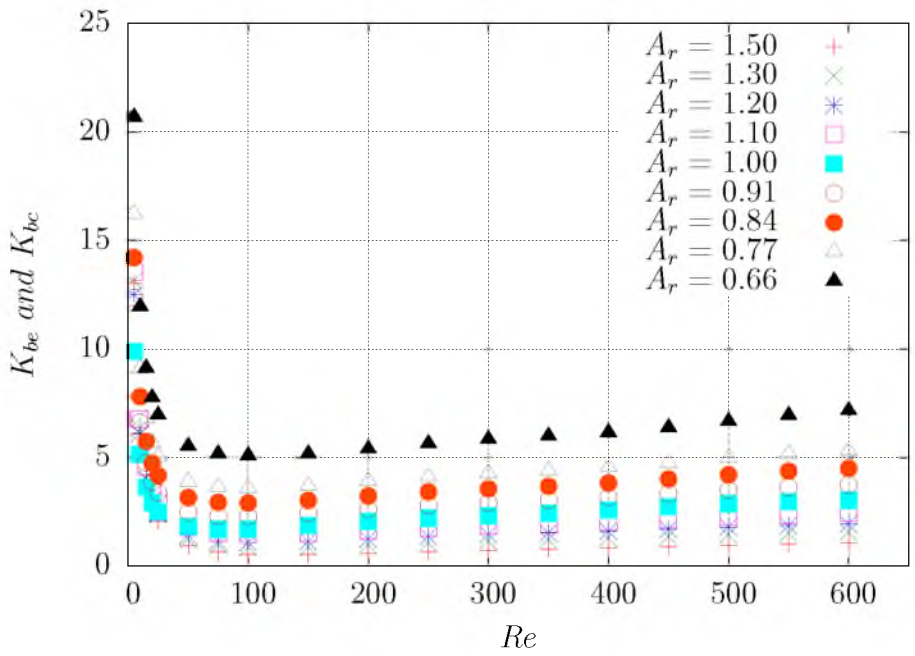

Figure 4.45: **Bend excess loss coefficients for minor aberrations:** The plot shows the bend excess loss coefficients for minor changes in the area ratio at the miter bend of the microchannel.

outlet channel and are shown in the Fig. (4.46a). Surprisingly, the adjusted K_{bc} are higher for the smaller A_r. Note that the increase in K_{bc} is very small when Re is increased or A_r is decreased, suggesting that K_{bc} could be assumed to be constant for these conditions without introducing any undesirable effects. Once again, the higher excess loss coefficients in the experiments when compared to the simulations are due to the following reasons:

- in the experiments, the friction factor f for the outlet channel is determined from the Eq. (2.3), which produces a smaller value than the actual friction factor due to the surface roughness (which is not well characterized), resulting in a smaller estimate of frictional loss in the outlet channel,

- inconsistent channel dimensions created by the razor cutting process used in xurography, and

- in the xurographic channels used for the experiments, the presence of overcuts at the bends and adhesive globules in the channel system (see Fig. (1.1) and

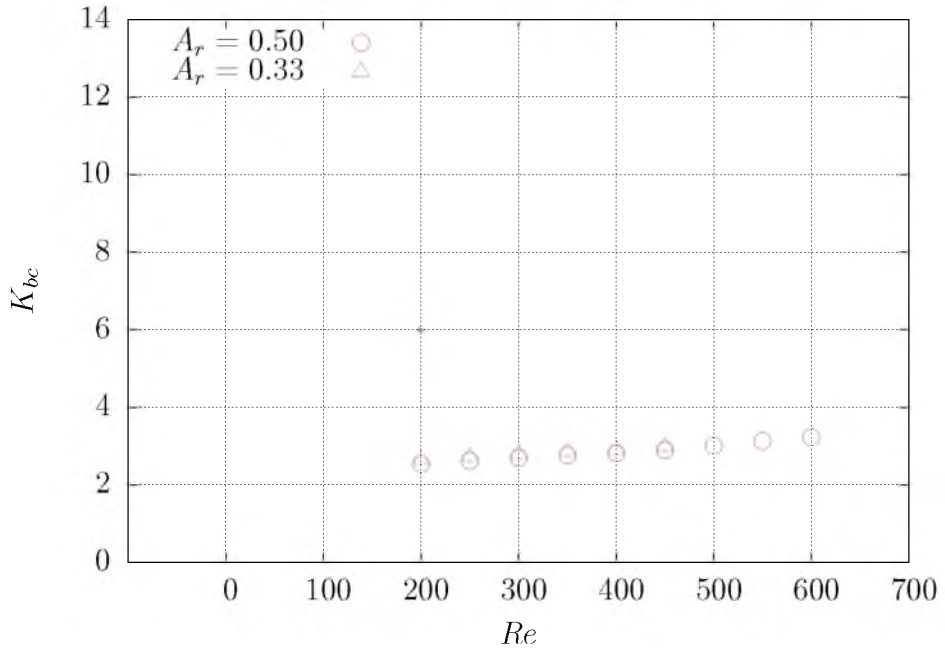

(a)

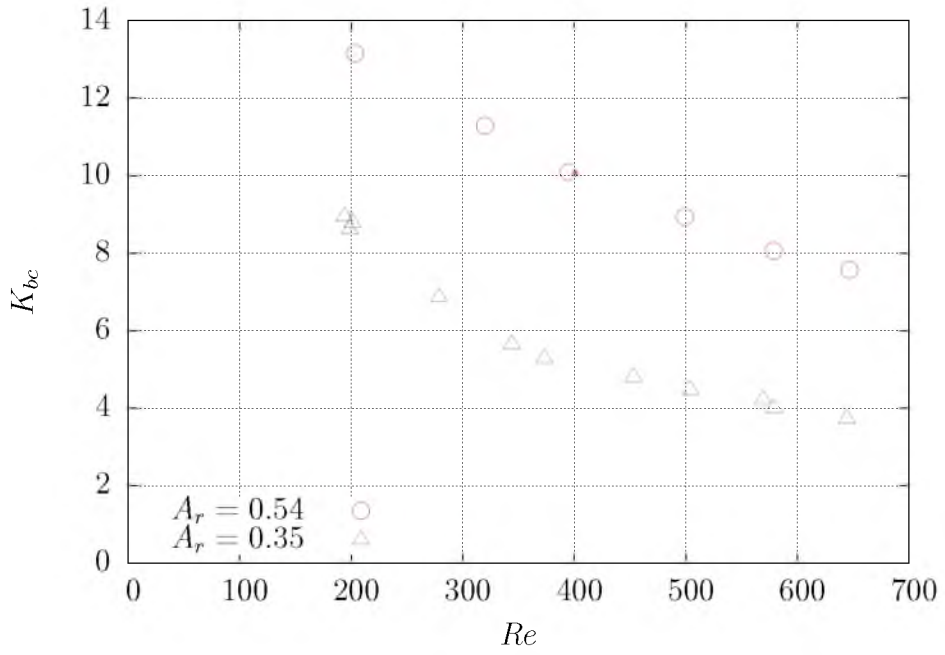

(b) **(Adopted with permission from ref. [17])**

Figure 4.46: **Comparison of bend excess loss coefficient (Contraction):**The plots show the bend excess loss coefficients for the abrupt contractions in microchannels with $A_r = 0.5$ and $A_r = 0.33$. (a) Simulations. (b) Experiments [17]

Fig. (1.2)), result in a higher pressure drop across the channel.

When a smaller frictional loss estimate from theory and a higher total pressure drop are substituted into the Eq. (2.5), it results in higher bend excess loss coefficients.

4.6 Summary

The flow simulations for steady state, isothermal, laminar water flows have been performed for Reynolds numbers between 5 and 600. The microchannels with miter bends featuring abrupt expansions and contractions were used as the flow domains in these simulations. The aspect ratios of these channels were in the range of $0.2 \leq \alpha \leq 1$ and the area ratios at the bend in the range of $0.33 \leq A_r \leq 3$.

The flow structure in the miter bend microchannels was analyzed. The flow separation downstream of the miter bend in the outlet channel began at around $Re = 50$. An axial vortex flow regime developed in the outlet channel around $Re = 300$, after which the primary recirculation zone remained constant in size. This axial flow vortex intensified with the decrease in A_r. The width of the primary recirculation zone decreased with the decreasing aspect ratio, while it increased with the increase in the magnitude of expansion and contraction at the miter bend. The secondary recirculation zone showed a significant increase in size for smaller aspect ratio with the increase in Reynolds number, after which it reduced to an asymptotic value. With the development of the axial vortex, the length of the secondary recirculation zone into the outlet decreased while it increased in depth into the inlet channel.

The flow development lengths in the outlet channels were also investigated. Due to the highly three-dimensional nature of the velocity field at the bend and the presence of the recirculation zone, the flow development lengths are much higher than predicted by the Martinelli's equation. L_{dev} predicted by the conventional equation provided a good approximation for the outlet channel development length from the simulations at lower Reynolds numbers. The nonlinear dependency of L_{dev} at the midrange Re observed in smaller aspect ratio channels is attributed to the development of the axial vortex flow in the outlet channel. As expected, L_{dev} increases with the decrease in the A_r at the miter bend, while it decreases with the increasing A_r due to flow

deceleration up to $A_r = 1.5$. An increase in A_r beyond 1.5 results in the increase in L_{dev} due to the larger flow separation distances in the outlet channel.

The bend excess loss coefficients were evaluated for all channels and are compared to the experimental excess loss coefficients available in the literature. K_b for the miter bend microchannels decreased rapidly with increasing Re for lower Reynolds numbers, after which K_b remained fairly constant. This behavior is also observed with the expansion and contraction channels. The percentage increase in K_{bc} for a minor contraction is far greater than that of K_{be} for an equivalent expansion. K_b values for the simulations were in the same range of the experimental bend excess loss coefficients available in the literature, while K_{be} and K_{bc} were substantially smaller than the experimental counterparts from similar channels. The K_{be} decrease with increasing A_r and the K_{bc} increase with decreasing A_r are trends that are consistent with the available literature. For higher A_r, K_{be} values are both very similar and nearly constant with Re, suggesting that the bend excess loss coefficient is insignificant for the higher expansion area ratios.

CHAPTER 5

CONCLUSIONS

Steady state, isothermal, and incompressible flow simulations of water in miter bend microchannels are successfully performed in this study. Commercially available CFD packages of Fluent and Gambit are used to perform these simulations in the laminar regime with the Reynolds numbers in the range of $5 \leq Re \leq 600$. Other parameters considered in this study are the aspect ratio (α) of the microchannel and area ratio (A_r) at the miter bend. The changes in the flow structure with the Reynolds number, aspect ratio, and the area ratio at the miter bend of the microchannels were studied.

5.1 Conclusions

The data for the size of the recirculation zones at the miter bend, the flow development lengths in the outlet channel, and the bend excess loss coefficients are evaluated from these simulations. The following conclusions are made from the results obtained through this study:

- The flow separation downstream of the miter bend occurs at approximately $Re = 50$ and continues to increase in size up to $Re = 300$, beyond which it remains constant in both length and width.

- For channels with high expansion area ratio ($A_r = \{2.0, 2.5, 3.0\}$), the flow separation on the inner corner of the miter bend begins at a smaller Reynolds number, $Re = 25$. The same early onset of flow separation occurs for the channel with greatest contraction ($A_r = 0.33$).

- The length as well as the width of the primary recirculation zone increases with the increase in A_r for the expansion channels. A maximum width of $0.3w_o$ is observed for the expansion channel with $A_r = 3.0$.

- In contraction channels, the length of the primary recirculation zone remains constant for higher contraction area ratios, i.e., $0.67 \leq A_r \leq 1.0$.

- For smaller area ratios of contraction, i.e., $A_r = \{0.5, 0.4, 0.33\}$, L_{rpc} increases with the decreasing area ratio. L_{rpc} attains a peak value and decreases with further increase in Re.

- An axial flow vortex develops on top of the primary recirculation zone, downstream of the miter bend, at around the same Re as above and continues to grow in magnitude with the increase in Re.

- The Re at which the axial vortex first develops increases with an increase in A_r for the expansion channels due to the magnitude of flow deceleration. In contraction channels, the acceleration of the flow as A_r decreases, increases the magnitude of the axial vortex.

- The ratio of the width of the primary recirculation zone to the width of the outlet channel increases with the increase in the α of the channel. A maximum value of 50% is observed for $\alpha = 1.0$. Further, this width ratio increases rapidly with Re for lower Reynolds numbers and tends to move towards an asymptotic value for $Re = 600$.

- A very small flow separation on the outer corner exists from as early as $Re = 5$. This separation begins to develop into a recirculation zone as Re increases. The Re at which a significant growth in the zone is observed increases with decreasing α.

- The extent of penetration of the secondary recirculation zone into the upstream and downstream flow increases with the increase in Re. After a certain Re, the length of the recirculation zone into the outlet channel decreases when the axial flow vortex begins to develop.

- The Re when L_{rso} begins to decrease, increases with increasing α.

- The flow development length L_{dev} in the outlet channel is in good agreement with the conventional estimation for $Re < 250$. For $250 \leq Re \leq 400$, L_{dev} is

nearly constant due to the formation of an axial vortex in the outlet channel. This deviation occurs at larger Re as the aspect ratio of the microchannel decreases.

- For higher aspect ratios ($\alpha \geq 0.5$), L_{dev} increases linearly with Re and is in good agreement with the conventional model [37] as well as the relation reported by Ahmad and Hassan [49].

- The development length in the outlet channel is better predicted by the conventional model [37] given by Eq. (2.12) than the Martinelli and Viktorov's [50] correlation based on α.

- The flow development lengths decrease with increasing A_r at the miter bend up to $A_r = 1.5$ due to flow deceleration. The Re at which the axial flow vortex begins to develop increases with increasing A_r. At higher area ratios, L_{dev} increases with increasing A_r as the primary recirculation zone increases in size.

- In contraction channels, L_{dev} increases significantly even for the minor area contractions, i.e., $A_r = \{0.91, 0.87, 0.77, 0.67\}$. The linear increase in L_{dev} with Re for small A_r indicates that the axial vortex in the outlet is of near constant magnitude for these channels.

- The bend excess loss coefficient K_b decreases rapidly with increasing Re for lower Reynolds number, after which K_b remains fairly constant with the increase in Re.

- The K_b decreases with the increase in α. K_b for microchannels with $\alpha = \{0.2, 0.33\}$ are in good agreement with the experimental excess loss coefficient reported by Kolekar [16].

- The experimental K_b are higher in magnitude when compared with the simulations as the experimental results include the losses due to surface roughness, inconsistent channel dimensions, and fabrication defects into the bend loss.

- K_{be} decreases with an increase in A_r due to flow deceleration. For higher A_r, K_{be} is very small, on the order of ≈ 0.05 for a microchannel with $A_r = 3.0$

for $Re = 600$. This trend is in agreement with the experimental excess loss coefficients reported by Nguyen [17], although the magnitudes of K_{be} are far less than the experimental K_e.

- K_{bc} increases significantly even for a small change in the contraction area at the miter bend, when normalized by the kinetic head at the inlet. Notably, when normalized by using the kinetic head of the outlet, the K_{bc} for the smaller area ratios, i.e., $A_r = \{0.40, 0.33\}$, are of the same order in contrast to the deceasing trend reported by Nguyen [17].

- The large difference in the excess loss coefficients from the simulations and the experiments is due to the larger pressure drops across the experimental channels due to surface roughness, inconsistent channel dimensions, and the damage to the channel walls resulting from the cutting process.

- Interestingly, the bend excess loss coefficients due to abrupt expansions and contractions fall in the same range as the experimental loss coefficients reported in the literature for straight channel expansions and contractions.

Upon close analysis of the effects of expansions and contractions on the bend excess loss coefficients, it can be concluded that an abrupt expansion at the 90° miter bend is conducive in keeping excess loss coefficients in microfluidic devices to a minimum. It is suggested that the design of the channel width downstream of a 90° miter bend be oversized to offset the imprecision of the cutting plotter and to ensure that $A_r \geq 1$.

From this study, it is evident that FLUENT offers an excellent choice for the simulations of microchannel flows using the FVM approach to solve the Navier-Stokes equations. The choice of the third-order MUSCL scheme for momentum and the PRESTO scheme for pressure discretization results in an overall solution scheme with an order of convergence of 1.85, which is far better than the procedures used by Dreher et al. [52]. In addition to better order of convergence, the present study uses a larger cell size of 5 µm, which is more than twice the cell size used in [52]. Using a higher order discretization scheme allows simulation of higher Reynolds number ($Re = 550$ for $\alpha = 1.0$ and $D_h = 100\,\mu m$) flows as compared with the literature,

where water flows have been simulated only up to $Re = 500$ by using a nominal second-order scheme in a miter bend channel with $\alpha = 1.0$ and $D_h = 200\,\mu m$ [52].

5.2 Recommendations

The effect of the lack of a flux-limiting function in the FLUENT's version of the third-order MUSCL scheme needs to be investigated. As demonstrated by Kurganov [60], the flux-limiting function reduces numerical diffusion, which results when the flow direction is not aligned with the mesh. This enhancement would provide a better estimate of the Re_{cr} for flows in the miter bend microchannels. Further, the following are some of the additional aspects of the microchannel flows that need to be explored as part of future research:

- A correlation for the flow development length in the outlet channel and the bend excess loss coefficients needs to be developed as a function of the Re, α, and A_r.
- The existence of the axial flow vortex in the outlet channel for the midrange Reynolds number needs to be verified experimentally.
- The effect of the vortices on the mixing characteristics of the 90° miter bend channels should be explored.
- The present work needs to be extended to the turbulent flow regime to study the behavior of bend excess loss coefficients at higher Reynolds number.
- The effect of the abrupt expansions or contractions at the miter bend on the heat transfer characteristics of the microchannels needs to be investigated.
- The effects of multiple bends with expansions and contractions as well as the effect of a varying configuration of such bends on the microchannels flows as seen in the serpentine microchannels should be explored.
- The effect of separation distance between successive 90° miter bends should be explored. It is expected that when the separation distance is shorter than the flow development length investigated herein, the downstream bend excess loss coefficient will be affected.

REFERENCES

[1] P. Gravesen, J. Branebjerg, and O. S. Jensen, "Microfluidics - A review," *Journal of Micromechanics and Microengineering*, vol. 3, p. 168, December 1993.

[2] D. Tuckerman and R. Pease, "High-performance heat sinking for VLSI," *Electron Device Letters, IEEE*, vol. 2, no. 5, pp. 126–129, 1981.

[3] G. M. Whitesides, "The origins and the future of microfluidics," *Nature*, vol. 442, pp. 368–373, July 2006.

[4] B. Ziaie, A. Baldi, M. Lei, Y. Gu, and R. A. Siegel, "Hard and soft micromachining for biomems: Review of techniques and examples of applications in microfluidics and drug delivery," *Advanced Drug Delivery Reviews*, vol. 56, pp. 145 – 172, 2004.

[5] B. K. Gale, M. A. Eddings, S. O. Sundberg, A. Hatch, J. Kim, and T. Ho, "Low-cost MEMS technologies," in *Comprehensive Microsystems* (Y. Gianchandani, O. Tabata, , and H. Zappe, eds.), Elsevier, 2008.

[6] B. H. Weigl, R. L. Bardell, and C. R. Cabrera, "Lab-on-a-chip for drug development," *Advanced Drug Delivery Reviews*, vol. 55, no. 3, pp. 349–377, 2003.

[7] S. Haebrele and R. Zengerle, "Microfluidic platforms for lab-on-a-chip applications," *Lab chip*, vol. 7, no. 9, pp. 1094–1110, 2007.

[8] L. A. Legendre, C. J. Morris, J. M. Bienvenue, A. Barron, R. McClure, and J. P. Landers, "Toward a simplified microfluidic device for ultra-fast genetic analysis with sample-in/answer-out capability: Application to T-cell lymphoma diagnosis," *Journal of Laboratory Automation*, vol. 13, pp. 351–360, December 2008.

[9] I. Hassan, "Thermal-fluid MEMS devices: A decade of progress and challenges ahead," *Journal of Heat Transfer*, vol. 128, pp. 1221–1233, November 2006.

[10] K. W. Oh and C. H. Ahn, "A review of microvalves," *Journal of Micromechanics and Microengineering*, vol. 16, pp. 13–39, 2006.

[11] D. J. Laser and J. G. Santiago, "A review of micropumps," *Journal of Micromechanics and Microengineering*, vol. 14, no. 6, pp. 35–64, 2004.

[12] V. Hessel, H. Löwe, and F. Schönfeld, "Micromixers — a review on passive and active mixing principles," *Chemical Engineering Science*, vol. 60, no. 8-9, pp. 2479 – 2501, 2005.

[13] D. Bartholomeusz, R. Boutte, and J. Andrade, "Xurography: rapid prototyping of microstructures using a cutting plotter," *Journal of Microelectromechanical Systems*, vol. 14, pp. 1364 – 74, 12 2005.

[14] K. E. Herold and A. Rasooly, eds., *Lab on Chip Technology (Vol. 1): Fabrication and Microfluidics.* Caister Academic Press, 2009.

[15] J. Greer, S. O. Sundberg, C. T. Wittwer, and B. K. Gale, "Comparison of glass etching to xurography prototyping of microfluidic channels for DNA melting analysis," *Journal of Micromechanics and Microengineering*, vol. 17, no. 12, pp. 2407–2413, 2007.

[16] R. Kolekar, "Fluid flow characteristics in xurographic microchannels," Master's thesis, Department of Mechanical Engineering, University of Utah, December 2009.

[17] L. T. Nguyen, "Contraction/expansion effects in 90° miter bends in rectangular xurographic microchannels," Master's thesis, Department of Mechanical Engineering, University of Utah, 2011.

[18] S. Alshareef, "Experimental study of xurographic microchannel single-pass single-phase counterflow heat exchanger," Master's thesis, Department of Mechanical Engineering, University of Utah, 2012.

[19] J. C. Adams and T. H. Brom, "Microwulf: a beowulf cluster for every desk," *SIGCSE Bull.*, vol. 40, pp. 121 –125, March 2008.

[20] S. G. Kandlikar, S. Garimella, D. Li, S. Colin, and M. R. King, *Heat transfer and fluid flow in minichannels and microchannels.* Elsevier, 2006.

[21] M. Gad-el-Hak, "The fluid mechanics of microdevices—the freeman scholar lecture," *Journal of Fluids Engineering*, vol. 121, pp. 5–33, march 1999.

[22] J. van Rij, T. Harman, and T. Ameel, "The effect of creep flow on two-dimensional isoflux microchannels," *International Journal of Thermal Sciences*, vol. 46, no. 11, pp. 1095–1103, 2007.

[23] N. Xiao, J. Elsnab, and T. Ameel, "Microtube gas flows with second-order slip flow and temperature jump boundary conditions," *International Journal of Thermal Sciences*, vol. 48, no. 2, pp. 243–251, 2009.

[24] M. Gad-el-Hak, ed., *The MEMS handbook: Introduction and fundamentals.* CRC/ Taylor & Francis, 2006.

[25] I. Papautsky, B. K. Gale, S. K. Mohanty, T. A. Ameel, and A. B. Frazier, "Effects of rectangular microchannel aspect ratio on laminar friction constant," in *SPIE Micro Fluidic Devices and Systems Conference*, pp. 147–159, 1999.

[26] I. Papautsky, J. Brazzle, T. Ameel, and A. Frazier, "Laminar fluid behavior in microchannels using micropolar fluid theory," *Sensors and Actuators A: Physical*, vol. 1-2, pp. 101–108, 1999.

[27] I. Papautsky, T. Ameel, and A. B. Frazier, "A review of laminar single-phase flow in microchannels," in *ASME Int. Mechanical Engineering Congress and Exposition*, 2001.

[28] G. L. Morini, "Single-phase convective heat transfer in microchannels: a review of experimental results," *International Journal of Thermal Sciences*, vol. 43, pp. 631–651, 2004.

[29] J. Koo and C. Kleinstreuer, "Liquid flow in microchannels: experimental observations and computational analyses of microfluidics effects," *Journal of Micromechanics and Microengineering*, vol. 13, no. 5, pp. 568–579, 2003.

[30] G. Hetsroni, A. Mosyak, E. Pogrebnyak, and L. Yarin, "Fluid flow in microchannels," *International Journal of Heat and Mass Transfer*, vol. 48, no. 10, pp. 1982–1998, 2005.

[31] Q. Weilin, G. M. Mala, and L. Dongqing, "Pressure-driven water flows in trapezoidal silicon microchannels," *International Journal of Heat and Mass Transfer*, vol. 43, no. 3, pp. 353–364, 2000.

[32] W. Qu and I. Mudawar, "Experimental and numerical study of pressure drop and heat transfer in a single-phase micro-channel heat sink," *International Journal of Heat and Mass Transfer*, vol. 45, no. 12, pp. 2549–2565, 2002.

[33] J. Judy, D. Maynes, and B. Webb, "Characterization of frictional pressure drop for liquid flows through microchannels," *International Journal of Heat and Mass Transfer*, vol. 45, no. 17, pp. 3477–3489, 2002.

[34] M. Kohl, S. Abdel-Khalik, S. Jeter, and D. Sadowski, "An experimental investigation of microchannel flow with internal pressure measurements," *International Journal of Heat and Mass Transfer*, vol. 48, no. 8, pp. 1518–1533, 2005.

[35] D. Costaschuk, J. Elsnab, S. Petersen, J. Klewicki, and T. Ameel, "Axial static pressure measurements of water flow in a rectangular microchannel," *Experiments in Fluids*, vol. 43, no. 6, pp. 907–916, 2007.

[36] A. J. Ward-Smith, *Internal fluid flow: The fluid dynamics of flow pipes and ducts.* Oxford: Clarendon Press, 1980.

[37] R. K. Shah and A. L. London, *Laminar flow forced convection in ducts: A source book for compact heat exchanger analytical data.* Advances in heat transfer, Supplement 1, Academic press, 1978.

[38] S. Yuk Kwan Lee, M. Wong, and Y. Zohar, "Pressure losses in microchannels with bends," in *Micro Electro Mechanical Systems, 2001. MEMS 2001. The 14th IEEE International Conference on*, pp. 491–494, 2001.

[39] S. Maharudrayya, S. Jayanti, and A. Deshpande, "Pressure losses in laminar flow through serpentine channels in fuel cell stacks," *Journal of Power Sources*, vol. 138, pp. 1–13, 2004.

[40] N. Kockmann, M. Engler, D. Haller, and P. Woias, "Fluid dynamics and transfer processes in bended micro channels," *ASME Conference Proceedings*, vol. 2004, no. 41642, pp. 165–171, 2004.

[41] D. Haller, P. Woias, and N. Kockmann, "Simulation and experimental investigation of pressure loss and heat transfer in microchannel networks containing bends and t-junctions," *International Journal of Heat and Mass Transfer*, vol. 52, no. 11-12, pp. 2678–2689, 2009.

[42] R. Xiong and J. N. Chung, "Flow characteristics of water in straight and serpentine micro-channels with miter bends," *Experimental Thermal and Fluid Science*, vol. 31, pp. 805–812, 2007.

[43] R. Xiong and J. N. Chung, "Effects of miter bend on pressure drop and flow structure in micro-fluidic channels," *International Journal of heat and Mass Transfer*, vol. 51, pp. 2914–2924, 2008.

[44] H. Herwig, B. Schmandt, and M.-F. Uth, "Loss coefficients in laminar flows: Indispensable for the design of micro flow systems," *ASME Conference Proceedings*, vol. 2010, no. 54501, pp. 1517–1528, 2010.

[45] R. W. Fox, A. T. McDonald, and P. J. Pritchard, *Introduction to Fluid Mechanics*. Hoboken, NJ: John Wiley & Sons, Inc, 6 ed., 2004.

[46] F. Abdelall, G. Hahn, S. Ghiaasiaan, S. Abdel-Khalik, S. Jeter, M. Yoda, and D. Sadowski, "Pressure drop caused by abrupt flow area changes in small channels," *Experimental Thermal and Fluid Science*, vol. 29, no. 4, p. 4, 2005.

[47] T. Y. Chalfi, "Pressure loss associated with flow area change in micro-channels," Master's thesis, School of Mechanical Engineering, Georgia Institute of Technology, 2007.

[48] D. E. Torgerson, "Microscale loss coefficients through expansion and contraction xurographic microchannels," Master's thesis, Department of Mechanical Engineering, University of Utah, 2010.

[49] T. Ahmad and I. Hassan, "Experimental analysis of microchannel entrance length characteristics using microparticle image velocimetry," *Journal of Fluids Engineering*, vol. 4, pp. 041102(1–13), 2010.

[50] M. Martinelli and V. Viktorov, "Modelling of laminar flow in a inlet section of rectangular microchannel," *Journal of Micromechanics and Microengineering*, vol. 19, no. 2, p. 025013 (9 pp.), 2009.

[51] N. Kockmann, C. Holvey, and D. M. Roberge, "Transitional flow and related transport phenomena in complex microchannels," *ASME Conference Proceedings*, vol. 2009, no. 43499, pp. 1301–1312, 2009.

[52] S. Dreher, N. Kockmann, and P. Woias, "Characterization of laminar transient flow regimes and mixing in t-shaped micromixers," *Heat Transfer Engineering*, vol. 30, no. 1-2, pp. 91–100, 2009.

[53] S. H. Wong, P. Bryant, M. Ward, and C. Wharton, "Investigation of mixing in a cross-shaped micromixer with static mixing elements for reaction kinetics studies," *Sensors and Actuators B: Chemical*, vol. 95, pp. 414–424, 2003.

[54] C. Galletti, M. Roudgar, E. Brunazzi, and R. Mauri, "Effect of inlet conditions on the engulfment pattern in a t-shaped micro-mixer," *Chemical Engineering Journal*, vol. 185-186, pp. 300–313, 2012.

[55] S. V. Patankar, *Numerical Heat Transfer and Fluid Flow.* Series in computational methods in mechanics and thermal sciences, Washington : Hemisphere Pub. Corp. ; New York : McGraw-Hill, c1980., 1980.

[56] Ansys, Inc., *Fluent 6.3 User's Guide*, 2006.

[57] B. P. Leonard, "A stable and accurate convective modelling procedure based on quadratic upstream interpolation," *Computer methods in applied mechanics and Engineering*, vol. 19, pp. 59–98, 1979.

[58] B. P. Leonard and S. Mokhtari, "Ultra-sharp nonoscillatory convection schemes for high speed steady multidimensional flow," tech. rep., Institution for Computational Mechanics in Propulsion, Cleveland, Ohio., 1990.

[59] B. van Leer, "Towards the ultimate conservative difference scheme. v. a second-order sequel to godunov's method," *Journal of Computational Physics*, vol. 32, no. 1, pp. 101–136, 1979.

[60] A. Kurganov and D. Levy, "A third-order semidiscrete central scheme for conservation laws and convection-diffusion equations," *SIAM Journal on Scientific Computing*, vol. 22, pp. 1461–1488, 2000.

[61] S. Acharya, B. R. Baliga, K. Karki, J. Y. Murthy, C. Prakash, and S. P. Vanka, "Pressure-based finite-volume methods in computational fluid dynamics," *Journal of Heat Transfer*, vol. 129, no. 4, pp. 407–424, 2007.

[62] S. P. Vanka and G. K. Leaf, "Fully-coupled solution of pressure-linked fluid flow equations," Tech. Rep. ANL-83-73, Argonne National Lab., IL (USA), August 1983.

[63] M. J. Raw, "A coupled algebraic multigrid method for the 3D navier-stokes equations," *Notes on Numerical Fluid Mechanics*, vol. 49(1), pp. 204–215, 1995.

[64] Ansys, Inc., *Gambit 2.4 User's Guide*, 2007.

[65] M. Spiga and G. L. Morini, "A symmetric solution for velocity profile in laminar flow through rectangular ducts.," *International Communications in Heat and MassTransfer*, vol. 21, pp. 469–475, 1994.

[66] R. C. Weast, ed., *CRC handbook of chemistry and physics: 1st student.* Boca Raton: CRC Press, 1988.

[67] P. J. Roache, *Verification and validation in computational science and engineering.* Hermosa publishers, 1998.